Smart control of light in Edge-Emmiting Lasers

PhD Thesis by:
Judith Medina Pardell

Supervisors:
Muriel Botey
Ramon Herrero

Tutor:
Kestutis Staliunas

Universitat Politècnica de Catalunya,
Physics department

Contents

Acknowledgments

During these years, many people have participated in one way or another in my life, either in a scientific and in a personal perspective. I want to thank them all for the time shared and help provided.

I would like to thank my advisors Prof. Muriel Botey and Prof. Ramon Herrero, for bringing me the opportunity to complete my PhD thesis at Universitat Politècnica de Catalunya. I would like to thank them for the patience, guidance, and support they gave during entirely stay in Terrassa.

I am also grateful to Prof. Kestutis Staliunas and Prof. Josep Trull for their valuable ideas and suggestions to successfully complete this thesis. I would also like to thank Prof. Crina Cojocaru, Prof. Cristina Masoller, Prof. Antonio Pons, Prof. Jordi Tiana, and Prof. Ramon Vilaseca from the DONLL group for their valuable suggestions, questions, and support during the various group's meetings.

I would like to thank Dr. Shubam Kumar, Dr. Waqas Waseem, Dr. Carlos Quintero-Quiroz, Dr. Dario Zappala**,** Dr. Sandeep Gawali, Dr. Maria Masoliver**,** Dr. Pablo Amil, Dr. Hossam Selim, Dr. Donatus Halpaap, Ricardo Silini, Laura Rodríguez**,** Salim Benadouda, and Tetsu Magariyachi for their help and support as colleagues and as friends and for all the good moments during lunchtimes and breaks hours.

M'agradaria mencionar també a totes les persones que han format part d'aquest camí d'una forma més personal i que sense ells no hauria estat el mateix. Als companys d'Enginyeria Física i del Màster de Fotònica per les dures hores a la biblioteca i els sopars i festes post-estudi. Als amics i amigues del Penyafort per fer-me sentir com a casa i ser la meva família. A tots els amics de Barcelona, per compartir i fer-me estimar aquesta ciutat que m'ha donat els millors dels records i a les amigues de Lleida per ser el lloc on poder tornar sempre.

Finalment, a la meva parella, el Raül per aparèixer a la meva vida quan menys ho esperava i donar-me el suport, la calma i l'amor que necessitava. Gràcies per treure'm sempre un somriure en els pitjors moments i convertir-te en la meva roca. Tampoc vull deixar-me la meva família i agrair-los estar sempre al meu costat, cuidar-me i estimar-me i en especial a la meva mare per mai deixar de creure en mi i sacrificar tot el que fes falta.

List of publications

I S. Gawali, J. Medina, D. Gailevičius, V. Purlys, G. Garre-Werner, C. Cojocaru, J. Trull, M. Botey, R. Herrero, J. Montiel-Ponsoda, and K. Staliunas, "*Spatial filtering in edge-emitting lasers by intracavity chirped photonic crystals,*" Journal of the Optical Society of America B **37**(10), 2856-2864 (2020).

II W. W. Ahmed, S. Kumar, J. Medina, M. Botey, R. Herrero, and K. Staliunas, "*Stabilization of broad-area semiconductor laser sources by simultaneous index and pump modulations,*" Optics Letters **43**(11), 2511-2514 (2018).

III W. W. Ahmed, S. Kumar, J. Medina, M. Botey, R. Herrero, and K. Staliunas, *"Stabilization of Broad Area Semiconductor Amplifiers and Lasers by Double Modulation of Pump and Refractive Index,"* 2018 20th International Conference on Transparent Optical Networks (ICTON), IEEE, 2018.

IV J. Medina, W. W. Ahmed, S. Kumar, M. Botey, R. Herrero, and K. Staliunas, *"Stabilization of Broad Area Semiconductor Laser Sources,"* 2018 20th International Conference on Transparent Optical Networks (ICTON), IEEE, 2018.

V J. Medina, M. Botey, R. Herrero, and K. Staliunas, *"Stabilized narrow-beam emission from broad-area semiconductor lasers,"* Physical Review A **101**(3), 033833 (2020).

VI J. Medina, M. Botey, R. Herrero, and K. Staliunas, *"Spatiotemporal stabilization of PT-symmetric BAS lasers,"* SPIE Photonics Europe, Society of Photo-Optical Instrumentation Engineers (SPIE), 2020.

VII J. Medina, M. Botey, R. Herrero, and K. Staliunas, *"Spatiotemporal stabilization of PT-symmetric BAS lasers,"* European Conference on Lasers and Electro-Optics (CLEO Europe), OSA, 2019.

VIII M. Botey, W. W. Ahmed, J. Medina, R. Herrero, and K. Staliunas, *"Non-Hermitian Broad Aperture Semiconductor Lasers Based on PT-Symmetry,"* 2019 21st International Conference on Transparent Optical Networks (ICTON), IEEE, 2019.

IX M. Botey, W. W. Ahmed, J. Medina, R. Herrero, Y. Wu, Y., and K. Staliunas, *"Regularization of broad-area lasers by non-Hermitian potentials,"*Proceedings of The 10th International Conference on Metamaterials, Photonic Crystals and Plasmonics (META), 2019.

X J. Medina, R. Herrero, M. Botey, and K. Staliunas, *"Stabilized Bright Narrow Beams from Edge-Emitting Lasers*," 2020 22nd International Conference on Transparent Optical Networks (ICTON), IEEE, 2020.

XI J. M. Pardell, R.Herrero, M. Botey, and K. Staliunas, *"Non-Hermitian arrangement for stable semiconductor laser,"* Optics Express **29**(15), 23997-24009 (2021).

Preface

The invention of the laser triggered the study of light-matter interactions. In turn, the advent of artificial structured materials on micro- and nanometer scales has become a fruitful playground to tailor the propagation and generation of light, even in exotic or counterintuitive ways, uncovering novel physical phenomena. In this thesis, we propose using artificial photonic materials and new schemes to control the spatiotemporal dynamics of broad area edge-emitting semiconductor lasers (EELs), as well as contributing to the control of the field dynamics by non-Hermitian Photonics.

Indeed, the new physics based on open-dissipative non-Hermitian systems is beyond the recent focus on optical systems holding modulations of the complex permittivity, field referred as non-Hermitian Photonics [El-G18]. As initially demonstrated in Quantum Mechanics, systems described by non-Hermitian Hamiltonians may still present real eigenvalues (energy) as conservative Hermitian systems. Moreover, they hold other unexpected physical behaviors derived from the asymmetric coupling between modes. In particular, this was first observed in systems invariant under Parity (P-) and Time (T-) symmetry — referred to as PT-symmetric — [Ben98]. Photonic Crystals (PhC) were the first pioneering artificial photonic materials. The periodic modulations of the index of refraction on the order of wavelength, tailor the temporal and spatial dispersion properties, therefore offering the ability to filter, localize and shape light [Yab87, Joh87]. It is interesting to note that while dissipation is an inherent property of all forms of matter, most of it was completely disregarded in all the initial works on periodic artificial media [Jao11]. However, soon attention was also paid to analogous, equally accessible artificial nanophotonic structures, where gain and losses are modulated on the wavelength scale [Sta09, Bot10].

Finally, the interplay between real and imaginary components of permittivity came into play as optical systems with complex permittivity became flexible and

achievable classical analogs of such quantum systems to realize and explore the predicted novel effects.

Therefore, the new platform of non-Hermitian Photonics, including the pioneering PhCs, has paved the way to experiment with fundamental concepts in physics which are easier to realize in optics; and to uncover effects in photonics that are universal of other kinds of waves beyond the domain of electromagnetic waves. Non-Hermitian Photonics presents a large variety of direct applications and is at the basis of emerging fields, summarized in Figure 1.

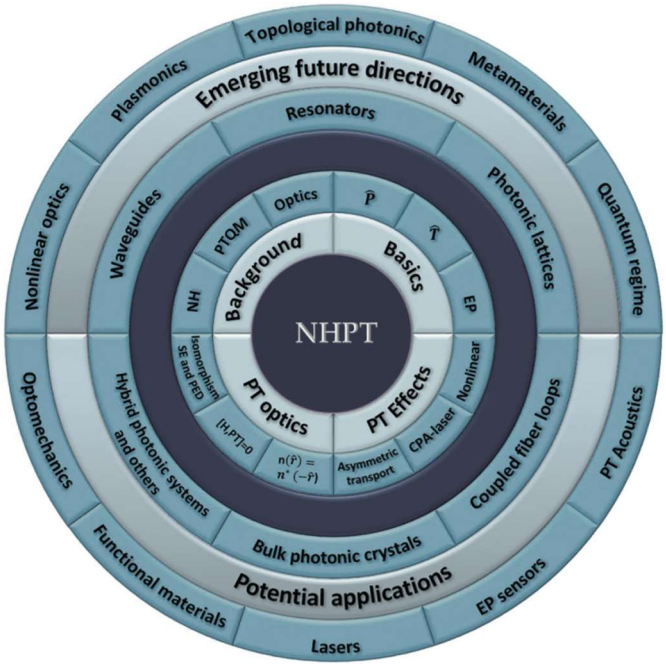

Figure 1. An overview of the review based on non-Hermitian physics and PT symmetry (NHPT), graphic from [Gup20].

Besides, semiconductor lasers and in particular EELs, are replacing other laser sources due to their compactness, efficiency, affordable prices and performance, however, they suffer from a major drawback when the aperture of the laser is very broad as compared to the wavelength. In addition, as power increases, the quality of the emitted beam intrinsically deteriorates. Under these conditions, emission becomes highly multimode and unstable, limiting possible applications. Although different mechanisms have been proposed, obtaining a stable and bright emission without compromising their compact design remains a longstanding open question. This thesis aims at contributing to this goal and to

the field of non-Hermitian Photonics by proposing four compact schemes to improve the beam quality and stabilize the emission from EELs.

The original work performed during my PhD along four years resulted in four published papers [Ahm18, Gaw20, Med20, Med21], the first one which I coauthor as a collaborator, and other three where I am the first author, and seven conference papers [Ahm18-2, Bot19, Bot19-2, Bot20, Med18, Med19, Med20-2]. Therefore, this PhD presents the results published on the four papers and seven conference proceedings, and it is organized as follows:

Chapter 1 provides an overview of the general properties of edge-emitting (EE) light sources, considering amplifiers, lasers, and laser bars, which are studied and modeled throughout the thesis. We include the description of the main beam quality parameters and the state of the art of different physical models, divided into mean-field models and adiabatic models, depending on their main approximations. Moreover, we briefly summarize various existing proposals to improve the beam quality of EEL and EEL bars. Finally, we introduce the periodical modulations systems that can be used to filter and control light. Specifically, we present non-Hermitian PT-symmetric systems and their applications.

In Chapter 2, and as a first step, we propose to use chirped PhCs for intracavity filtering the multimode emission of EELs. To numerically assess the filtering performance, we developed a full (2+1)-dimensional spatio-temporal model, including transverse and longitudinal dimensions plus time, to evolve the electric field and carriers. The effect is demonstrated numerically as well as experimentally. The good agreement of the predictions with actual experimental results demonstrates the proposal and validates the model used throughout the thesis, with corresponding modifications.

In Chapter 3, we propose to impose intrinsic complex, refractive index and gain modulations within EELs and use the non-Hermitic potential to achieve spatial and temporal stabilization. The effect is demonstrated by the stability analysis on a simplified model and numerical simulations.

Going one step further, in Chapter 4, we propose to divide the EEL cavity into two mirror-symmetric half-spaces holding PT-symmetry with opposite mode coupling directed toward the symmetry axis. With this geometry, we expect to obtain a two-fold benefit: on one hand, achieving a spatio-temporal stabilization

of the laser, and on the other, localizing the field generated all over the laser along the symmetry axis. We numerically demonstrate regimes of simultaneous localization and stabilization leading to an enhanced output and improved beam quality.

Next, in Chapter 5, we extend the mirror-symmetric non-Hermitian coupling to an array of thin EELs (diode bar). While thinner lasers show a more stable emission, this is not a solution for EEL bars since new temporal and synchronization instabilities arise from the coupling between neighboring lasers, leading again to irregular spatiotemporal behaviors. Therefore, we extend the proposed mirror symmetric non-Hermitian configuration to couple individual EELs in the array by a lateral shift between the pump and index profiles. The localized and stable output beam may facilitate a direct coupling of these semiconductor lasers arrays to an optical fiber.

Finally, Chapter 6 summarizes the results and presents the conclusions of the thesis and a discussion on future perspectives.

Chapter 1
Introduction

1.1 Characteristics of edge-emitting light sources

Semiconductor optical devices, particularly amplifiers and lasers, are promising and reliable solid-state light sources due to their robustness, compactness, and high efficiency with various fields: photonics, engineering, biology, chemistry, and medicine. Applications range from pumping other solid-state lasers to optical data transmission, metrology, spectroscopy, laser material processing, and medical uses to free-space optical communications [Bar13]. However, despite their important advantages, they suffer from a significant drawback reducing their usage in either scientific or industrial applications: their multimode character and the spatio-temporal instabilities lead to a low spatial and temporal quality of the emitted beam [Hes95, Bur99, Raa02, Oht12, Agr13]. Many spatial modes are excited and present in the emission, especially in broad sources, due to the lack of an intrinsic mode selection mechanism. Furthermore, the strong nonlinearity of the active media, and the refractive index dependence on intensity, induce self-focusing effects that break the mode profile into multiple filaments. This drastically reduces the beam quality at high power emission and leads to spatial hole burning [Gol88, Die00, Rad11-2].

In broad semiconductor light sources, the origin of spatio-temporal dynamics is largely caused by modulation instability which is at the basis of spontaneous spatial pattern formation in many spatially extended nonlinear systems. It responds to the instability of the homogeneous solution by spatial modulations, leading to the growth of spatial modes generating stable and unstable patterns in a route to spatio-temporal behaviors and chaotic pattern dynamics. Their relatively low beam quality results in a less than optimal brightness and large divergence, which, in particular, prevents focalization and an efficient coupling to laser fibers thus, as above said, restricting their usage for many applications. The beam quality also plays an important role when the emitted light is used to pump another laser, such as solid-state lasers and fiber lasers.

1.1.1 Structure and properties

The characteristic structure of a semiconductor light source consists of a planar configuration of a (generally) double-heterostructure formed by a forward-biased heavily-doped p-n junction fabricated by two direct bandgap semiconductor materials (less current is the simple homojunction configuration). The main advantage of semiconductor optical sources is their high conversion

efficiency, precisely deriving from their planar configuration, enabling efficient access of the (electric current) pump to the whole volume of the active amplifying medium. Besides, other advantages are their compact design and affordable price. While homojunction lasers were reported back in the 60's, the first heterojunction laser dates from 1970 [Alf01, Loc70]. Since then, a large variety of laser structures have been developed guided by the performance requirements of specific applications.

Nowadays, a wide variety of semiconductor amplifiers and lasers can be found in the market. A semiconductor laser device may consist of a single emitter or contain multiple laser diodes. Wavelengths range from the ultraviolet, comprising all the visible spectrum, to infrared depending upon the bandgap energy, cavity length, and refractive index of the semiconductor, while the most common semiconductor lasers operate in the near-infrared. To achieve efficient recombination of electrons and holes, the carriers must be confined to the active layer [Yu96] which thickness (height) is around 100 nm. Within this layer occurs the radiative recombination of electrons and holes, being energy emitted as electromagnetic radiation.

For the case of lasers, the heterojunction active media are inside an optical cavity formed by cleaving two opposite facets of the semiconductor wafer, see Fig. 1.1 (a). No external mirrors are required since cleaved facets, which may also be coated to adjust their reflectivity by using dielectric multilayers, provide enough optical feedback. The laser threshold is reached when the injected pump current reaches a critical value, or threshold intensity (on the order of 100-150 mA), and gain overcomes cavity losses. Semiconductor laser sources do not employ any scheme for current confinement.

The typical architecture of semiconductor diode laser is around 1-3 μm thick (height, being the active region on the order of 0.1 μm), the width ranges from 50 μm to 400 μm (very large as compared to the emission wavelength, on the order of one micron) and 1-3 mm long. The emitting power ranges from hundreds of milliwatts [Gaw19] to tens of watts [Pas08], see Fig. 1.1 (a). While the most straightforward encapsulated semiconductor lasers show a circular geometry, see Fig. 1.1 (b) the first proposed semiconductor lasers had a narrow stripe geometry as in Figs. 1.1 (c) and (d), with an emitted power restricted to milliwatts, to prevent catastrophic optical damage. In Broad Area Semiconductor (BAS) light sources, also referred to as edge-emitting (EE) the output increases with the width. Due to the geometry, the highly multimodal emission occurs in the

horizontal axis, slow axis, which shows a small divergence. On the contrary, along the vertical direction, fast axis, the divergence is large due (on the order of tens of degrees) to the small size of the aperture of the order of few μm. Cause of this large divergence angle of the fast axis, the output light from the laser is generally collimated by placing a cylindrical lens of very short focal length at the output of the semiconductor material, also called Fast Axis Collimator (FAC). The emission in the slow axis strongly depends on the injection current since an increase of the injection current induces high-order mode oscillations, decreasing the beam quality.

Despite the beam quality issues, the high degree of efficiency, coupled with low lasing thresholds, and tiny, compact physical dimensions, Figs. 1.1 (b) and (d), make these lasers attractive for most devices where efficient power and/or space constraints are vital [Li00].

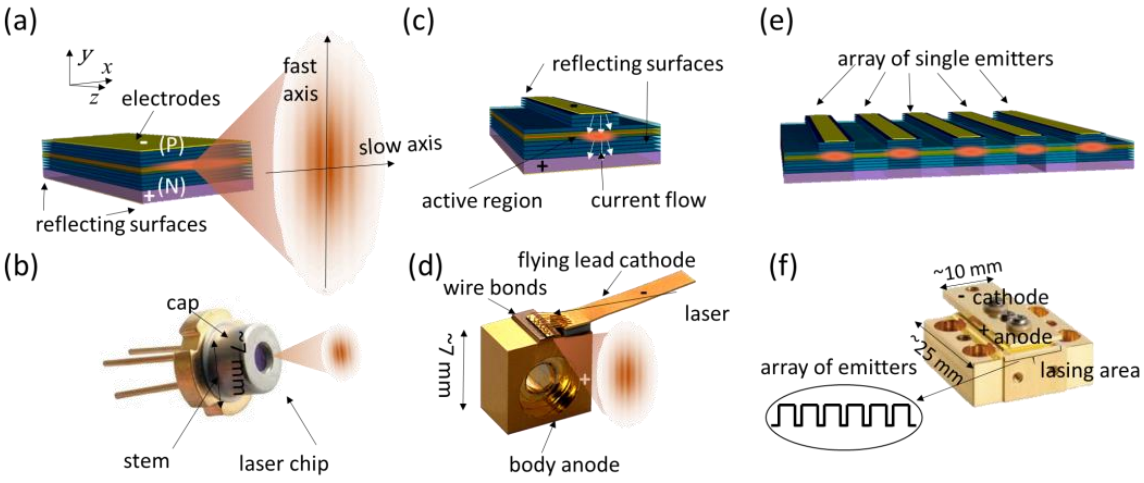

Figure 1.1. (a) Schematic illustration of single EEL. (b) Photography of an encapsulated diode laser (c) Schematic illustration of gain-guided EEL. (d) photography of gain-guided single EEL. (e) Schematic illustration of a bar of EELs. (f) Photography of a gain-guided bar of EELs.

A power-scaling approach is used in EEL bars to further increase the optical power, which can emit output powers of the order of hundreds of watts, see Fig. 1.1 (e) and (f). Diode laser bars (DLB) are linear arrangements of multiple broad area lasers mounted in a single package, usually consisting of 19 to 69 emitters along the slow axis, up to around 10 mm long. Each emitter has a well-defined width, and it is separated from the neighboring emitters by a distance called "pitch". The ratio of emitter width to the pitch defines the fill factor. Along the vertical axis (fast axis) the beam may be considered a point source, and the pitch between the emitters is small enough to consider that the radiation pattern along

the slow axis is a single line source [Li07]. Output powers exceeding 700 W in a continuous-wave regime have been demonstrated with single diode laser bars [Liu14]. Finally, DLB form multi-bar modules, in which the bars are arranged in the form of a stack.

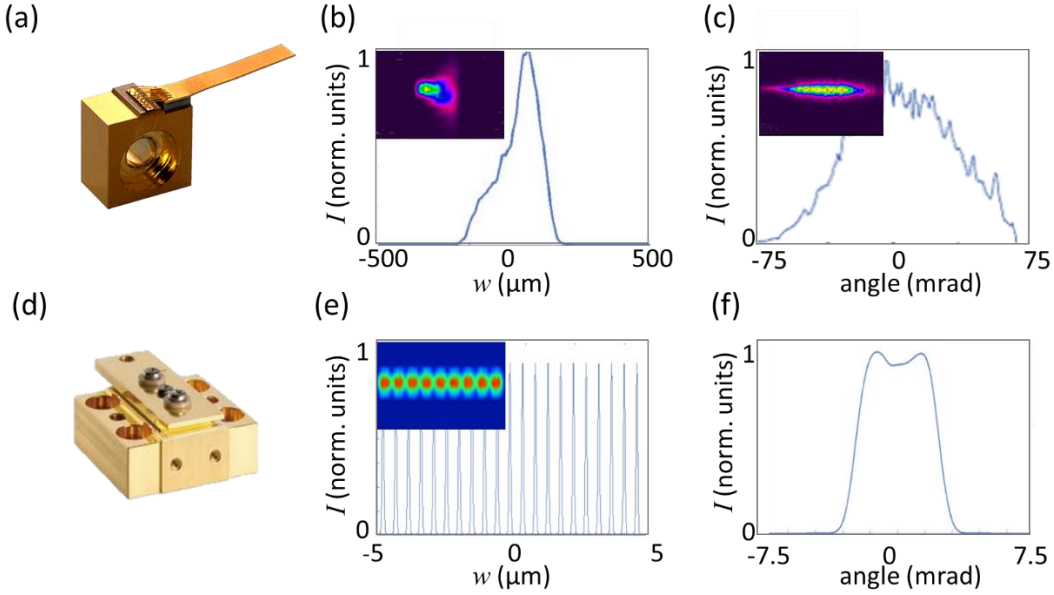

Figure 1.2. (a) Photography of an EEL. (b) Near field normalized output intensity of an EEL [Gaw19]. (c) Far field normalized output intensity of an EEL. (d) Photography of an EEL bar. (e) Near field normalized output intensity of an EEL bar. (f) Far field normalized output intensity of a bar EEL [Yu16].

Examples of the near field and far field emission from a single EEL and an EEL bar are provided in Fig. 1.2 We observe that the slow axis is highly multimode from a single emitter, eventually with an asymmetric beam profile, Fig. 1.2 (b). The far-field beam profile along the slow axis increases its width to support the larger number of modes, Fig. 1.2 (c). As for single EEL, the emission for EEL bars in the fast axis is nearly diffraction-limited, while in the slow axis, the beam quality is poor because of two reasons: the wide emitting aperture and the lightless areas between two adjacent emitters, see Figs. 1.2 (e) and (f).

1.1.2 Modelling the dynamics of EELs

As generally all lasers, semiconductor lasers comprise three principal elements: an optical cavity, an amplifying medium, and a pump mechanism. The optical cavity is generally created by two mirrors that provide longitudinal boundaries for light propagation. Two main types of optical cavities can be distinguished, ring and linear cavities. In the first, the electric field inside the cavity can be

described as a traveling wave, while in linear (Fabry–Perot resonators), the electric field is described as a standing wave, due to the interference between the forward and backward fields and requires accounting for both fields in the mathematical description. Lasers described in this thesis are of the second kind. The pump mechanism, being highly specific for each type of laser, has a common purpose: to create enough population inversion for lasing.

The laser amplifying medium can be solid, liquid, gas, or plasma involving two, three or even four electronic levels. Still, the majority of cases are well described by a two-level approximation, while additional levels help to achieve the necessary population inversion.

The wave equation is driven by the polarization of the medium and the Bloch-equations describing the dynamics of atoms in the gain medium lead to the well-known Maxwell-Bloch equations describing the laser dynamics. These relations are obtained from the laser theory, in the field of quantum optics and their derivation can be found in classic laser literature [Sie86, Sil96]. A didactic exposition of the semiclassical derivation of the Maxwell-Bloch equations can be found in [Val06]. The result is a relationship between the main physical magnitudes leading the laser dynamics, i.e. D, the population inversion of carriers o population difference in a two-level system, P, the polarization of the medium and E, the electromagnetic field classically described and driving the matter variables. Further, models of this spatially extended system should involve the longitudinal coordinate z, i.e. propagation direction of the field, plus one or two transverse coordinates and time. The model becomes a system of spatio-temporal partial derivatives of the three involved variables expanded in the 1D (mean-field models), 2D or 3D space and time. Therefore, the simplest approximation considers a uniform field in the whole cavity volume [Val06]. In this mean-field model, intertwined temporal dependences of variables can be expressed in a simple form:

$$\begin{aligned}
\frac{\partial E(t)}{\partial t} &= \sigma\ (P - E) \\
\frac{\partial P(t)}{\partial t} &= -\ (1 + i\delta)P + DE \\
\frac{\partial D(t)}{\partial t} &= -\gamma\left[D - r - \frac{1}{2}(E^{*}P + EP^{*}) \right]
\end{aligned} \tag{1.1}$$

These equations include the ratios between characteristic times of the three variables, $\gamma = \gamma_{\parallel} / \gamma_{\perp}$ is the ratio between the polarization characteristic time, $\gamma_{\perp}$, and the population inversion characteristic time, $\gamma_{\parallel}$, while $\sigma = \tau_k / \gamma_{\perp}$, where τ_k is the characteristic time of the electric field decay due to cavity losses. Other parameters are the relative pump $r = p / p_0$, where p_o is the threshold pump, $\delta = \frac{\omega_\alpha - \omega}{\gamma_{\perp}}$ the detuning between atomic resonance, ω_0 and the laser frequency, ω. When modeling we can disregard the specifics of the pump mechanism and describe it through the pump parameter.

Laser dynamics strongly depends on the characteristic times of these three variables that can have different orders of magnitude depending on parameters of the gain medium and the cavity configuration. The dynamics of Class A lasers, like gas and dye lasers, can be physically described by only one variable, the electromagnetic field, while population inversion and polarization show much smaller characteristic times than the field decay inside the cavity and are adiabatically eliminated.

In Class B lasers, the population inversion reacts slowly compared to field evolution, i.e. its characteristic timescale is larger than the intensity attenuation by cavity losses, while the medium polarization has short characteristic times and can be adiabatically eliminated. Thus, the dynamical description of Class B lasers is generally based on the interaction of two physical variables, the electromagnetic field and the population inversion. The slow evolution of carriers implies a strong reduction of the spontaneous emission in front of the stimulated emission, and therefore much larger efficiencies and emitted power can be reached. However, the more variables the richer the temporal dynamics, appearing in Class B lasers Hopf bifurcations, self-sustained oscillations, pulsed emission and chaotic behaviors. Class B lasers cover solid state lasers and some molecular lasers, e.g. CO_2 lasers. Semiconductor lasers and particularly EEL's to which this PhD is dedicated also belong to Class B lasers. They are applied in fields like medicine, material processing, technology, and communications, and cover 90% of commercial lasers nowadays. Finally, Class C lasers correspond to those with large characteristic times for the polarization, although they are less current and of smaller commercial interest.

To summarize, EELs are solid state class B lasers based on a semiconductor p-n junction as active gain material located inside a resonant Fabry-Perot cavity, directly pumped by in injection electrical current. As above mentioned, the cavity

mirrors are generated by the semiconductor's own front and back facets. For class B lasers, the polarization of the medium presents a much small characteristic time, it rapidly reaches a constant value and can be adiabatically eliminated from equations leading the field and carriers time evolution. Setting $\frac{\partial P}{\partial t}=0$, the system of equations of Eq. (1.1) becomes:

$$\begin{aligned}\frac{\partial E(t)}{\partial t} &= \sigma E\left[\frac{D}{1+i\delta}-1\right]\\ \frac{\partial D(t)}{\partial t} &= -\gamma\left[D\left(1-\frac{|E|^2}{1+\delta^2}\right)-r\right]\end{aligned} \tag{1.2}$$

where the field is averaged in the whole laser cavity as it is depicted in Fig. 1.3 (a).

The final relation between these variables depends on the laser characteristics. Specifically, for semiconductor lasers, the pump is a forward bias applied voltage across the p-n junction. Qualitatively speaking, the carriers (electrons and holes) are injected into the active layer and change the active-layer dielectric constant (both the real and imaginary parts). This affects the propagation of the optical mode which in turn affects the carrier distribution through stimulated recombination. Further, in EEL the small thickness of the active zone in between the p-n junction allows reducing one spatial dimension, strongly simplifying the numerical simulation and reducing the required calculation time.

Different models with more or less simplification have been presented, focused on the study of different characteristics of semiconductor lasers. Two main approximations are usually made, mean field approximations as the one explained above where variables are integrated in some or all spatial dimensions and in the other hand static models, where time is disregarded. Further simplifications can be done in specific semiconductor lasers as the adiabatic elimination of carriers. In the opposite direction, some reported models are more complex and include the majority of the aspects under study; however, they require complicated and time-consuming numerical methods [Rad11].

A more accurate mean field model for a semiconductor laser can be found in [Spi98, Lug99]. In this case, the semiconductor laser is a Fabry–Perot short microresonator. Applying the mean field limit integrating variables in the longitudinal coordinate *z*, and assuming only one cavity mode, the temporal evolution of the electric field amplitude and the population inversion is explored. Figure 1.3. (b) schematically represents this model type only considering

transverse field distributions. In this case, the interdependence between the carrier density N normalized to its transparency value and field is described by:

$$\begin{aligned}\frac{\partial E(x,y,t)}{\partial t} &= -\left[1+\eta+i\frac{1+i\delta}{1-\delta^2}\right]E + E_I - 2C\Theta(N-1)E + i\nabla_\perp^2 E \\ \frac{\partial N(x,y,t)}{\partial t} &= -\gamma\left[N + BN^2 - J + |E|^2 (N-1) - D\nabla_\perp^2 N\right]\end{aligned} \tag{1.3}$$

where the parameter η accounts for the linear absorption of the material; Θ is the cavity detuning; E_I is an external field injected into the cavity; C is the bistability parameter; γ is the nonradiative recombination rate of the carriers; B is the coefficient of the radiative recombination involving two carriers; J is the intensity of the pump current, normalized to its transparency value and D is the diffusion coefficient of the carriers. The transverse Laplacian operator $\nabla_\perp^2 = \partial^2/\partial x^2 + \partial^2/\partial y^2$ describes the field diffraction along the cavity in the paraxial approximation where the transverse coordinates are scaled to the square root of the cavity diffraction length and time is scaled to the photon lifetime in the cavity. Finally, $\Theta = (h+i)$, where h is the linewidth enhancement factor.

Other approximations model the longitudinal propagation of the electromagnetic field along semiconductor amplifiers in stationary regimes. For these models, the Slow Varying Envelope Approximation (SVEA) is usually considered where the electric field is written as $E(x,y,z,t) = A(x,y,z,t)e^{ikz-i\omega t}$ where A is the amplitude envelope of the electric field, k is the wavevector, and w the angular frequency that are constants. The simple case of EEL semiconductor amplifiers describes carriers N and the paraxial propagation of the slowly varying amplitude A along z [Ult06]. The carrier rate equation includes semiconductor nonlinearities, carrier diffusion, and spontaneous and Auger recombination coefficients. A linear dependence of the induced refractive index and gain on the carrier density may be assumed: $\Delta\varepsilon \sim \alpha(N'-N_0')$, where α is the gain parameter that includes scattering losses and N' the cladding-layer absorption and N_0' is the transparency level. The normalized equations for the optical field A and N can be expressed as:

$$\begin{aligned}\frac{\partial A(x,z)}{\partial z} &= \frac{i}{2}\frac{\partial^2 A}{\partial x^2} + (1-ih)NA - (1+\alpha)A \\ 0 &= D\frac{\partial^2 A}{\partial x^2} + J - N - BN^2 - CN^3 - (N-1)\left|A\right|^2\end{aligned} \tag{1.4}$$

where h is the linewidth enhancement (Henry factor) [Hen82]. The nonradiative recombination time is scaled to unity. For simplicity, carrier diffusion along propagation direction z is neglected. The carrier density is normalized to the transparency value N_0.

Another attractive static model, including both the axial and the lateral effects in a gain-guided semiconductor laser, is found in ref. [Agr84], that neither considers temporal laser dynamics. The model describes forward and backward waves in paraxial propagation for a single lasing mode by applying an effective-index approximation. The equation can be expressed as:

$$\begin{aligned} 2ik\frac{\partial A}{\partial z}+\frac{\partial^2 A}{\partial x^2}+k_0\Gamma\Delta\varepsilon A=0 \\ D\nabla^2 N=-\frac{J}{ed}+\frac{N}{\tau_{nr}}+BN^2+CN^3+\frac{g(N)}{\hbar\omega}|A|^2 \end{aligned} \tag{1.5}$$

where, $\Delta\varepsilon=\frac{-a\eta_\alpha RN}{k_0}-i\frac{\eta_\alpha}{k_0}[g(N)-a_{fc}N]+i\frac{\eta_p}{k_0}(1-\Gamma)\frac{\alpha_p}{\Gamma}$, Γ is the confinement factor for an active layer of thickness d, η_α and η_p are the background refractive indices of the active and passive layers, respectively, and $\Delta\varepsilon$ accounts for the passive-layer absorption and local gain increases linearly with carriers, $g(N)=aN-b$. The gain parameter, a_{fc}, is the free-carrier-absorption coefficient, and α_p is the passive-layer absorption coefficient.

The first term of $\Delta\varepsilon$ is related to the carrier-induced index reduction governed by the anti-guiding parameter R, the second term provides the gain after considering free carriers and material absorption, and the last term governs passive-layer absorption. The anti-guiding parameter R is known to play an essential role in gain-guided devices. Its value $R = -(2k_0/\alpha)(d\eta_\alpha/dN)$ is related to the active layer index change, primarily due to the absorption-edge shift with the carrier density.

For the carrier's equation, e is the electron charge, J depends on N through the lateral variations of the Fermi voltage at the junction of the active and p layers, $\hbar$ is the normalized plank constant, and ω is the angular frequency.

However, a complete picture of the spatio-temporal evolution of field and carriers in the semiconductor laser would consider coupled equations for the optical field and carriers in the 3D space and time [Böh08]. Due to the long transients presented by the system, this complete model is inefficient for

studying the laser dynamics or laser operation dependence on the model parameters, and it is limited to describe stationary behaviors. In the next chapter, we introduce a model for the spatio-temporal integration of the semiconductor laser that allows studying the field distribution in the laser cavity and its temporal evolution, scheme in Fig. 1.3 (c), as well as scanning the laser parameters.

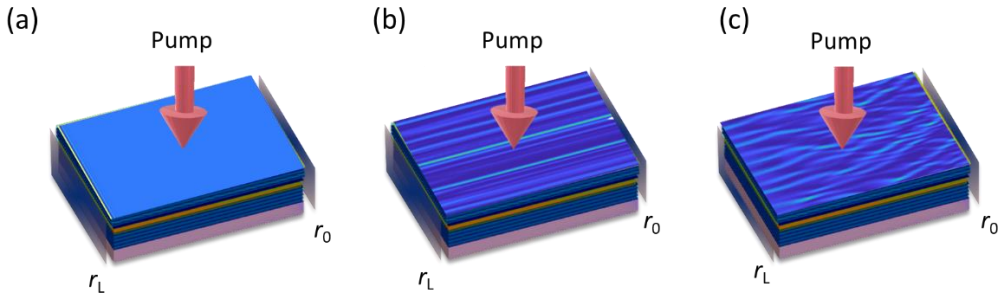

Figure 1.3. Schemes of a laser modeled by numeric equations where the electric field is defined as (a) $E(t)$, (b) $E(x, t)$ and (c) $E(x, z, t)$.

1.2 Emission performance of EELs

As discussed in the previous section, EELs present low brightness (parameter defined in the next section) —10 to 20 times worse than other high-power laser sources— due to their highly multimode emission in the slow axis. High brightness laser sources offer many benefits in terms of high beam quality, a longer field of focus and low divergence. There is a demand for high brightness diode lasers, particularly in the field of material processing and to pump other solid-state lasers.

Different possible approaches for the stabilization of either a single semiconductor laser or an EEL bar have been proposed. However, obtaining a stable emission from high-power EELs sources has remained a longstanding open question.

1.2.1 Beam Quality assessment

We briefly introduce the general concepts for the characterization and assessment of such beam quality.

The laser beam quality is commonly defined in comparison to the features of a perfect Gaussian beam. The basic equation describing the propagation of monochromatic beams with arbitrary field amplitude is given by the Helmholtz equation. When the optical beam is highly directional or we want to study the beam propagation only at the vicinity of a specific direction, we apply the small-angle or paraxial approximation to seek for simpler solutions. The Gaussian beam is, hence, the simplest solution to the paraxial wave equation describing the properties of the optical beam in the paraxial approximation. For a monochromatic Gaussian beam propagating along the *z*-direction, the complex field amplitude can be expressed as [Tei91]:

$$A(x,y,z) = A_0 \frac{w_0}{w(z)} e^{-(x^2+y^2)/(w^2(z))} e^{-i\left[kz+\frac{k(x^2+y^2)}{2R(z)}-\varphi(z)\right]} \tag{1.6}$$

where w_0 is the minimum beam radius, $w(z) = w_0\sqrt{1+(z/z_R)^2}$, the beam waist, and, in turn, z_R is the Rayleigh range, propagation distance along the propagation direction of a beam from the waist to the place where the area of the cross section is doubled, $z_R = \frac{\pi w_0^2}{\lambda}$; $R(z) = z\left(1+\left(\frac{z}{z_R}\right)^2\right)$ is the curvature, and $\varphi(z) = arctg\left(\frac{z}{z_R}\right)$ a phase term.

The beam waist at $z = 0$, w_0, corresponds to the minimum beam radius, see Fig. 1.4 (b). At this plane the radius of curvature of the wave front, $R(z)$, is flat. As the beam propagates through space, the beam radius at any position z along the beam is given by $w(z)$. The planar wavefronts of the Gaussian beam at the beam waist plane become curved as the beam propagates, acquiring parabolic profiles given by the radius of curvature $R(z)$, see Fig. 1.4 (a). The Rayleigh range is given by z_R, the beam radius at a distance z_R from the beam waist is a factor $\sqrt{2}$ larger and the intensity at the axis is decreased by a factor of two. The distance along the propagation direction where the beam is most confined, defined by the planes $z = \pm z_R$ is called the confocal parameter of the Gaussian beam. The divergence angle in the far field ($z \gg z_R$) is given by: $\theta = \frac{\lambda}{\pi w_0}$ The smaller the beam waist (w_0), the shorter the Rayleigh range, and larger the divergence angle. So tightly focused Gaussian beams tend to diverge very fast in the far field.

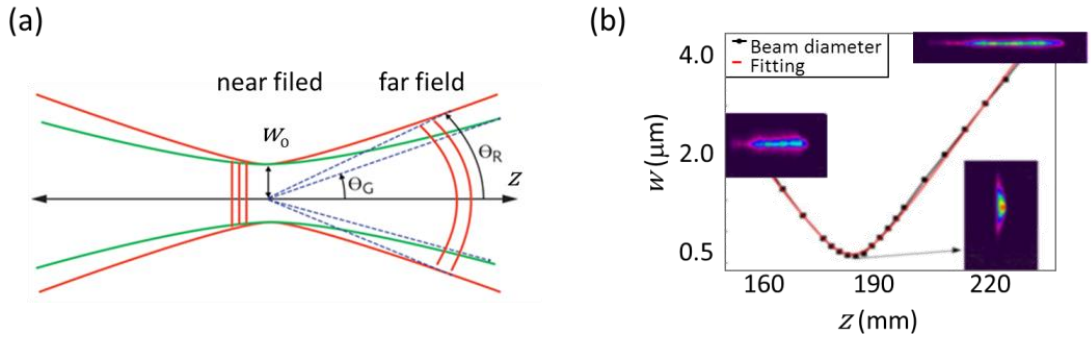

Figure 1.4. (a) Comparison between the laser beam divergence of an actual beam (in red) and an ideal Gaussian beam (in green), the beam's wavefront is planar in the near field near the beam waist and curved in the far field. (b) Experimental measurement of the beam width measured at different positions along the propagation direction (black dots) and fitted beam waist equation (in red) [Gaw19].

The Gaussian beam is not the only solution of the paraxial wave equation. Other high-order mode solutions can be expressed using Hermite-Gaussian modes (rectangular coordinates) or Laguerre-Gaussian mode (cylindrical coordinates). Actually, the beam emitted from semiconductor laser edge-emitting laser is highly multimode in the horizontal (slow axis); each mode being a quasi-Gaussian mode. All these modes combine to form the multimode beam. As all the modes propagate, they grow in size and merge with other modes to form a line in the far field. Such beam cannot be well collimated neither focused down to a smaller spot.

Gaussian beam emission is assessed by the parameter product (BPP). The BPP of a diffraction-limited beam is given by product of divergence angle and beam waist, BPP = $w_0\theta$. A lower BPP means a better beam quality. The BPP can be different, for non-diffraction limited beams, along vertical and horizontal directions and it is used to define the spatial quality of the beam. For semiconductor lasers, the BPP along the two axes is quite different, being low for fast axis and high for slow axis.

Another parameter of interest is the beam quality factor, M^2, which is defined as the beam parameter product of the measured beam divided by the corresponding product for a diffraction-limited Gaussian beam.

$$M^2 = \frac{BPP_{actual\ beam}}{BPP_{Gaussian\ beam}} = \frac{\pi w \theta}{4\lambda} \tag{1.7}$$

For a diffraction-limited Gaussian beam, the beam parameter product is BPP = λ/π, which is close to 1. The minimum focusing spot size that can be achieved with a given laser beam for a given divergence depends on the beam's factor. Lower factors correspond with a tighter focus, a more efficient use of the power within the beam, and a higher potential effective power of the laser. Focusing laser beams tightly is particularly important, for example, when using lasers for imaging, since a smaller beam waist means higher power densities, as well as better resolution.

For higher-order non-diffraction limited beams such as EELs, both the BBP and the M^2 factor can be significantly different in two perpendicular directions (x-horizontal direction and y-vertical direction). Namely M_x^2 and M_y^2 are the factors the beam quality factor along horizontal (slow axis) and vertical direction (fast axis). Thus, the brightness for EELs is defined as the output power divided by both factors [Sum09]:

$$B = \frac{P}{\lambda^2 M_x^2 M_y^2} \tag{1.8}$$

where P is the average power of the beam. The brightness can be enhanced either by increasing the optical power or by decreasing M_x^2 and M_y^2 values. In semiconductor lasers, due to low mode selectivity of Fabry-Perot cavity, it results in higher order transverse modes emission. For EELs having widths of several hundreds of microns, M_x^2 is in the order of 100. The M_x^2 can be decreased by reducing the far field divergence angle, and decreasing the width of the active region.

1.2.2 Conventional techniques to improve the beam emission

A direct way to clean up a beam is by removing the high-order modes. Conventionally, the simplest filtering scheme for noisy beams consists on a pinhole in the focal plane, see Fig. 1.5 (a). The resulting quality of the filtered beam depends on the incident beam and the diameter of the pinhole. The smaller the pinhole, the better the beam quality, however, this entails a severe reduction of the power.

Various proposals have been presented to improve the spatial emission from broad EEL. One approach is to use optical injection to stabilize the intrinsic transverse instabilities [Pak17]. Other proposals use external resonators to

provide feedback, via 4f cavities with a spatial frequency filtering configuration or an unstable cavity with convex external mirrors to achieve a fundamental mode operation [Wol99, Wol00, Sal85], see Fig. 1.5 (b). Another strategy is to introduce phase-conjugated feedbacks [DeT97]. In all these solutions, external elements compromise the device's robustness while it becomes less compact, also power is lost, lowering the emitted brightness.

Yet another possibility is a distributed feedback laser, a type of laser that has a structure that provides optical feedback. A longitudinal diffraction grating with periodic changes in refractive index can be used to cause reflection back into the cavity. The periodic change can be either in the real part of the refractive index, or in the imaginary part [Tur10]. Moreover, it has been shown that the periodic modulation of pump profile in the transverse and longitudinal directions can lead to spatial filtering and stabilization effects in EE amplifiers [Her12, Rad13], as seen in Fig. 1.5 (c). Possible stabilizations of EE sources under specific working conditions are proposed by introducing spatial [Kum14, Her12] or spatio-temporal modulations [Hal62]. These schemes have a compact and efficient design to control spatio-temporal dynamics.

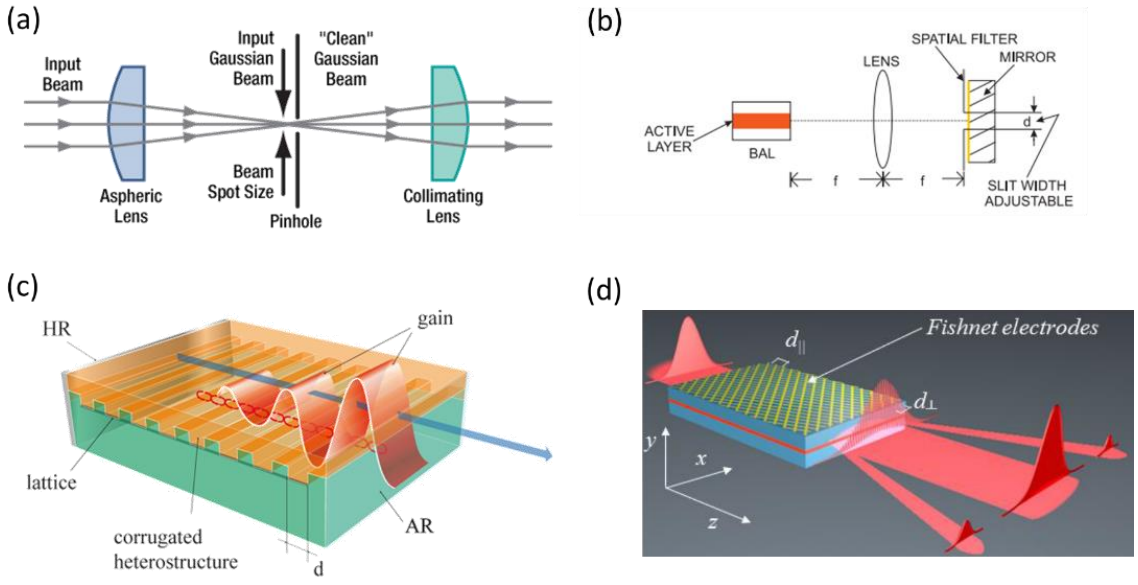

Figure 1.5. Schemes of improving EEL beam emission: (a) external filtering scheme with a pinhole, (b) optical feedback [Wol99], (c) distributed feedback laser [Tur10] and (d) periodic modulation of the pump profile [Her12].

1.2.3 Improving the performance of EEL bars

Various beam shaping techniques have been presented to improve both the beam quality of every single emitter within the EELs bars, also reducing the lightless areas between two adjacent emitters. The introduction of an optimized beam transformation lens system can allow small focus diameter and improve its beam quality [Yu16], Fig. 1.6 (a). Other techniques include external phase masks to achieve a single-lobe spot [Ste07], or use holographic feedback [Iid98]. Another proposed concept was extending wavelength-multiplexing techniques with external cavities to spectrally superimpose the beams of a semiconductor array into one [Jec06], Fig. 1.6 (b). However, again external elements compromise the device's robustness and compactness.

A method that overcomes the problems associated with external feedback solutions, such as high order mode energy loss and energy efficiency proposed using notions of supersymmetry [Hok19], Fig. 1.6 (c), using a non-Hermitian potential in a different way as it is proposed in the present thesis. In P. Hokmabadi and coauthors proposal the main array is paired to a lossy super-partner. Apart from the ground state, all high-order modes are coupled to the supersymmetric lossy array whose role is to suppress all undesired higher-order modes while simultaneously enhancing the gain seen by the fundamental supermode of the primary lattice.

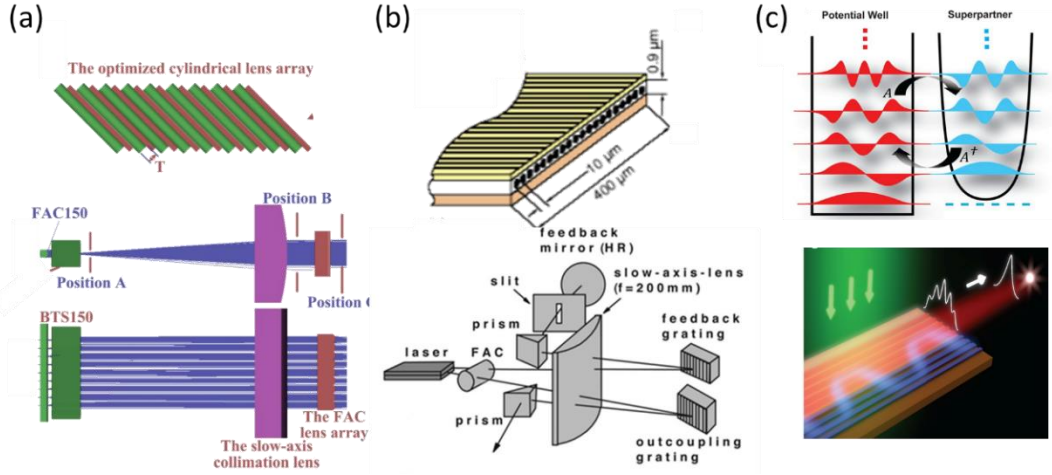

Figure 1.6. Schemes of improving EEL bar beam emission: (a) cylindrical tailored lens arrays [Yu16], (b) wavelength-multiplexing techniques [Jec06], and (c) supersymmetric EEL bar in the upper the gain array and lossy partner array are shown [Hok19].

1.3 Periodic systems beyond Photonic Crystals

The advent of artificially structured materials on micro- and nanometer scales has become a fruitful playground to uncover novel physical phenomena due to their ability to tailor the propagation and generation of light even in exotic or counterintuitive ways. In 1987 two papers published in the same Physical Review Letters volume by Eli Yablonovitch and Sajeev John, respectively showed that a modulation of the index of refraction on the wavelength scale could either inhibit the spontaneous emission or localize light [Bus98, Joa11]. Since then, periodic dielectric structures have been referred as Photonic Crystals (PhC), for their ability to modify the dispersion relation of photons similarly as a periodic potential in a semiconductor crystal determines the energy bands that affect the motion of electrons. Yet electrons follow Fermi-Dirac distribution while photons obey Bose-Einstein distribution. Hence, the analogy has limitations. In fact, PhCs were also initially known as photonic BandGap (BG) materials. Diverse applications of PhCs rapidly derived precisely from the modification of such temporal dispersion: frequency filtering — also responsible of the structural color in nature in butterflies and weevils —, optical demultiplexing, rainbow trapping in chirped structures —with a varying period—, routing and bending light in PhCs waveguides or PhC fibers, light confinement or localization —as a defect in a PhC may be a completely shielded trap for light localization—, for energy harvesting in solar cells, or to enhance nonlinear phenomena [Sou12].

However, soon attention was also paid to the ability of PhCs to modify not only to the temporal dispersion but also to shape the spatial dispersion leading to spatial effects —in at least 2D architectures—. Therefore, PhCs allow beam shaping effects [Mai10], such as self-collimation and flat lensing due to negative diffraction or spatial filtering —this latest effect is used in Chapter 2 of this Thesis, as discussed below in more detail.

Later, similar beam shaping effects were also demonstrated in seemingly analogous artificial materials, where not the real part but rather the imaginary part of the permittivity profile —gain/loss profile— [Kum12]. However, pure dielectric PhCs and gain/loss structures are two limiting ideal situations and more interesting physics arises from the interplay of both modulations, real refractive index and gain/loss.

Other unusual, exotic and even counterintuitive phenomena are the cause of the recent focus on the more general class of periodic non-Hermitian optical systems holding modulations of the complex permittivity as described in section 1.3.1.

Worth mentioning that since 1987, the technological available fabrication techniques have noticeably advanced. The tedious layer-by-layer construction of the first 3D woodpile PhC —of only 1.25 periods — lasted months, while with direct laser writing it is possible in minutes — as it is the case with PhC used in Chapter 2 of this thesis [Gaw20] — along with the flexibility to combine different materials.

1.3.1 Mode coupling in periodic complex systems

The simplest one-dimension (1D) realization of a PhCs is also known as a Bragg reflector —consisting on a multilayered stack of alternating refractive index materials of widths $\lambda/2n_i$, being λ the wavelength of light and n_i; i=1,2 the refracting index of the two materials—. Alternatively, we may consider $n(x) = n_0 + n(x) = n_0 + n_{Re}\cos(qx)$, a simple harmonic modulation index profile where q is the wavenumber (reciprocal lattice vector) of the modulation, see Figs. 1.7 (a).

In such 1D dielectric arrangement, the formation of photonic bands can be straightforwardly explained in terms of destructive interferences within the material, due to the accumulated phase shift in the partial reflections from successive layers. Consequently, when light propagates perpendicular to the modulation, there is a continuous bandgap —stopband— or range of light frequencies unable to propagate through the PhC, close to the resonance condition $k = q/2$. Therefore, light may be completely back reflected for a perfect infinite structure or, more precisely, decay exponentially for actual finite structure leading a strong reduction in transmission —of orders of magnitude with just a few periods, depending on the index contrast. In other words, a PhCs modifies the density of states of light at every point within it, see Figs. 1.7 (a-c) [Bot09].

Analogous 1D periodic structures are Gain-Loss Modulated (GLM) materials, where the gain and loss are spatially modulated periodically on the wavelength scale, see Fig. 1.7 (d). Yet the refractive index is constant, assuming, for example a complex refractive index profile in the form: $n(x) = n_0 + i\,\Delta n(x) = n_0 + i\,n_{Im}\sin(qx)$. The dispersion of such structures can be analyzed by an extended plane wave expansion for an infinite structure [Boy19], allowing for complex

eigenfrequencies, see Figs. 1.7 (b) and (e). The real part of the eigenvalue represents the frequency, while the imaginary part determines the temporal growth or decay of the corresponding mode. Close to resonance, $k \approx q/2$, instead of opening a BG, modes pull each other and lock and the imaginary part becomes non-zero. As a result, the presence of a growing mode within this locked-frequency range the presence of a growing mode leads to an enhanced transmission or anti-bandgap at resonance, see Figs. 1.7 (e) and (f) where we observe both a transmission and reflection enhancement.

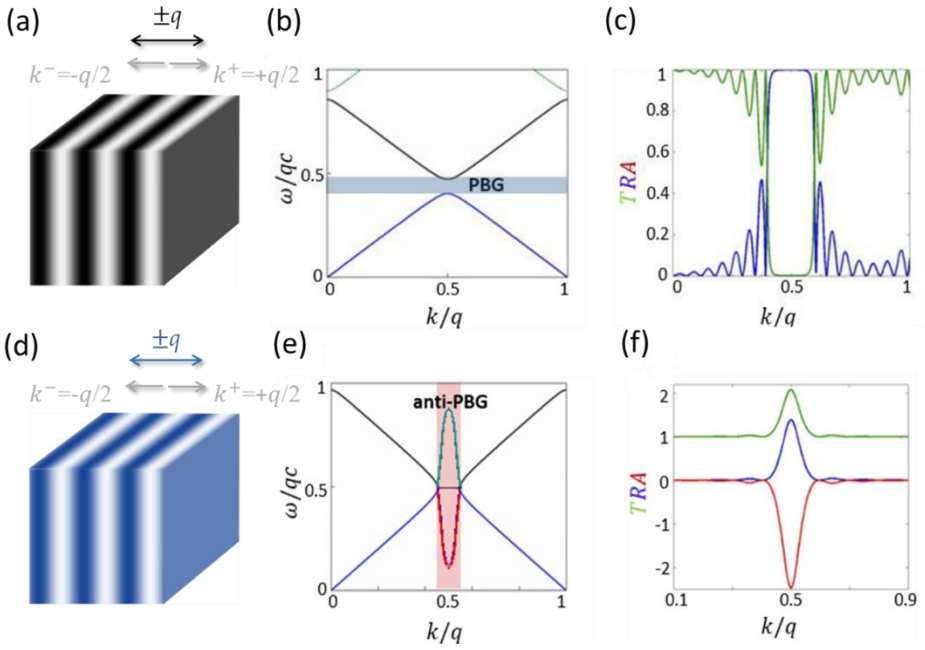

Figure 1.7. (a) Scheme of 1D PhC with a harmonic index modulation $n(x) = 1 + 2\cos(qx)$. (b) Dispersion relation obtained by plane wave expansion for an infinitely extended structure; (c) numerical transmission, T, and reflection, R, as obtained by transfer matrix method for a five periods structure. (d) Scheme of 1D GLMM made of two different materials $n_1 = 1 + i\,0.2\sin(qx)$. (e) Complex dispersion relation obtained by extended plane wave expansion for an infinite structure [Bot10]; (f) numerical transmission, T, and reflection, R, as obtained from a discretized multilayer structure by transfer matrix method, for ten bilayers.

In 2D GLM structures, the directional gain leads to different interesting spatial effects such as spatial filtering self-collimation [Sta09], and flat lensing [Kum13]. Note that while the coupling mechanism in GLM materials differs from PhCs in both cases it is symmetric, meaning reflection does not depend on the propagation direction of light.

Next, we analyze the situation when both refractive index and gain/loss modulations are present but not in phase but shifted a quarter of the wavelength of the modulation. When both modulations are balanced, such a system is a classic analog of a quantum system invariant under Parity (P-) and Time (T-) known as a PT-symmetric system [Ben98]. The simplest harmonic PT-symmetric complex index profile may be described as: $n(x)= n_0+ n_{Re} \cos(qx)+ i\, n_{Im} \sin(qx)$, with $n_{Re} = n_{Im}$. While such a system may be regarded as a superposition of a PhC and a GLM structure, a new exotic property of unidirectionality arises. That is to say, reflection from a finite PT-symmetric structure may not be symmetric close to resonance, being attenuated from one side while enhanced from the other side [Guo09, Lin11], while the transmission is constant, see Fig. 1.8.

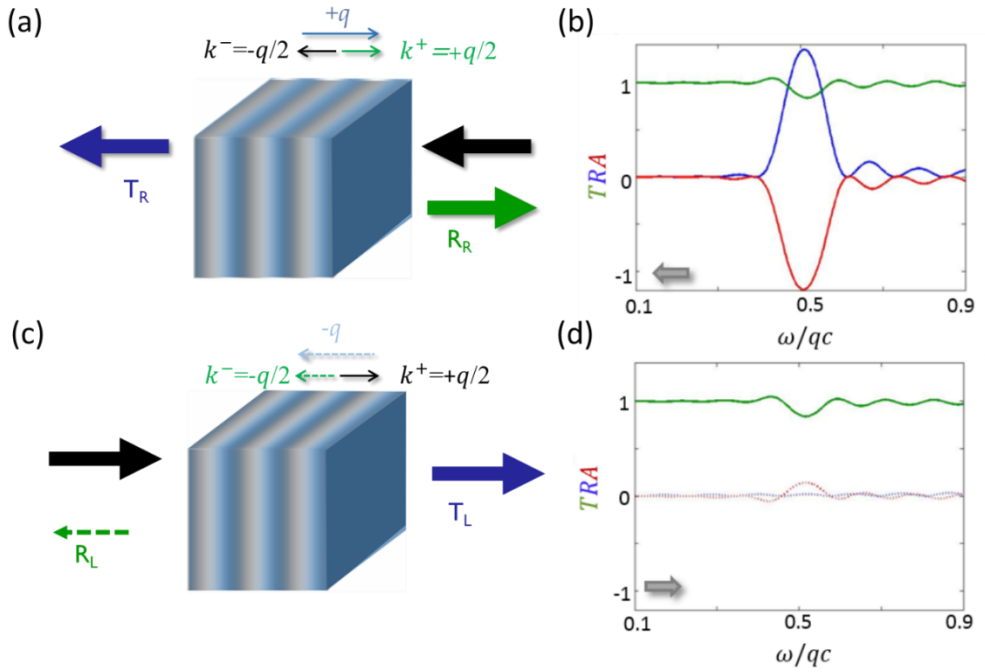

Figure 1.8. Unidirectional reflection, transmission and absorption from a simple discretized multilayered structure equivalent to the harmonic modulation: $n(x) = 1.1 + 0.1\, e^{iqx}$ as numerically obtained by the transfer matrix method. When (a) light is incident from the right, reflection, R_R, is high; when light is incident from the left, reflection, R_L, cancels at resonance, i.e, for light with a wavevector $k = \omega/c = 2q$ being q the wavenumber of the modulation. Note that transmission, T, is the constant irrespectively of the direction of the propagation of light.

A simple explanation for the different behaviors of Figs. 1.7 and 1.8 may be provided inspecting the mode coupling. The simple PT-symmetric complex profile considered may be more conveniently expressed as $n(x)= n_0+ n\, e^{iqx}$ where n is the amplitude of the complex index modulation. Clearly, such a modulation unidirectionally couples a wave with a wavevector k^- to $k^+= k^- + q$. In the right

column of Fig. 1.8 (a), a left-propagating resonant wave, $k^- \approx -q/2$, is coupled to $k^+ = k^- + q \approx q/2$ and is thus Bragg-reflected to the right. On the contrary, the above-considered real-valued 1D PhC, Fig. 1.7 (a) with harmonic potential, $n(x) = n_0 + n_{Re} \cos(qx) = n_0 + n_{Re}/2\ (e^{iqx} + e^{-iqx})$ symmetrically couples, at resonance, $k^+ \approx q/2$ with $k^- \approx -q/2$. In fact, the wavenumber $+q$ couples k^- to k^+ , yet $-q$ couples k^+ to k^-, as schematically illustrated in Fig. 1.7 (a). Exactly the same situation is found for the harmonic GLMM with complex profile $n\ (x) = n_0 + n_{Re} \sin(qx) = n_0 + n_{Re}/2\ (e^{iqx} - e^{-iqx})$; also, in this case, the presence of both lattice vectors $+q$ and $+q$ warrants symmetric mode coupling, see Fig. 1.7 (d). In this way, the 1D PT-symmetric modulations given by PT-symmetric complex modulation break the symmetry of left-right wave coupling and propagation [Tur15].

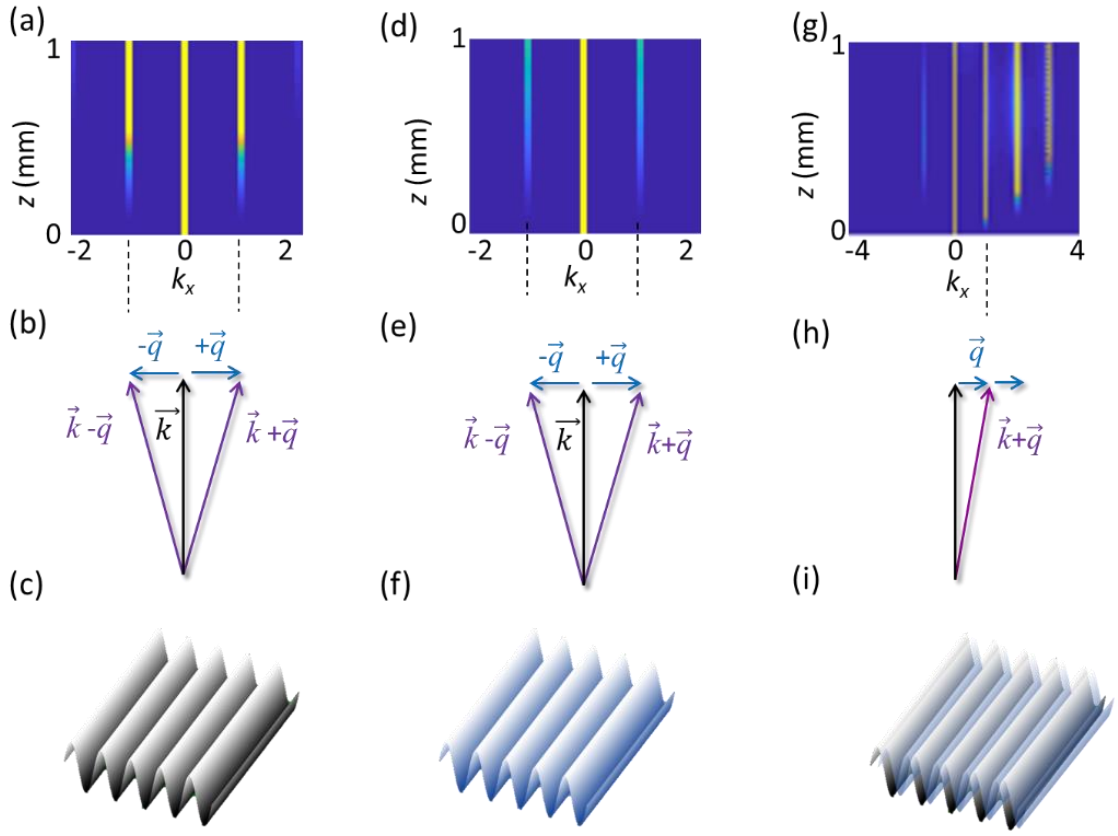

Fig. 1.9. (a) Spectral propagation of a Gaussian beam in a refractive index modulated EE amplifier. (b) Possible coupling of wavevector, $\vec{k}$, with the modulation vector, $\vec{q}$ for a PhC sinusoidal potential. (c) The sinusoidal periodic potential of the refractive index. (d) Spectral propagation of a Gaussian beam in a modulated gain EE amplifier. (e) Possible coupling of wavevector, $\vec{k}$, with the modulation vector, $\vec{q}$ for a gain sinusoidal potential. (f) The sinusoidal periodic potential of the gain/loss. (g) Spectral propagation of a Gaussian beam in a modulated complex index EE

amplifier. (h) Possible coupling of wavevector, $\vec{k}$, with the modulation vector, $\vec{q}$, for a shifted refractive index and gain sinusoidal potential. (i) Sinusoidal periodic potential of shifted refractive index and gain. Numerical simulations are performed using the model presented in Chapter 3 and adding the corresponding potential.

Analogously, when light propagation direction is not transverse to the modulation of the periodic structure but longitudinal propagation the asymmetric structure may couple wavevector of light $\vec{k}$ with $\vec{k} \pm \vec{q}$, being $\vec{q}$ the reciprocal lattice vector. In Fig. 1.9 we numerically propagate a Gaussian beam with a central wavevector $\vec{k}$ and analyze the Fourier spectrum of the propagated beam, observing the energy transfer to neighboring modes.

We can observe that either for a purely real-valued refractive index and for a purely imaginary gain/loss modulations the beam interacts with potential along the propagation and the energy couples the central mode $\vec{k}$ to higher-order harmonics of the modulation. As expected, in both cases, the spatial spectrum of the field shows the symmetric coupling between the modes, $\vec{k} \pm \vec{q}$, see Figs. 1.9 (a) and (d). For the PT-symmetry complex potential the field spectrum clearly indicates an asymmetric energy flow between the modes towards: $\vec{k} + \vec{q}$, $\vec{k} + 2\,\vec{q}$, $\vec{k} + 3\,\vec{q}$, ... see Fig. 1.9 (g), as will be explained in more detail in Chapter 4, section 4.1.

1.3.2 Spatial effects in 2D PhCs

In turn, novel spatial propagation effects arise in artificially modulated photonic structures that engineer the spatial dispersion, see Fig. 1.10 (a). Indeed, periodic modulations of the complex refractive index can shape monochromatic beams. The distortion of the spatial dispersion accounts for the effect, and at least 2D architectures are required. In free space, the isofrequency contours are perfect circles, and the concave curvature introduces a phase delay between wave components leading to a broadening of a propagating beam, yet when such curvature is flat, a beam can propagate without broadening (self-collimation), and concave isofrequency contours (negative diffraction) may lead to focalization after the accumulated space is compensated in free space, see Fig. 1.10 (b) [Sta09, Bot10, Kum12, Kum13].

Among the beam shaping effects is the angular filter [Mai15]. While the celebrated BG in temporal dispersion may be used for frequency (chromatic filtering), spatial filtering is also possible thanks to the formation of angular BGs. For given propagation wavevectors and particular angles waves cannot

propagate, in other words, there is a stop band in the spatial dispersion domain, see Fig. 1.10 (c). The plane wave components that corresponds to this angular BGs may be reflected back in the Bragg regime (or deflected in Laue regime) and consequently removed from the angular spectrum of a forward propagating beam, see Fig. 1.10 (d). The use of PhC for filtering is becoming a known method in optics since proposed 15 years ago [Tan06, Tan07, Sta09, Ser09, Col10, Mai10, Mai15, Gai16].

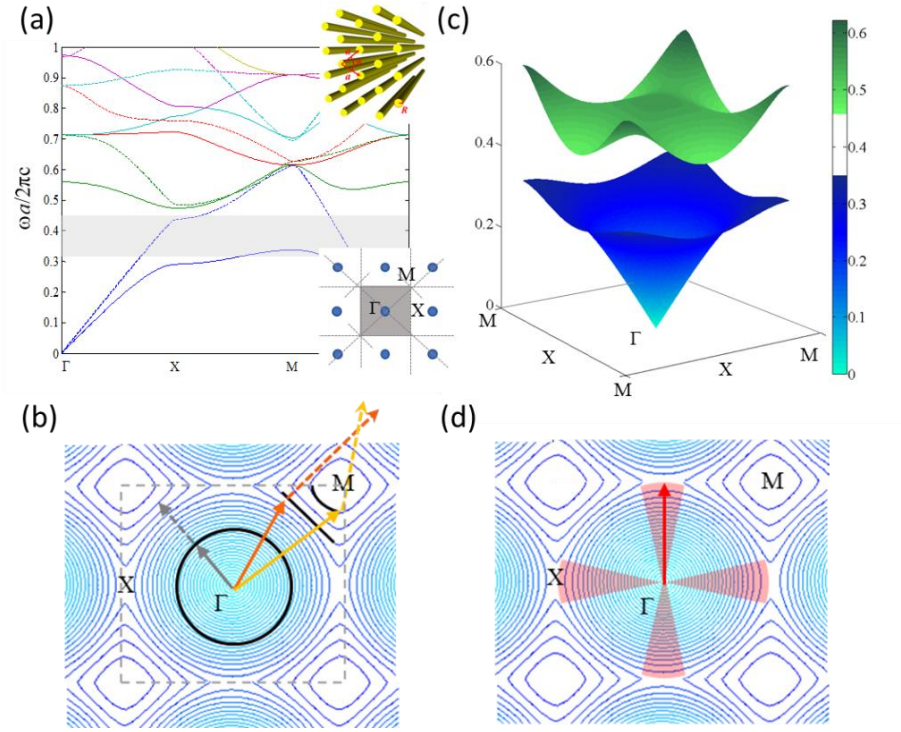

Figure 1.10. (a) Bands structure for TE (solid) and TM (dotted) polarizations determined as an eigenvalue problem —for the frequency— of a 2D structure made of cylinders in a square lattice, by solving Maxwell's equation with Bloch's theorem — solutions invariant under translation of a lattice vector —, folded into the first Brillouin —the shaded region indicated in the lower inset—. The capital letters represent the lattice directions. (b) First and second bands for TE polarization showing the BG for this polarization. (c) Isofrequency contours of the first band showing a change of curvature approaching the high symmetry point M. The red arrow corresponds to normal diffraction, the orange to self-collimation and the yellow to negative diffraction. The black arrows indicate the direction of the group velocity. (d) Isofrequency contours of the first band showing the angular BGs for the wavevector marked as the red arrow at the high symmetry point X.

In 2D PhCs geometry of the fabricated structure is characterized by its longitudinal and transverse period and corresponding wavenumbers $q_{\parallel}$ and $q_{\perp}$.

In this kind of structures there is a coherent transport of radiation from the fundamental or zero component, $\vec{k}$, to the diffracted component, $\vec{k} + \vec{q}$. Therefore black line appears in transmission corresponding to the resonance condition $k_x/k_0 = q_{\parallel} / q_{\perp} - q_{\perp}/(2k_0)$, Fig. 1.11 (a). [Mai10].

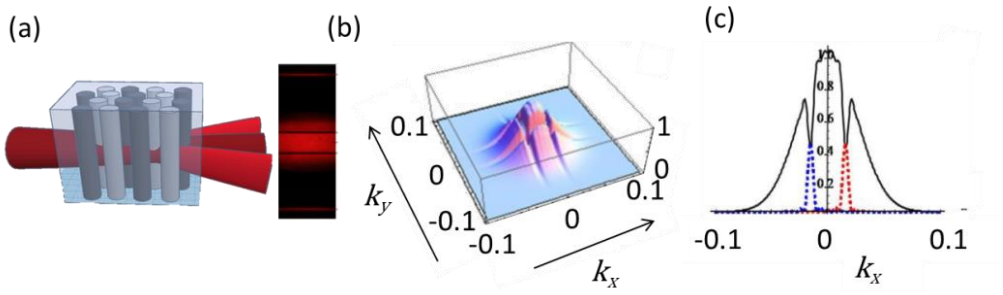

Figure 1.11. (a) Schematic representation of experimental measurement, focused laser beam provides a wide range of angular $k^{\rightarrow}$ components incident to the PhC. Some of the $k^{\rightarrow}$ components are deflected to the diffraction maxima and the rest passes through unaffected. (b) Filtered beam spectrum. (c) Experimental horizontal cut obtained by numerical integration with the parameters: $m = 2{\cdot}10^{-4}$, $q_{\perp} = 0.25$, $q_{\parallel} = 0.035$, and normalized propagation distance $z = 4{\cdot}10^{3}$, k_x is normalized into k_0 [Mai10].

Figure 1.11 shows for a schematic representation of a single-pass spatial filtering. After the beam passes along the sample of Figs. 1.11 (a) and (c) it is possible to observe the black filtered parts of the spatial spectra, corresponding to the four crossing lines, Fig. 1.11 (b), each line corresponding to the coupling with a particular diffraction component.

The angular position and width of the lines can be controlled by varying the parameters of the photonic structure. One interesting structure is chirped PhC, which are structures with gradually increased or decreased periods [Oue87]. Chirping can also be achieved by a slowly-varying the refractive index gradient [Lou05]. Since the BandGap (BG) frequency depends on the structure period, in a chirped PhC, where the period gradually varies, the BG frequency range moves along the structure, broadening the total BG. In Chapter 2, we propose using an analogous resonance condition for a chirped PhC for spatial filtering.

1.3.3 Non-Hermitian Photonics

The introduction of the concept of PT-symmetry has triggered an intense research activity leading to the development of the new field of non-Hermitian Photonics [Fen17]. First regarded as a curiosity in the frame of Quantum

Mechanics, as non-conservative systems that could still present real eigenvalues [Ben98]. PT-symmetric systems have found feasible realizations in the field of optics. The first experimental observation of passive PT-symmetry breaking in optics was reported by Guo et al. in 2009 [Guo09], demonstrating loss-induced optical transparency. Already in 2010, Rüter demonstrated asymmetric transport of light, including an active media. Spontaneous PT-symmetry breaking and oscillations that violate left-right symmetry were observed in coupled waveguides with gain and loss, see Fig. 1.12 (a). The concept was applied to large-scale unidirectional lattices hinting that PT-symmetry could lead to a new generation of multifunctional optical devices and networks see Fig. 1.12 (b) [Reg12]. Since then, the field has been exponentially growing, coinciding with the advances in nanofabrication techniques. Simultaneously, other relevant experiments and proposals were reported, and other PT-symmetric optical structures and configurations were proposed [Lin11, Lon11, Fen12, Jia15]. Thus, optics has become the ideal playground to experiment and uncover the new physics of non-Hermitian systems, offering a novel tool to control and tailor light [Zia14, El-G18].

In the more general case of non-Hermitian photonics, the interplay between real and imaginary parts of the potential may lead to exotic features arising from an unusual mode coupling symmetry breaking. Applications range from cloaking arbitrary objects [Lon11, Hay18, Hay18-2], to tailoring the filed flows in arbitrary dimensions. In fact, general non-Hermitian systems holding asymmetric wave flow may be designed with a generalized Hilbert Transform (HT), analogous to the Kramer's Kronig relations that break the temporal symmetry, which is at the basis of causality [Ahm18-3]. Other fascinating and exotic proposals include optical isolators, optical modulators, optical switches, coherent perfect absorbers -antilasers-, optical diodes, sensors to new effects in topological photonics, and it is even possible to create non-casual systems by adding either nonlinearities or a magnetic response.

Since light amplification, gain, and optical absorption, loss, are inherent properties of the lasers, they become an ideal platform to prove and study non-Hermitic effects. In the early studies, effort was only put into lowering the dissipation to improve these devices' performance. Recently, the new proposals in non-Hermitian optics provide a background to explore exotic regimes in laser systems. An interesting field of application is coupled micro-ring cavities, and microring lasers and laser arrays. A particular recent example reported by

Hodaei et al. two directly coupled identical microring-cavities presented were used to achieve a stable single–longitudinal mode operation, in Fig. 1.12 (d). In turn, it was demonstrated that a laser array system could significantly improve the lasing response and output beam quality. Hokmabadi et al. explored this possibility in a coupled microring system in which a standard laser array is coupled with its dissipative super partner array with unbroken supersymmetry, see Fig. 1.12 (e). Finally, some studies even study PT-symmetry exceptional points at higher orders. This is of high interest since it can enhance the sensitivity of resonant optical structures to an external perturbation, see Fig. 1.12 (f). In this line, Hodaei et al. presented a ternary PT-symmetric photonic laser molecule.

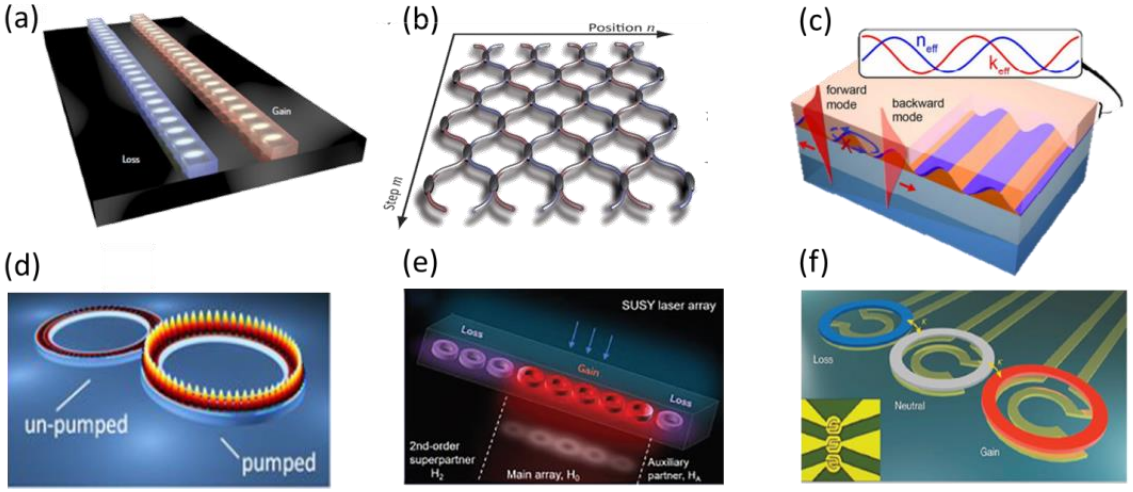

Figure 1.12. Experimentally demonstrated optical PT-symmetric systems. (a) Gain-loss waveguides, with unidirectional light transport [Rüt10]. (b) PT-symmetric temporal lattice formed by two coupled fiber loops periodically switching between gain and loss [Reg12]. (c) Asymmetric behavior in a passive PT-symmetric organic thin-film metawaveguide [Jia15]. (d) PT-symmetric coupled whispering-gallery microresonators [Hod14]. (e) Non-Hermitian supersymmetry-based laser array depicting active main array (red), and super-partner array (purple) [Hok19]. (f) Ternary PT-symmetric photonic laser molecule where the middle microcavity is without gain/loss and the adjacent sites have balanced gain and loss [Hod17].

Nearly one century after the birth of Quantum Mechanics, the classical optical platform of non-Hermitian Photonics is deepening our understanding of fundamental quantum physics revolutionizing and extending quantum theories and facilitating technological breakthroughs for photonic applications [Fen17].

Chapter 2

Intracavity filtering Edge-Emitting Lasers

This PhD aims to study mechanisms to improve the performance of Edge Emitting (EE) amplifiers and lasers. For this purpose, we need a versatile model with sufficiently short integration times to model the spatio-temporal dynamics of the system in its parameter space. Thus, in this Chapter we develop a specific new approach, including the spatial distribution and the temporal evolution of both fields and carriers that will be used throughout the thesis.

The model is used to numerically demonstrate the intracavity filtering of the multimode emission of EE Lasers (EELs) with chirped Photonic Crystals (PhCs). The results of this Chapter are published in Ref. [Gaw20]. The reported excellent agreement between predictions and experiments confirms both the proposed filtering scheme and the model.

2.1 Spatiotemporal models for edge-emitting amplifiers and lasers

Chapter 1 summarizes existing models for Edge-Emitting (EE) semiconductor light sources, that is to say, amplifiers and lasers, available in the literature. There exist some complete models that consider detailed material features, however, they are generally limited by very long integration times preventing the study in the parameter space and optimization. As previously commented, actual models may be grouped into mean-field models and stationary models. The first ones describe the temporal evolution of the field and carriers while they do not account for the spatial field distribution [Lug99]. On the other hand, stationary models consider the propagation of static beams along the semiconductor, while carrier and field dynamics are neglected [Ult06].

We here present and develop a full (2+1)-dimensional spatio-temporal model for the electric field and carriers, including transverse and longitudinal dimensions plus time. The starting point is the wave equation for the field inside the semiconductor and the carrier density dependence on the field [Agr84], and the main novelty is the proposed integration mechanism. Instead of simultaneously integrating the field and carriers in time in the whole active medium, we take advantage of the different characteristic temporal responses of the carriers and the field to split the calculation into a spatial integration of the field and a temporal integration of carriers. For a simple pass of the field along the

semiconductor, i.e. to model an EE amplifier, the temporal behavior of the system is just given by the carrier's relaxation time, which is justified by the difference between both temporal responses. For the case of lasers, we assume that the cavity round trip time is short (on the order of ps) as compared to the carrier's relaxation time (on the order of ns). This means that the time evolution of the field in one roundtrip may be calculated by its propagation along the cavity, assuming constant carriers. Analogously, the temporal integration of carriers assumes a constant field distribution due to its fast move towards the stationary state.

In turn, we also propose a simplified mean-field model that will also be used with some variations in Chapters 3, 4 and 5.

2.1.1 Complete spatio-temporal model

A usual approach to model EE amplifiers and lasers is to consider rate equations for the active material layer alone by introducing the field equation and appropriate boundary conditions. Then, the system is pumped by a forward bias applied voltage across the p-n junction. The carriers (electrons and holes) are directly injected into the active layer and change the active-layer dielectric constant (both the real and imaginary parts). This affects the propagation of the optical mode, altering the carrier distribution through stimulated recombination. The electrical and the optical parts are coupled, and a self-consistent solution is required. The problem is hugely involved in its most general form, and several simplifying assumptions are usually made.

The current injection density, J, crossing the active layer, enhances the carrier density in the semiconductor. In turn, nonradiative transitions, characterized by their characteristic time and radiative stimulated emission and proportional to the existing total field intensity, reduce the carrier density. Spontaneous emission and Auger recombination are not considered in this model. Altogether with the carrier diffusion, it results in the carrier density rate equation:

$$\frac{\partial N}{\partial t} = \frac{J}{ed} - \frac{N}{\tau_{nr}} - \frac{g(N)}{\hbar\omega}\left|A\right|^2 + D\nabla^2 N \tag{2.1}$$

where e is the electron charge, d *is* the active layer thickness ω the light angular frequency, and D the diffusion coefficient $g(N) = a(N - N_0)$ is the local gain,

considered linear, where *a* is the gain parameter and N_0 is the carrier density to achieve transparency, i.e., the onset of population inversion.

After normalization of the field intensity $|A'|^2 = \frac{a\tau_{nr}}{\hbar\omega}|A|^2$ and carrier density $N' = \frac{N}{N_0}$, the rate equation becomes:

$$\frac{\partial N'}{\partial t} = \gamma\left(D'\nabla^2 N' - N' - (N'-1)|A'|^2 + p\right) \tag{2.2}$$

where $\gamma = 1/\tau_{nr}$, $D' = \tau_{nr}D$ and the pump is $p = \frac{\tau_{nr}}{edN_0}J$. The field propagation inside the active material satisfies Maxwell's wave equation [Gum05]:

$$\nabla^2\mathbf{E} - \frac{n^2}{c^2}\frac{\partial^2\mathbf{E}}{\partial t^2} = 0 \tag{2.3}$$

In general, the total field $\mathbf{E}(\vec{r},t)$ is a superposition of many longitudinal and transverse modes. Here, we only consider one longitudinal mode with frequency ω_0 propagating with small aperture angles along the *z*-axis. Given the small thickness of the active layer, the fast axis (y-axis) field distribution corresponds to the fundamental waveguide mode. Thus, the field can be written as $\mathbf{E}(x,z,t) = E(x,z,t)e^{-i\omega_0 t}$ where E is the field amplitude. Introducing the field amplitude distribution in the wave equation and neglecting the temporal term $\frac{\partial^2 E}{\partial t^2}$, much smaller than ω_0, we can write:

$$\nabla^2 E + \frac{n^2 k_0^2}{n_0^2}E + \frac{2in^2 k_0^2}{n_0^2\omega_0}\frac{\partial E}{\partial t} = 0 \tag{2.4}$$

We consider the paraxial approximation, bearing in mind that the propagated light takes small angles in amplifiers and lasers. In addition, using $E^{\pm}(x,z,t) = A^{\pm}(x,z,t)e^{\pm in_0 k_0 z}$ for the forward and backward wave, and being $A^{\pm}$ the field envelopes, the k_0 wavenumber in the vacuum and n_0 the effective refractive index for the considered mode. We obtain the following expression for the field envelope of both counter-propagating fields:

$$\frac{n^2}{c}\frac{\partial A^{\pm}}{\partial t} \pm \frac{\partial A^{\pm}}{\partial z} = \frac{i}{2n_0 k_0}\nabla_{\perp}^2 A^{\pm} + ik_0 \Delta n_T A^{\pm} \tag{2.5}$$

The complete spatial and temporal refractive index variations Δn_T are defined as deviations from the effective value of the refractive index n_0 : $n(x,z,t) = n_0 + \Delta n_T(x,z,t)$. Index modulations will be generated by the carrier distribution Δn_N and by modifications of the laser structure Δn. Only a fraction of the mode, characterized by the confinement factor Γ, lays within the active region with refractive index n_a, while the rest lies in the passive surrounding medium with index n_p . The modulations of the complex refractive index generated by carriers can be written as: $i\mathrm{k}_0 \Delta n_N(x,z,t) = i\frac{\Gamma}{2n_0}\left[-an_a RN - in_a(g(N) - a_{fc}N)\right] - \frac{(1-\Gamma)}{2n_0}n_p\alpha_p$, where the first term inside brackets is the carrier-induced index reduction associated with the anti-guiding parameter. The free-carrier absorption coefficient and α_p is the passive medium absorption coefficient, see Ref. [Agr84] for more details.

As explained, we profit from the fast field response compared to carrier response to disregard the field dynamics and always consider the field in its stationary state $\frac{\partial A}{\partial t} = 0$.

Splitting the system calculation in a spatial integration of the field along the cavity for a constant carrier distribution and a temporal integration of carriers for the stationary field. Thus, the field propagation equation for the forward and backward field envelopes reads as:

$$\pm\frac{\partial A^{\pm}}{\partial z} = \frac{i}{2n_0 k_0}\nabla_{\perp}^2 A^{\pm} + \sigma\left[N'(1-ih) - (1+\alpha)\right]A^{\pm} + ik_0 \Delta n A^{\pm} \tag{2.7}$$

where $\alpha = \left(\Gamma n_a a_{fc} N_0 + n_p \alpha_p \left(1-\Gamma\right)\right) / \left(\Gamma n_a (a - a_{fc}) N_0\right)$ is the loss coefficient, $h = \frac{aR}{a - a_{fc}}$ the linewidth enhancement factor or Henry factor, $\sigma = \frac{\Gamma n_a (a - a_{fc}) N_0}{2n_0}$

is a parameter inversely proportional to the light-matter interaction length and $N' = n_0\left(a - a_{fc}\right)N$ the normalized carrier distribution.

The typical values for AlGaAs lasers are extracted from [Agw84]:

$$\begin{array}{llll} n_a = 3.55 & a = 1.5{\cdot}10^{-16}\,cm^2 & a_{fc} = 6{\cdot}10^{-18}\,cm^2 & R = 1.5-4 \\ n_p = 3.32 & \alpha_p = 10cm^{-1} & \Gamma = 0.5 & n_0 = 3.35 \\ N_0 = 10^{18}\,cm^{-3} & D = 33cm^2s^{-1} & \tau_{nr} = 5ns & d = 0.2\mu m \end{array}$$

Finally, the model is led by the following equations where we dropped all apostrophes - ’ - for simplicity:

$$\begin{aligned} \pm\frac{\partial A^{\pm}}{\partial z} &= \frac{i}{2n_0k_0}\nabla_{\perp}^2A^{\pm} + \sigma\left[N(1-ih)-(1+\alpha)\right]A^{\pm} + ik_0\Delta nA^{\pm} \\ \frac{\partial N}{\partial t} &= \gamma\left(D\nabla^2N - N - (N-1)\left|A\right|^2 + p\right) \end{aligned} \tag{2.8}$$

According to the previous table, the coefficients of Eq. (2.8) take values: $\sigma = 0.004$, $h = 1.2$ and $\alpha = 0.1$ for the above table.

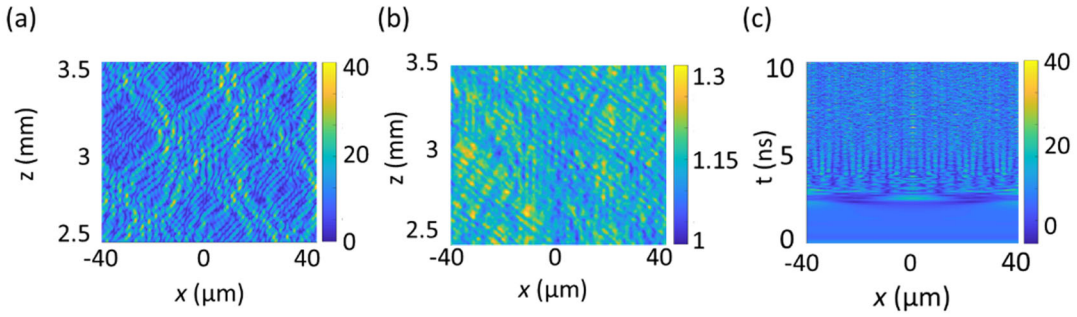

Figure 2.1. (a) Electric field along an EE amplifier exhibiting a multimode emission. (b) Corresponding carrier’s density along the EE amplifier. (c) Temporal evolution of the electric field at the end of the EE amplifier ($z = 3.5$mm). Numerical simulations are performed with the model presented in Eq. (2.8) for the forward field.

In the simplest case, may we consider just one field, namely A^+, which corresponds to a single pass EE amplifier. Therefore, to simulate the spatio-temporal behavior of an EE amplified we integrate Eq. (2.8) setting $A^- = 0$. The multimode emission of the amplified is evident from Fig. 2.1 (a), showing a field distribution along the amplified at the final propagated length, 3.5 mm, as well as from Fig. 2.1 (b) displaying the corresponding carriers’ distribution. The temporal evolution shows the instabilization of the homogeneous field and the

transition to turbulence by the accumulation of ever-increasing spatial frequencies. In addition, a high inhomogeneous field and carrier distribution along the active media with many field filamentations is present at the final integration time.

The total field intensity $|A|^2 = |A^+|^2 + |A^-|^2$ is considered for laser integration, where the interference between the forward and backward fields is disregarded. It is justified due to the different amplitude values of forwarding and backward fields along the laser, creating low contrast fringes, as shown in Figs. 2.2 (a) and (b). In addition, the carrier diffusion is large enough to blur the fine interference structures even though both fields are intertwined through the field-material interaction. The integration of the full equations of the laser also exhibits clear spatial inhomogeneities within the cavity, see Fig. 2.2 (c) and temporal instability of the output radiation, see Fig. 2.2 (d).

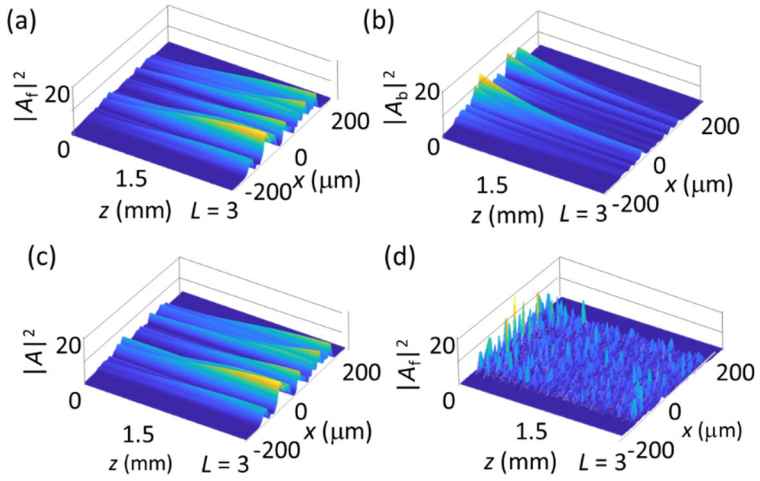

Figure 2.2. Intensity of the fields within the laser for: (a) forward field intensity, (b) backward field intensity, (c) total field, and (d) temporal evolution of the output intensity. Integration parameters: p_0 = 2.0, *width* = 400 μm, L = 1500 μm, α = 0.1 μm^{-1}, h = 2.0, s = 0.04 μm^{-1}, $k_0 = 2\pi$ μm^{-1}, D = 0.03 cm^2/s , n = 3, r_L =0.04 and r_0 = 0.99.

The boundary conditions along the propagation direction are straightforwardly determined by the Fabry-Perot cavity mirrors located at z = 0 and z = L as: $A^-(z=0) = r_0 A^+(z=0)$ and $A^+(z=L) = r_L A^-(z=L)$, where L is the length of the laser and $r_{0/L}$ are the corresponding reflection of front/back mirrors at z = 0/L, respectively. Boundary conditions in the transverse direction are sometimes

considered to be periodic, although we generally apply an hypergaussian filter to obtain a finite window.

As above mentioned, the roundtrip time of the cavity is assumed to be small as compared to the carrier's relaxation time. The temporal evolution of the field in one roundtrip is calculated by its propagation along the cavity, assuming constant carriers. Thus, each iteration in the temporal integration is divided into two main parts, the propagation of the forward and backward field along the laser cavity and the temporal integration of carrier density in time.

The first integration step considers constant carrier distribution and integrates the forward field along the cavity in a split-step form with two operators. The first one corresponding to the diffraction term is precisely integrated with Fourier space. The second operator corresponding to the rest of the equation is local and precisely integrated into the direct space. Finally, the front mirror boundary conditions give values of the backward field at this mirror. Next, the backward field is incorporated in the same form up to the back mirror. Again, the boundary conditions give the forward field at this mirror. In the final integration step, the carriers' distribution is again split into two parts. The first operator of the split-step method is the diffusive term integrated in the Fourier space. The rest of the equation is integrated in direct space, considering a constant total field intensity.

2.1.2 Simplified adiabatic model

In turn, the previous full model may be simplified in a mean-field model. Such a simplified model can be semi-analytically solved inside the laser cavity and has been used to characterize the laser threshold and LI-curve when the cavity or other parameters such as the reflectivity of the mirrors are varied. The model may be used to characterize the field along the cavity in an EEL when no transverse distributions of field and carriers are considered as well as no modulations of index and pump: $\nabla^2 N = 0$; $\dfrac{\partial^2 A}{\partial x^2} = 0$; $\Delta n = 0$ and $\Delta p = 0$.

With these simplifications, we can analytically find the adiabatic state of carriers: $N = \dfrac{P+I}{1+I}$ as a function of the field intensity $I = |A|^2$. The growth of the forward and the backward field intensities along propagation is defined by $\partial_z I = \dfrac{1+I}{2s[(p_0 - 1 - \alpha)I - \alpha I^2]}$ with the integral expression:

$$I(z) = (P-1)ln(\alpha I - P + \alpha + 1) - \alpha ln(I) + 2s\alpha(1+\alpha-P) \quad (2.9)$$

We integrate the fields along z with the corresponding boundary conditions of Fig. 2.3 (a) in an iterative process up to find the intensity profiles for the forward and backward fields.

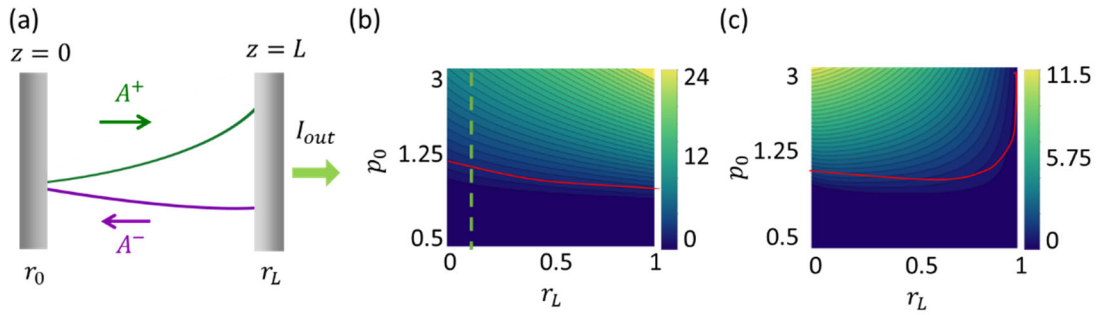

Figure 2.3. (a) Scheme of the cavity, boundary conditions and the forward and backward field envelope distributions within the unmodulated EEL. (b)/(c) Map of the intensity within the laser at z=L/output intensity; as a function of the power, p_0, and the end mirror reflectivity r_L. The red line indicates the laser threshold. The vertical green dashed line corresponds to the realistic case r_L = 0.04. The integration parameters are: α = 0.1 μm^{-1}, h = 2.0, s = 0.01 μm^{-1}, q_x = 0.5064 μm^{-1}, k_0 = 6.2832, D = 0.03 cm^2/s, L = 320 μm.

The intensity inside the laser is depicted in Fig. 2.3 (b), predicting that for high reflectivities the threshold decreases, and higher powers are obtained inside the laser, as is expected. On the other hand, in Fig. 2.3 (c), we could observe that the output intensity decrease with the reflection, as is predicted. These results confirm that the working regime for EEL is of low reflection, around 1-10%.

2.2 Intracavity spatial filtering

As introduced in Chapter 1, spatial filtering is a process to improve the laser beam quality by removing undesirable modes. In high power EELs, the nonlinearities in the active material can lead to the appearance of ripples or noise added to the smooth profile of the beam. Moreover, the beam passes through different optical elements, and its wavefront is distorted due to different optical imperfections as inhomogeneities in the refractive index of the medium, dust and diffraction effects. These accumulated field inhomogeneities correspond to high spatial frequency content in the far-field, see Fig. 2.4 (a).

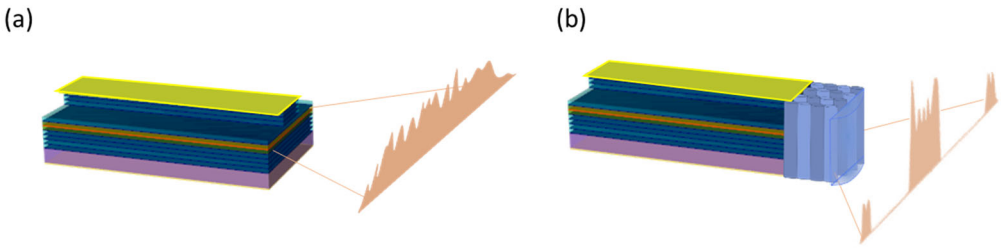

Figure 2.4. Intracavity filtering by a chirped PhC. (a) Scheme of an EEL and the multimode emission in the transverse direction (slow axis) (b) Compact intracavity filtering scheme with a chirped PhC located at the front facet of the EEL cavity intended to improve the performance, the transverse beam quality M_{x^2} factor and the brightness of the emission.

The simplest way to smooth the beam profile is the application of a high-frequency filter. The filtering is easily achieved by inserting a pinhole (or a slit in the 1D case) in the Fourier plane located at the focal plane of a converging lens which acts by laterally blocking the beam, cutting off the highest frequencies and leaving the central part of the spectrum (low frequencies).

Such spatial-filtering technique could be implemented on the emitted radiation in a single transmission scheme, however, the resulting power reduction for such a scheme does not bring any enhancement in brightness. While this simple filtering scheme suppresses high-order transverse modes enhancing the beam quality, it entails a profound reduction of the output power. Finally, the filtered frequency interval depends on the pinhole radius or slit aperture.

The same filtering technique can be applied inside the laser cavity to remove the unsuitable high frequency modes and force the amplification of low transverse modes. The profile of the emitted beam is smoothed while the output power is not drastically reduced, allowing the enhancement of the emitted beam brightness.

Moreover, the conventional filtering technique is neither convenient for intracavity filtering in micro-lasers such as microchips nor in EELs that usually have cavity lengths below the order of millimeters. An external coupled filtering cavity is neither a possibility since the bulky size of the lenses and the filter length, may strongly reduce the device compactness. Thus, new compact filtering techniques should be applied. This is the case of PhCs that act in the frequency domain without the necessary achievement of the Fourier space. PhCs represent a promising solution due to their compact nature and their well-established filtering effect that has been theoretically studied and experimentally demonstrated [Mai10, Mai15]. In this chapter, the PhCs and in particular chirped

PhCs, are considered to be used as compact spatial filters inside the cavity of EELs to improve the beam quality and maximize the brightness, see Fig. 2.4 (b).

To design the proposed intracavity filtering scheme of high spatial frequencies, we first start by a study of the conventional spatial filtering using an intracavity slit positioned in the Fourier domain with the developed model. Later, the results are experimentally validated. Once we determine the optimal slit width that maximizes brightness, we numerically prove the performance of a chirped PhC emulating the optimal slit. Then, we apply the numerical predictions to a real device and experimentally corroborate our results. Finally, we propose and prove some optimized filtering schemes.

2.2.1 Numerical filtering design

In the model, the slit is added as a transverse wavenumber cutoff filter in the Fourier space, positioned close to the front mirror. Since the aim of this filtering technique is to increase the brightness when filtering out the most divergent modes, we define the relative brightness as B/B_o, the ratio between the brightness of the emitted beam with spatial filtering (either with a slit or with a PhC) and brightness without any filtering (B_o).

We assume an actual EEL with the same parameters that will later be used experimentally. The cutoff wavenumber that simulates the slit corresponds to a divergence from 70–10 mrad. For small slit widths, the higher-order transverse modes are suppressed, in the limit, only the lowest-order transverse modes are allowed to laser. However, when the aperture is too narrow, brightness also decreases. As expected, the slit simultaneously reduces the power and the transverse beam quality factor, M_x^2 factor, which allows for enhancing the beam brightness. Figure 2.5 (a) shows the relative brightness scanning the width of the intracavity slit exhibiting a maximum enhancement for around 25 mrad aperture and pump three times above the threshold.

These numerical results may be compared to experimental measurements in Fig. 2.5 (b). The details of the experimental external cavity configuration are described in detail in section 2.2.2. We observe the same trend, compared to the predictions in Fig. 2.5 (a), a clear 3-times brightness enhancement is found for similar apertures and normalized pump current. Although the differences may be attributed to thermal guiding, losses, and other complex features not included in the model, the trend is similar for experimental and simulation results.

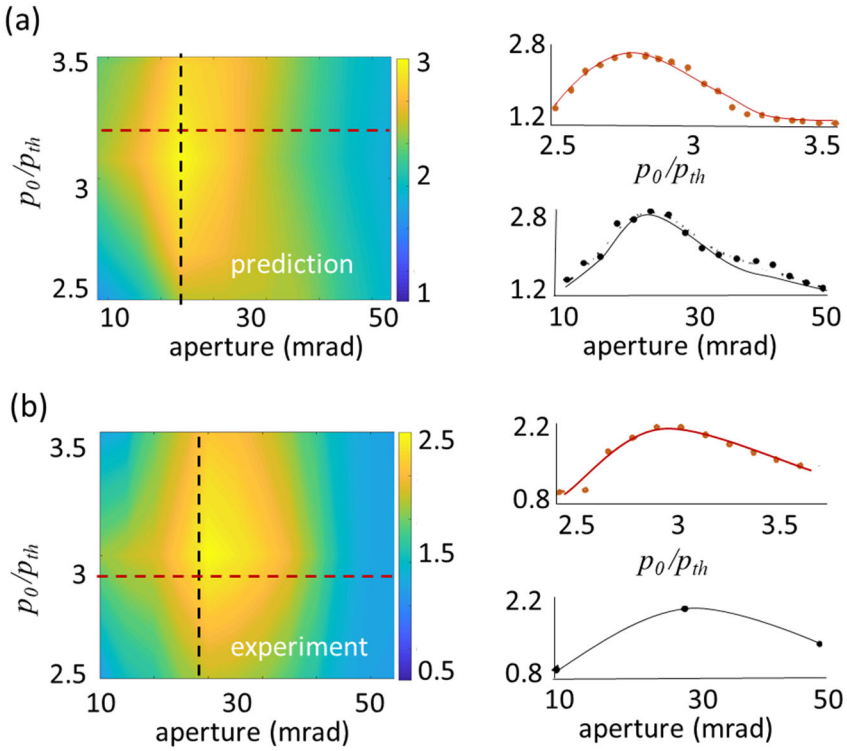

Figure 2.5. Relative brightness maps as a function of the slit aperture and normalized pump current. The pump current is normalized to the threshold current, p_0/p_{th}. Comparison of the (a) numerical and (b) experimental results of relative brightness for a short EE laser with a length of 1.5 mm. In red, cross-sections close to $p_0/p_{th} = 3$ for different apertures. In black cross-sections close to aperture = 25 mrad for different normalized currents. The integration parameters are the same as in Fig. 2.2.

In addition, we also explore the role of different parameters on the filtering performance, in particular, the effect of the reflectivity of the front mirror, while the rear mirror reflectivity is kept constant to unity. We consider three different reflectivities of the front mirror (4%, 6%, and 8%), limiting the reflectivity to 8% to avoid the possibility of causing catastrophic optical mirror damage at the front and rear facets of the laser.

We now proceed to the design of the two-dimensional (2D) chirped PhC. We assume a 2D structure as the one used in Ref. [Gaw19], where the effect was only experimentally demonstrated. It consists of an index modulation crystal fabricated via a femtosecond laser writing technique in a bulk of the N-BK7 glass substrate, characterized by the transverse and longitudinal lattice constants d_x and d_z, the latest changing linearly along the structure [Gai19].

The PhC is characterized by a geometry factor $Q = \frac{2nd_x^2}{\lambda d_z}$, chirped along the z-direction in the range of $1.10 < Q < 1.60$, and the number of periods N_P in the ranger of $20 < N_P < 120$. The transmission function of the crystals for different structures is calculated for different geometrical parameters, starting from technically available fabrication values leading to the total extinction of the higher-order spatial modes while the central modes experience almost no losses.

We initially assess the effect of such a crystal by applying the singe-pass transmission of the crystal to a broad Gaussian pulse. The effects of increasing the longitudinal chirping range dQ can be observed in Figs. 2.6 (a) and (b). Another possibility to increase the filtering efficiency is by increasing the number of periods of the structure. As the number of periods increases, the filtering performance increases and is seen in the transmitted profiles (blue), see Figs. 2.6 (c) and (d).

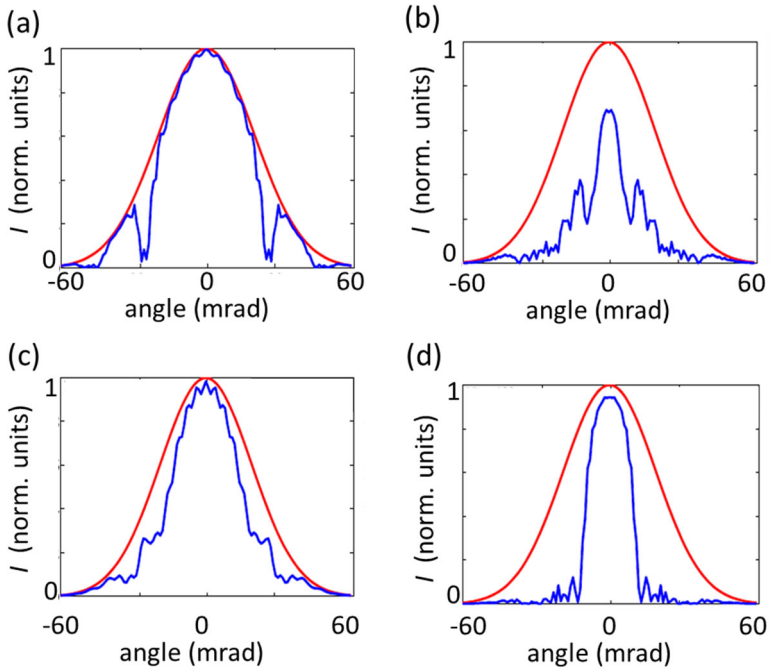

Figure 2.6. Comparison of the incident Gaussian profile and the single-pass transmitted beam trough a chirped PhC. Dependence on the chirp parameter dQ for a fixed number of layers $Np = 60$ for the different chirp of the structure, central $Q = 1.35$ and: (a) $dQ = 0.05$. (b) $dQ = 0.35$. Dependence on the number of layers Np for a fixed interval $Q = 1.35$ and chirp parameter $dQ = 0.25$ for: (c) $Np = 20$ and (d) $Np = 120$.

The filtering dips in the angular transmission get deeper with increasing the number of periods. To summarize, we searched for a numerically optimized

structure which filtering function emulated the optimized slit. The PhC was optimized by adjusting the geometry factor, Q, the chirp dQ, and the number of longitudinal periods, Np. We note that the filtering performance of the PhC is enhanced when placed inside the cavity. The PhC filtering improves the beam quality by reducing the amplitude of the high-order mode at each roundtrip while allowing the amplification of low-order modes and the enhancement of brightness.

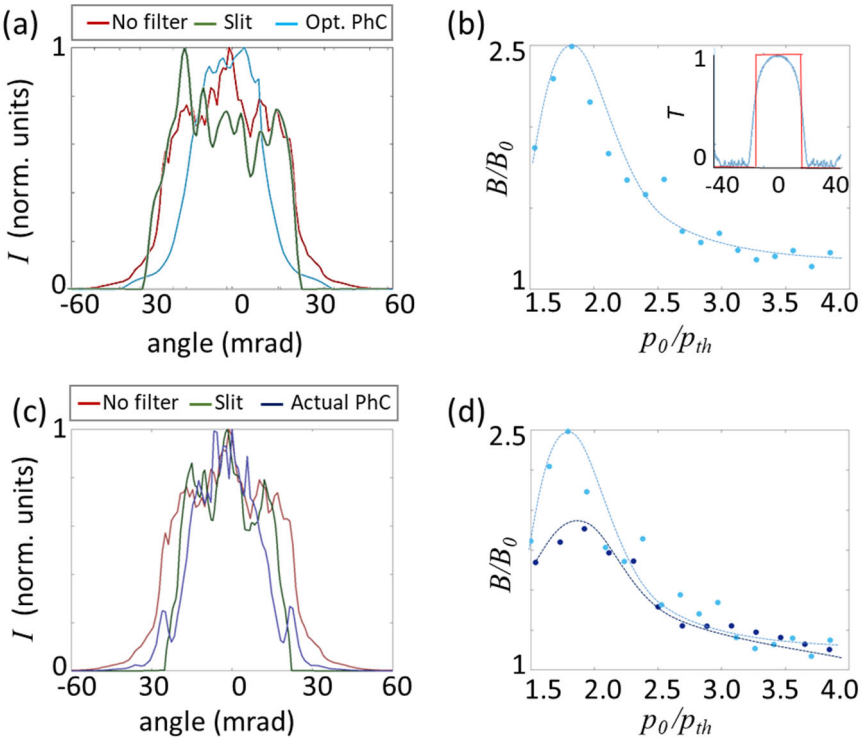

Figure 2.7. (a) Intracavity filtering performance of a chirped PhCs as compared to a slit considering an optimized PhC with central $Q = 1.14$, $dQ = 0.25$, and $Np = 73$, showing the emitted beam with noo filter (in red), the output beam with a slit (green) and the PhC filtered beam (blue). (b) Relative brightness for the optimized PhC (light blue curve) as a function of the pump normalized to the pump threshold. (c) Intracavity filtering performance of a chirped PhCs as compared to a slit considering a actual PhC with central $Q = 1.35$, $dQ = 0.25$, and $Np = 60$. (d) Comparison of the relative brightness corresponding to the optimized (light blue curve) and actual PhC (dark blue curve) as a function of the normalized pump current. The lines are a guide for the eye. The other laser integration parameters are the same as in Fig. 2.2.

We scan the PhC parameters to optimize the transmission function attaining the maximum relative brightness for Q centered at $Q = 1.14$, d$Q = 0.25$, and $Np = 73$. In Fig. 2.7 (a) we observe that a more Gaussian-like and narrow far-field is achieved when using PhC as a filter as compared to an equivalent slit, see the

comparison of the transfer function of the PhC compared to the one of a slit.To characterize of filtering performance of the PhC we scan the relative brightness as a function of the pump currents and predict a significant enhancement of a factor of 2 at twice the threshold current, see Fig. 2.7 (b).

No further enhancement is seen at higher pump currents due to thermal effects inside the cavity, restricting higher-order modes filtering, see Ref. [Gaw20]. We repeat the same predictions using the transmission function of an actual chirped PhC, fabricated with the parameters central Q = 1.35, dQ = 0.25, and Np = 60, see Fig. 2.7 (c). The maximum enhancement of the relative brightness in this case is found to be on the order of 1.7, close to the previous pump current, see Fig. 2.7 (d).

2.2.2 Experimental demonstration

Finally, the spatial-filtering performance of chirped PhCs in EELs was experimentally explored using an extended cavity scheme, see Fig. 2.8 (a) [Gaw20].

The actual experimental setup consists of an anti-reflection (AR) coated laser, microcylindrical Fast Axis Collimator (FAC), two pairs of cylindrical lenses to create conjugate planes, and a feedback mirror (front mirror of the cavity). The front facet of the laser is AR coated (R < 0.01%), while the back facet has a reflectivity of 95%. The active length of the laser diode is 1.5 mm, while the transverse width is 400 μm. The operating wavelength was 970 nm at a driving current of 3 A and the total emitted power of 1.24 W in continuous wave (CW) mode.

The high divergence emission along the fast axis is collimated using a high Numerical Aperture (NA) of 0.8 microcylindrical FAC microlens, with a focal length of 590 μm. A double 4-f plano-convex cylindrical lens system, acting along the slow axis, creates two conjugate planes of the emitter facet plane, see Fig. 2.8 (a). The lenses L_1-L_2 and L_3-L_4 are placed in a confocal arrangement forming the self-imaging cavity, which returns the same field to the same position after one round trip. The focal length of lenses L_1-L_4 is f = 50 mm, and all the lenses used are AR coated for near-infrared wavelength.

The improvement of the output laser beam is studied by measuring the power, the spectrum, the M^2 factor, and the laser beam profiles of the near-field, at plane B and far-field at the Fourier plane, plane C, see Fig. 2.8 (a). The laser cavity

mirror is located at the second conjugate plane, at the end of the extended 4-f cavity. The reflectivity of the used mirrors varies between 4% and 8% in one side and having an anti-reflection (AR) coating on the other side.

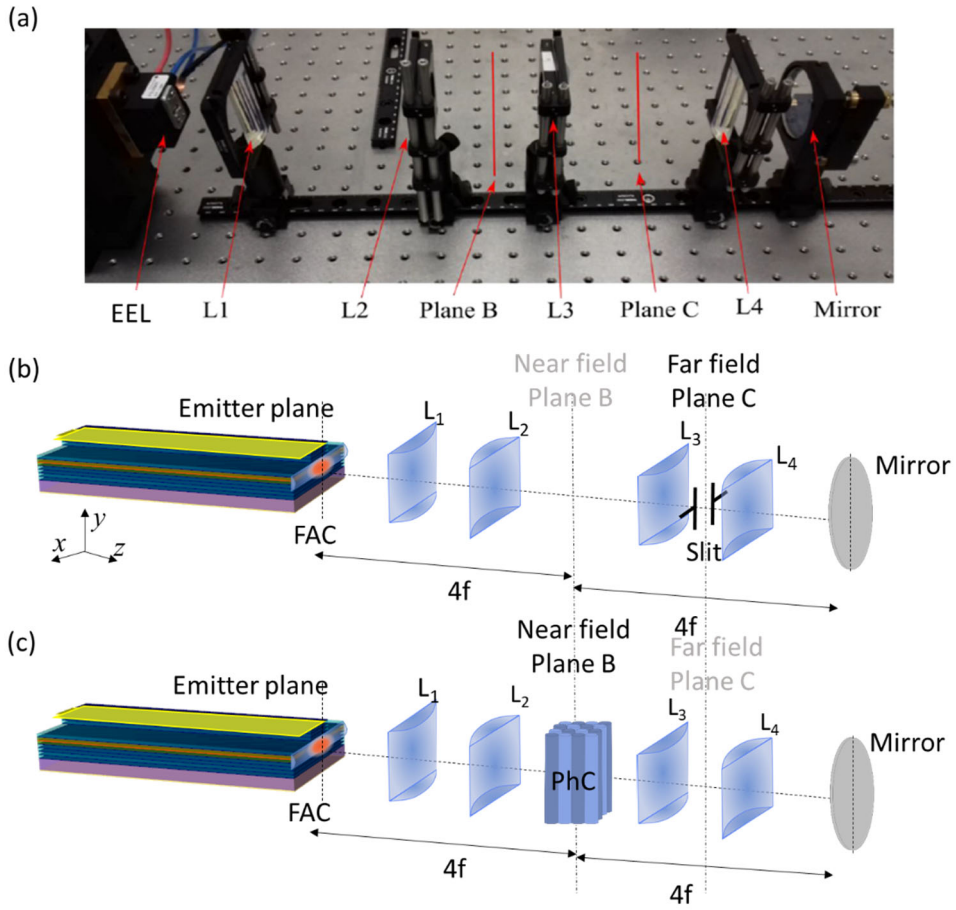

Figure 2.8. (a) Photograph of the experimental setup showing the EEL, 4 lenses of the double 4f lens system: L1, L2, L3, L4, the Fourier plane C and the conjugated plane B, and external cavity Mirror. (b) Scheme of the spatial filtering using intracavity variable slit placed at the far-field, plane C. (c) Scheme of the spatial filtering in extended cavity configuration using a PhC as a spatial filter at the near field, plane B.

This setup allows for the characterization of spatial filtering effect using either the slit in the far-field planes, Fig. 2.8 (b) or the chirped PhC, in plane B as in Figs. 2.8 (c), in the same setup. The beam profiles at the output of the laser (near field) or at the focal plane of an external lens (far-field) are recorded by imaging the profiles into a CCD camera with proper magnification. The used PhC had a chirped structure with central $Q = 1.35$, $dQ = 0.25$, and $Np = 60$.

We simulated the intracavity PhC spatial filtering considering a laser with the same experimental conditions and using the actual transmission function of the crystal in the numerical simulations. The beam profile predicted by the model with and without the intracavity filtering are depicted in Fig. 2.9 (a). A significative filtering was obtained while the profile of the emitted beam becomes smoother.

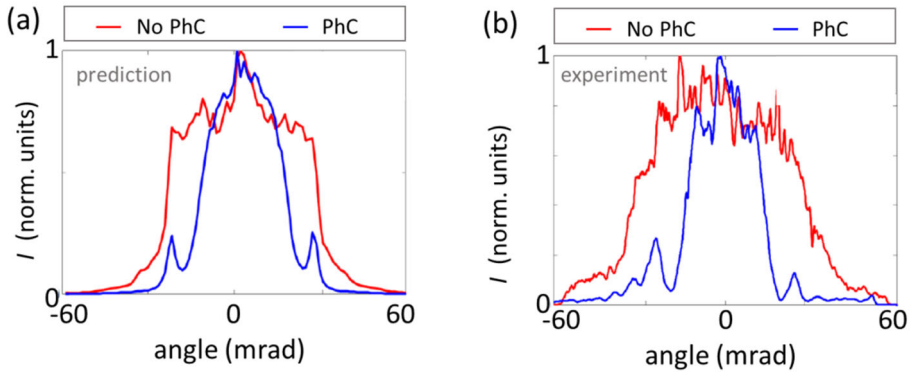

Figure 2.9. (a) Prediction of a monolithic integrated PhC filtering scheme in a compact cavity configuration. Effect of the chirped PhC spatial filtering on the far-field profiles with (blue) and without (red) PhC. The integration parameters are the same as in Figure 2.7. (b) Experimental results for an external cavity filtering at the Fourier plane.

The experimental results show a good agreement for both far-field distributions, with and without PhC, and with an analogous filtering results, see Fig. 2.9 (b). The improvement in the transmittance function was demonstrated with a clear correspondence between experimental and the corresponding numerical field profiles, cutoff angles, and corresponding divergence.

Besides, the output power, M^2 factor, absolute and relative brightness were measured in the experiments and compared with the accurate numerical analysis [Gaw20].

The numerical analysis and the experiments confirm the possible integration of a chirped PhC inside the EEL cavity between the front and cavity mirrors, leading to the highly compact cavity configuration.

2.2.3 Alternative filtering schemes

The efficiency of spatial filtering using optimized PhCs can be further increased by modifying the filtering scheme. The ultimate goal is a monolithic implementation, as schematically illustrated in Fig. 2.10 (a), showing how the

PhC structure could be integrated directly between the active medium and the front facet of the laser output cavity mirror. Alternatively, we also consider other possible configurations in which the PhC could be placed either at the rear facet, Fig. 2.10 (b), at both facets (rear and front), as shown in Fig. 2.10 (c).

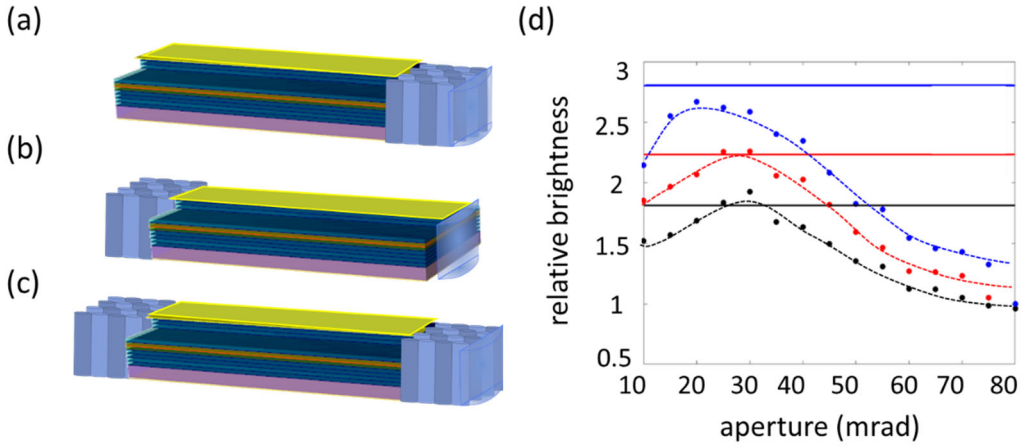

Figure 2.10. Scheme of an integrated compact cavity configuration, with the filtering element (chirped PhC which could be integrated at the mirrors, FAC lens…) at (a) front facet, (b) rear facet, and (c) both facets. (d) Optimized filtering performance as compared to the slit. The figure shows the relative brightness as a function of the slit aperture for a pump current of $p_0 = 2.5$. The horizontal lines correspond to the chirped PhC filtering results for the proposed configurations: (a) in black, (b) in red, and (c) in blue. The integration parameters are the same as in Figure 2.7.

We numerically simulate these three different geometries for the same parameters as previously considered. The results are resumed in Fig. 2.10 (d). We can observe that schemes with spatial filtering at the rear mirror always show smaller relative brightness than those with spatial filtering at the front mirror, while simultaneous filtering at both mirrors achieves the highest relative brightness. Slightly smaller values are attained for the optimized PhC located at the front and rear mirror while simultaneous PhCs at both mirrors reach the maximum relative brightness enhancement even higher than the slit case. These results indicate the way to achieve better optimization of our filtering scheme, even if new ways to implement this geometry experimentally must be conceived and analyzed in detail to check its availability. The successful implementation of the filtering PhCs in this scheme could lead to a very compact device with optimized beam quality.

2.3 Conclusions

To conclude, we demonstrate the spatial intracavity filtering by a chirped PhC, both theoretically and experimentally. Predictions are based on a complete (2+1)-dimensional space-temporal model, including transverse and longitudinal spatial degrees of freedom and temporal evolution of the electric field and carriers. We predict a brightness enhancement by a factor of 2.5, using an optimized chirped PhC placed on both the front and rear facets of the laser. The effect may be even higher than the filtering performance of a slit.

Experiments were performed in an extended cavity configuration using an intracavity 2D chirped PhC at the near-field plane and comparing it to a variable width slit in the far-field plane, determining a reduction of the beam quality parameter M^2 by a factor of 1.8, bringing along a brightness increase by a factor of 1.3. The experimental results are in good agreement with the numerical simulations, considering the transmission of the actual PhC used in experiments.

Further improvement may be achieved by exploring different spatial-filtering schemes using the PhC by placing it at both mirrors. These findings demonstrate that intracavity PhC filtering may render EELs bright light sources while keeping their compactness. Worth noting that the good agreement between numerical predictions and experiments confirms the validity of the model.

Publication I

S. Gawali, J. Medina, D. Gailevičius, V. Purlys, G. Garre-Werner, C. Cojocaru, J. Trull, M. Botey, R. Herrero, J. Montiel-Ponsoda, and K. Staliunas, "*Spatial filtering in edge-emitting lasers by intracavity chirped photonic crystals,*" Journal of the Optical Society of America B **37**(10), 2856-2864 (2020).

ATTENTION¡¡
Pages 58 to 66 of the thesis, containing the article mentioned above are available at the editor's web
https://opg.optica.org/josab/abstract.cfm?uri=josab-37-10-2856

Chapter 3

Spatio-temporal stabilization by complex modulations

Publications II, III, and IV

3.1 Spatial stabilization by complex modulations

As commented in Chapter 1, section 1.2.2, it was proved that intrinsic modulations of the pump profile allow managing the dispersion to improve the spatial structure of the emitted beam in edge-emitting (EE) amplifiers and lasers. In a linear amplification regime, such a modulation leads to the spatial filtering of the output radiations [Her12, Rad13]. Nevertheless, the situation is more involved in highly non-linear regimes due to the appearance of modulation instability (MI), which may be affected by refractive index and pump modulations [Vla06]. In a more recent study, a spatio-temporal modulation in the potential was proposed to control the modulation instability in EE amplifiers [Kum14], as well as in a broader class of spatially extended non-linear dynamical systems [Kum15]. However, MI is only partially suppressed for pump-modulated EE amplifiers and is limited to small linewidth enhancement factors (Henry factor). Thus, this solution is not completed, and it only works in particular regimes of parameters. The periodic modulation of the pump reduces or even removes the instabilities of the short-wave region although long-wave instabilities remain, preventing the complete stabilization of the EE amplifier. The total stabilization of the system can be reached reducing the width of the amplifier forbidding the existence of long waves.

This Chapter presents an efficient and compact scheme to obtain a stable and high-quality output from EE light sources by tailoring its dispersion. We propose introducing a periodic in-phase modulation of the refractive index and the pump (gain-loss) profiles, in transverse and longitudinal directions (2D space). In particular, we numerically show the stabilization performance of the proposed mechanism applied to EE amplifier sources. The results of this chapter were published in [Ahm18] and [Med18].

3.2 Modulated edge-emitting amplifiers

Pump modulations can stabilize edge-emitting amplifiers for small enough values of the linewidth enhancement factor, h, as demonstrated in [Kum15]. However, it may not be sufficient to stabilize highly non-linear regimes that appear for large values of h or high pump values. The principal reason is that pump modulations induce in turn refractive index modulations, which may

increase the resultant instabilities. These handicaps can be overcome by simultaneously modulating pump and refractive index profiles.

Specifically, we aim at stabilizing the long-wave transversal MI remaining when only pump modulations are introduced. With this purpose, we modulate the potential in two directions, the transversal and longitudinal directions, with respective modulation wavenumbers q_x and q_z. A mutual resonance between the transverse and the longitudinal harmonics is expected to strongly modify the spatial dispersion and the corresponding stability of the system.

This Chapter uses the spatio-temporal model presented in Chapter 2, section 2.1.1, adding a modulation on the refractive index, $m_2(x,z)$, and on the pump, $m_1(x,z)$. The paraxial model describing the dynamics of electric field amplitude (A) and carrier density (N) for the proposed doubly modulated EEL source may be expressed as:

$$\begin{aligned}\frac{\partial A(x,z,t)}{\partial z} &= \frac{i}{2k_0 n}\frac{\partial^2 A}{\partial x^2} + s[(1-ih)N-(1+\alpha)]A + 4im_2(x,z)k_0 A \\ \frac{\partial N(x,z,t)}{\partial t} &= \gamma(N-(N-1)\,|A|^2 + p + 4im_1(x,z) + D\nabla^2 N)\end{aligned} \tag{3.1}$$

The parameter values considered along this Chapter largely coincide with the ones presented in Chapter 2. The in-phase spatial modulations of pump and refractive index share the same spatial profile $m_{1,2}(x,z) = m_{1,2}\cos(q_x x)\cos(q_z z)$, with amplitudes m_1 for pump and m_2 for refractive index and with q_x transverse and q_z longitudinal wavenumbers. The spatial modulations are assumed in the transverse and longitudinal directions on small spatial scales, i.e., where $|q_x| >> k_0$ and $|q_z| >> \lambda$, where λ is the typical growth rate of the unstable transverse wavevectors. The modulation geometry may be characterized by the geometrical parameter $Q = 2nk_0q_z/q_x^2$ relating both wavenumbers $q_x = 2\pi/\, d_\perp$ and $q_z = 2\pi/d_\parallel$ being $d_\perp$ and $d_\parallel$ the transverse and longitudinal period of the modulation, respectively. Close to the resonance condition, $Q \approx 1$, it is possible to suppress the region of unstable wavevectors that precede the chaotic dynamics and therefore stable stationary states are achieved [Sta06]. In addition, to suppress long-wave instability modulation, the modulation wavenumber q_x should be similar to the most unstable wavenumber k_x of the system.

3.2.1 Characterization of the instabilities

Firstly, we consider unmodulated EE amplifier sources showing typical spatio-temporal chaotic behavior and the corresponding broad spatial spectrum, see Fig. 3.1. The width of the field spectrum indicates the range of the unstable wavenumber, contributing to chaotic dynamics, which is around 2 μm^{-1}. In order to perform an experimentally intended simulation, we assume realistic parameters compared with the model [Agr84] previously presented in Chapter 2, section 2.2.1. The pump is taken above the threshold, and carrier relaxation rate, γ, is normalized to the nonradiative characteristic relaxation time ($\tau_r = 2\ ns$), with a typical normalized value of 0.01.

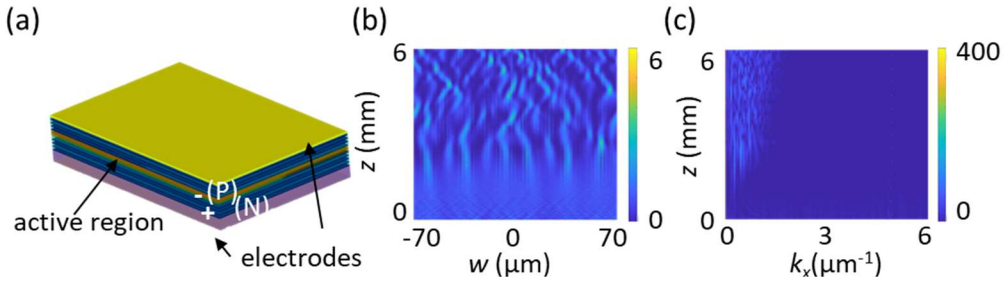

Figure 3.1. (a) Scheme of the unmodulated EE amplifier. Direct numerical integration results: when no modulation is applied $m_1 = m_2 = 0$. (b) Field distribution, and (c) spatial spectrum, k_x, inside the semiconductor after a long integration time. The simulation parameters are w = 140 μm, L = 6.4 mm, n = 3.3, D = 0.15 cm²/s, h = 2, α = 0.1 μm^{-1}, s = 0.03 μm^{-1}, γ = 0.01, p = 1.21 A.

The model of Eq. (3.1) allows analyzing the spatio-temporal dynamics of the system schematically shown in Fig. 3.1 (a). The integration of the system with a homogeneous input beam with small amplitude white noise typically shows a nonstationary and highly inhomogeneous field distribution in transverse and longitudinal directions arising from spatio-temporal instabilities. Increasing the pump parameter, the system usually reaches turbulent behaviors for a large range of parameters through the well-known MI, i.e. the instabilization of the homogeneous solution for an interval of transverse wavenumbers, see Figs. 3.1 (b) and (c).

However, other particular solutions can be observed, for instance nonhomogeneous stable stationary solutions that can even be spatially non-periodic, i.e. spatially chaotic, for long enough amplifiers, see Fig. 3.2.

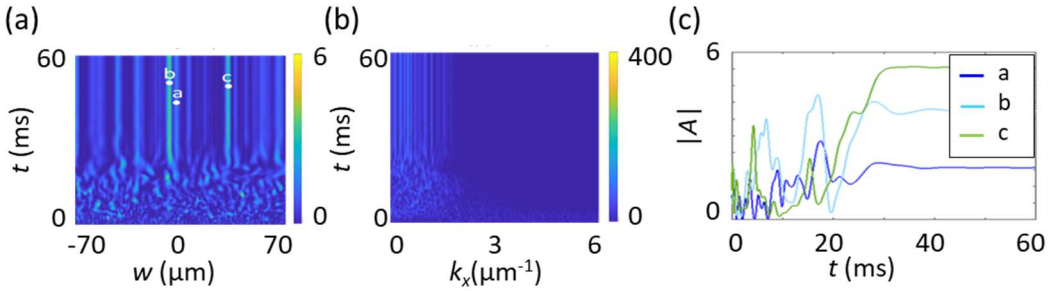

Figure 3.2. Direct numerical integration results: for the unmodulated case $m_1 = m_2 = 0$; Temporal evolution of (a) field and (b) spectrum at the end of the semiconductor. (c) Field envelope temporal evolution at points a, b, c indicated in (a). The simulation parameters are the same as Fig. 3.1.

Similar solutions with different stable profiles have been obtained by changing the small amplitude noise added to the input beam. These particular solutions become stable in temporal propagation, indicating a large enough basin of attraction in the phase space. We plotted the evolution of the field at three spatial points marked as (I, II, III), Fig. 3.2 (c). The temporal evolution shows stability in all points for times over 40 *ms*.

Note that only the incident field at $z = 0$ is fixed while the EE amplifier intrinsically involves the spatial propagation of the field and carriers in the longitudinal direction as well as their temporal evolution. Thus, we can differentiate spatial and temporal instabilities for the stationary states of the amplified beam. In this particular case, the homogeneous incident field becomes unstable along propagation through a MI, reaching chaotic distributions in the transverse space for large enough z values while they remain stable in time.

Another parameter that has a direct impact on temporal stability is the pump. As expected, the temporal instability increases with the pump value. This spatially non-periodic stable solution becomes unstable for a threshold pump value, temporal instabilities arise, and smooth periodic temporal oscillations appear, see the dark blue line in Fig. 3.3 (a). As can be observed in Fig. 3.3 (b), oscillations appear all over the stationary pattern. Finally, for larger values of the pump, the system turns into turbulent temporal behavior, see the black line in Fig. 3.3 (a).

The more unstable the temporal behavior, the more complex the stabilization becomes, and higher values of modulation amplitudes may be required. In this direction, Chapter 4 proposes a novel stabilization method for highly unstable systems beyond the achievements of the presented in-phase modulations in this Chapter.

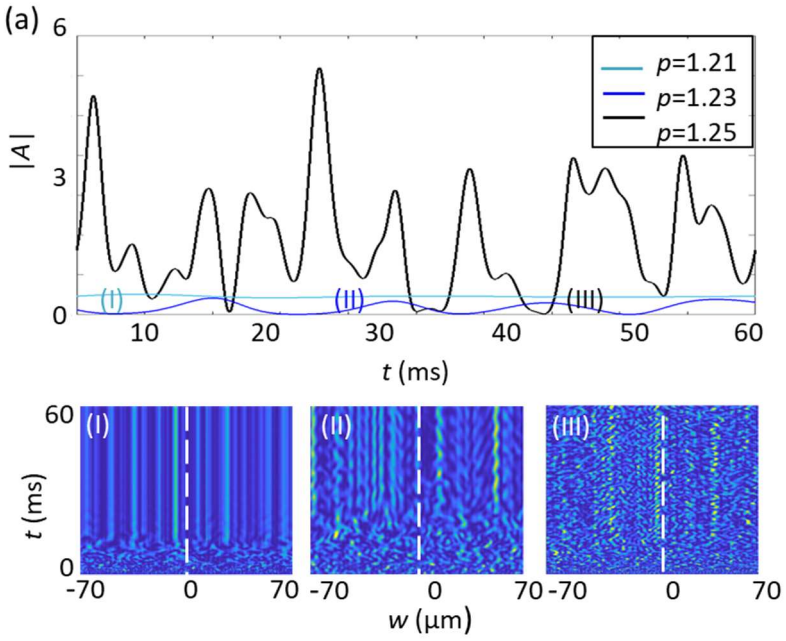

Figure 3.3. (a) Temporal instability of a spatially non-periodic solution for the unmodulated amplifier case. Temporal evolution for three different pumps 1.21, in light blue (stable), 1.23, dark blue (periodic), and 1.25 in black (chaotic). The simulation parameters are the same as Fig. 3.1.

3.2.2 Pump modulations

In this section, we shortly present some results of partial stabilization of the EE amplifier obtained with only pump modulations, schematically represented in Fig. 3.4 (a).

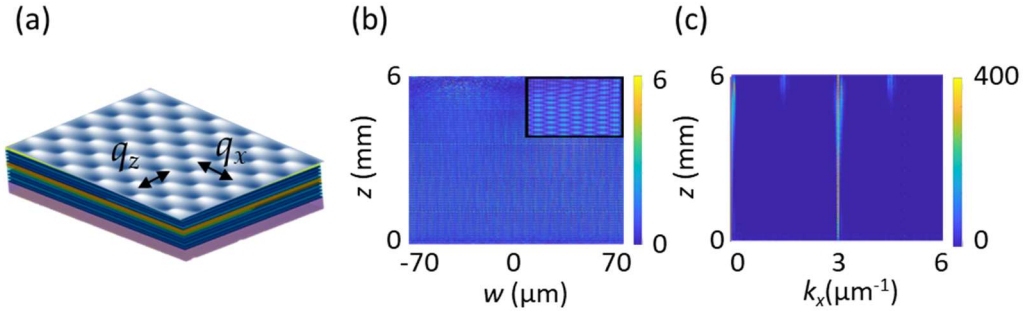

Figure 3.4. (a) Scheme of the amplifier and direct numerical integration results for the pump modulated case with parameters m_1= 0.35; m_2 = 0, q_x = 2.85 μm^{-1} and q_z = 0.196 μm^{-1}. (b) Field distribution and a zoomed-in view of it depicted in the inset, and (c) transverse spatial spectrum inside the semiconductor after a long integration time. The rest of the simulation parameters are the same as Fig. 3.1.

Publication II

W. W. Ahmed, S. Kumar, J. Medina, M. Botey, R. Herrero, and K. Staliunas, "*Stabilization of broad-area semiconductor laser sources by simultaneous index and pump modulations,*" Optics Letters **43**(11), 2511-2514 (2018).

Publication III

[Ahm18-2] W. W. Ahmed, S. Kumar, J. Medina, M. Botey, R. Herrero, and K. Staliunas, *"Stabilization of Broad Area Semiconductor Amplifiers and Lasers by Double Modulation of Pump and Refractive Index,"* 2018 20th International Conference on Transparent Optical Networks (ICTON). IEEE, 2018.

Publication IV

[Med18] J. Medina, W. W. Ahmed, S. Kumar, M. Botey, R. Herrero, and K. Staliunas, *"Stabilization of Broad Area Semiconductor Laser Sources,"* 2018 20th International Conference on Transparent Optical Networks (ICTON). IEEE, 2018.

ATTENTION¡¡
Pages 92 to 94 of the thesis, containing the article mentioned above are available at the editor's web
https://ieeexplore.ieee.org/abstract/document/8473604

Chapter 4

Spatio-temporal stabilization of PT-axisymmetric edge-emitting lasers

This chapter introduces various schemes of refractive index and effective gain-loss modulations based on PT-symmetry to stabilize and improve the spatial quality and temporal stability of Edge-emitting (EE) light sources, EE amplifiers, and EE Lasers (EELs). The main goal is to manage the dynamics of field and carriers to enhance the performance of EE light sources by using non-Hermitian modulations with local mirror-symmetric (PT-axisymmetric) configurations. The results presented here were published in Ref. [Med20].

4.1 Light propagation in PT-symmetric potentials

As presented in former chapters, a major drawback of semiconductor light sources and particularly EE light sources is the relatively low spatial and temporal quality of the emitted beam. Modulation Instability (MI) is the fundamental phenomenon that induces the mentioned spatio-temporal instabilities, which leads to complex dynamics and filamentation, i.e., a disruption of the smoothly distributed field into multiple filaments. Such complex dynamics limit the applications of EE light sources [Hes95, Bes66].

As presented in Chapter 1, section 1.2.2, the introduction of 2D spatial modulations in the refractive index [Her12, Rad13] or the pump profile [Kum14] can help to stabilize EE amplifiers and vertical emitting semiconductor laser sources [Ahm15]; also, a spatio-temporal modulation can control modulation instability [Kum15]. Besides, as demonstrated in Chapter 3 for EE amplifiers, in-phase 2D refractive index and pump spatial modulations lead to a substantial improvement of the spatial quality and temporal stability of the emitted beam [Kum14, Ahm18].

Finally, as described in Chapter 1, section 1.3.3 non-Hermitian Photonics and particularly PT-symmetric potentials are an interesting new platform for the control of light. Indeed, the asymmetric coupling may lead to a field directionality and promote light concentration and stabilization in vertical emitting semiconductor laser sources [Ahm16].

The simplest PT-symmetric periodic potential may be expressed as:

$$V(\vec{r}) = m_{Re}cos(\vec{q}\vec{r}) + im_{Im}sin(\vec{q}\vec{r}) = m_{+}e^{i\vec{q}\vec{r}} + m_{-}e^{-i\vec{q}\vec{r}} \quad (4.1)$$

where $m_+ = m_{Re} + m_{Im}, m_- = m_{Re} - m_{Im}$, and $q = 2\pi/\Lambda$ is the modulus of the modulation wavenumber $\vec{q}$, being Λ the spatial period. The induced asymmetry can be shown by integration of the field paraxial propagation in a 2D space, introducing this modulated potential as the complex refractive.

We here consider a simple potential in the transverse direction, $V(x)$:

$$\frac{\partial A}{\partial z} = \frac{i}{2n_0 k_0}\frac{\partial^2 A}{\partial x^2} + ik_0 V(x)A \tag{4.2}$$

where the product $V(x)A$ expresses the field-medium interaction. Such spatial modulations of the medium introduce couplings between plane wave components of the beam, coupling the modes $\vec{k}$, $\vec{k}+\vec{q}$, and $\vec{k}-\vec{q}$. Note that this is straightforward from the expression of the potential in an exponential form, see Eq. (4.1). Thus, the amplitudes of the exponents, m_+ and m_- , may induce asymmetric mode coupling through the field-medium interaction. The maximal asymmetry arises when ones of such amplitudes cancel, that is to say, when the real and imaginary components of the potential are balanced. This condition corresponds to the PT-symmetry breaking point, and corresponds $|m_{Re}| = |m_{Im}|$ [Ben98].

The case $m_+ = m_-$ leads to symmetric mode coupling, see Fig. 4.1 (a), and has been previously studied in Chapter 3. When either of these constants vanishes, the PT-symmetric potential coupled with the central mode $\vec{k}$, only to either $\vec{k}+\vec{q}$ or $\vec{k}-\vec{q}$, see Fig. 4.1 (b). Finally, the non-Hermitian potential can induce a non-isotropic or *local* asymmetry. As was proposed in Ref. [Ahm16], instead of presenting the same asymmetric coupling homogeneously on a *global* scale as in Figs. 4.1 (b), the PT-symmetry condition can be spatially dependent, we then refer to it as a *local* PT-symmetry. In the simplest case, we consider a mirror-symmetric potential with a central symmetry axis, and with opposed directionality in the two half-spaces that is expected to create either a field localization on-axis or an outwards energy flow from it, see Fig. 4.1 (c) and (d) [Ahm18-3]. Such PT-axisymmetric potential with unidirectional mode coupling at each half space could be used, as proposed later in this chapter, to regularize the spatio-temporal dynamics of EELs by localizing the field while improving stability.

For a physical picture to understand the induced coupling asymmetry, just remember that the field is generated in positive gain areas (grey profiles in Fig. 4.1 schemes), and it tends to have large index areas (blue profiles) in propagation.

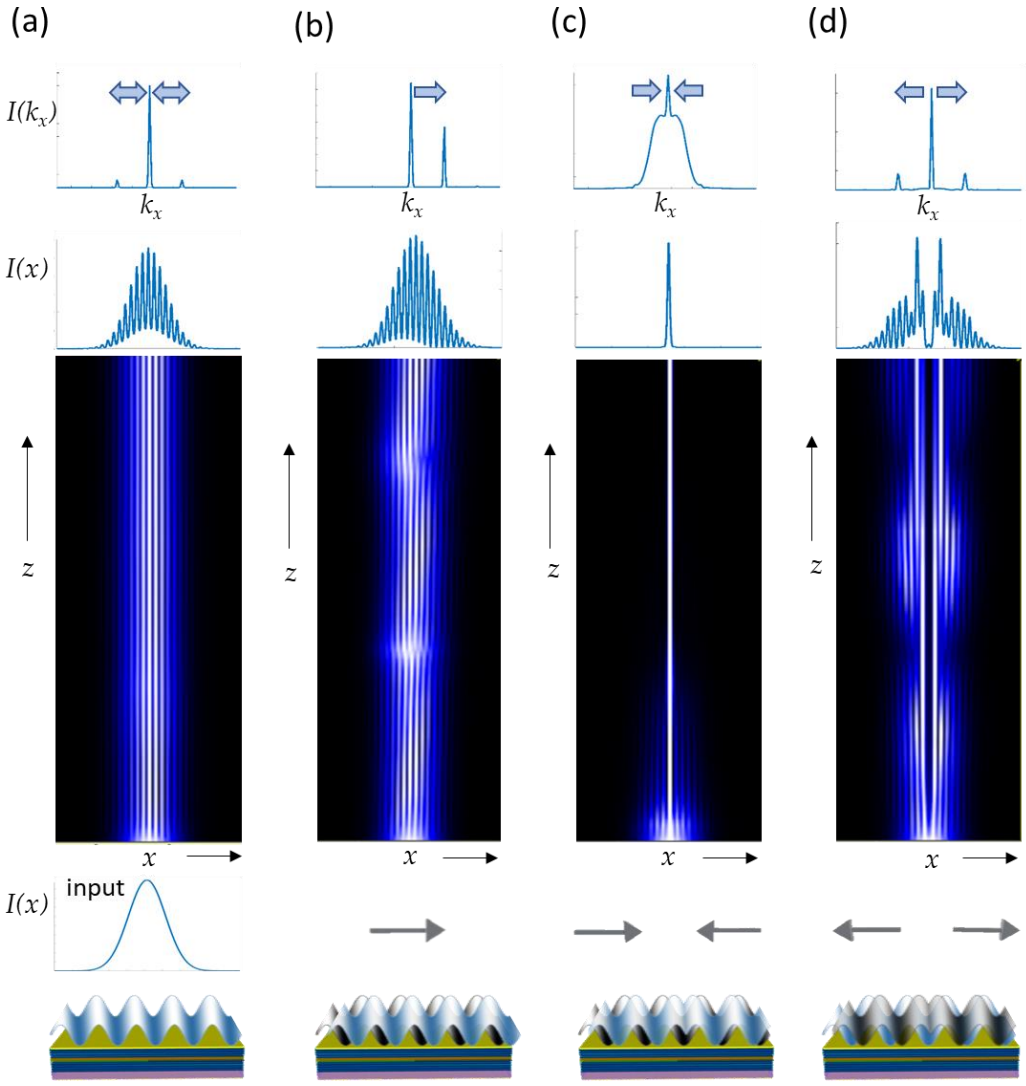

Figure 4.1. Gaussian beam propagating in a harmonic non-Hermitian media. From bottom to top: schemes of the transverse potential (blue indicates index and grey indicates gain); arrows indicating enhanced coupling direction; beam propagation by paraxial approximation Eq. (4.2), with the corresponding potential; output beam profiles in direct and in frequency space for: (a) index (or gain) modulation; (b) global PT-symmetric potential; (c) local axisymmetric potential with an inward mode coupling; (d) local axisymmetric potential with an outward mode coupling.

We preliminary analyze the effect of both global and local PT-symmetric potentials on EE amplifiers. Once the regularization scheme is proven in EE

amplifiers, we proceed to analyze the management of the emitted radiation from EELs.

4.2 Edge-emitting amplifiers with global and local PT-symmetry

The introduction of a non-Hermitian potential in an EE amplifier may be achieved by variations of the etch depth in the epitaxial layer structure (inducing index modulations), while spatially structuring the electrodes may be used to modulate the current injection density, leading to carrier density modulations.

Despite electrodes may present a stepwise profile, the induced spatial modulations of the injection current will be strongly smoothed due to the carrier diffusion. Therefore, for simplicity, we assume harmonic transverse modulations of the pump $\Delta p(x,z) = m_1 \sin(q_x x+\Phi)$ where the spatial transverse wavevector is $q_x = 2\pi / d_\perp$, being $d_\perp$ the transverse period (in the order of microns), and m_1 is the amplitude of the pump modulation.

Note that such a pump modulation may, in turn, induce refractive index modulation through the Henry factor of the semiconductor, h. This induced modulation of the refractive index is in-phase with the gain-loss modulation.

Then, in order to obtain the desired spatially shifted modulation of gain and the refractive index, we assume a sinusoidal refractive index modulation expressed as: $\Delta n(x,z) = m_2 \cos(q_x x) + m_3 \sin(q_x x)$. The first term is intended to render the refractive index in quadrature with the induced gain-loss modulation and the second term counterbalances the extra modulation induced by the Henry factor. The desired refractive index and gain-loss amplitudes, as well as the desired spatial shift or dephasing, are obtained by adjusting the set of modulation amplitudes (m_1, m_2 and m_3). The described modulations create a global PT-symmetric potential, see Fig. 4.2 (a), exhibiting the same mode coupling directionality character in the whole space. Such potential is included in the EE amplifier equations already presented in Eq. (2.7), in the following form:

$$\frac{\partial A}{\partial z} = i(2k_0 n)\frac{\partial^2 A}{\partial x^2} + s[(1-ih)N - (1+\alpha)]A + i\Delta n(x,z)k_0 A$$
$$\frac{\partial N}{\partial t} = \gamma(-N - (N-1)\,|\,A\,|^2 + p_0 + \Delta p(x,z) + D\nabla^2 N) \tag{4.3}$$

being Δn the direct refractive index modulation in the field equation also intended to compensate the index modulations indirectly induced by the pump modulation, Δp in the carrier's equation.

The propagation of an incident plane wave (with perfectly periodic boundary conditions) through the global PT-symmetric amplifier leads to the tilted field pattern reported in Fig. 4.2 (b). The corresponding spectrum clearly shows the coupling of the central wavevector of the incident field to positive transverse components of the wavevector, see Fig. 4.2 (c).

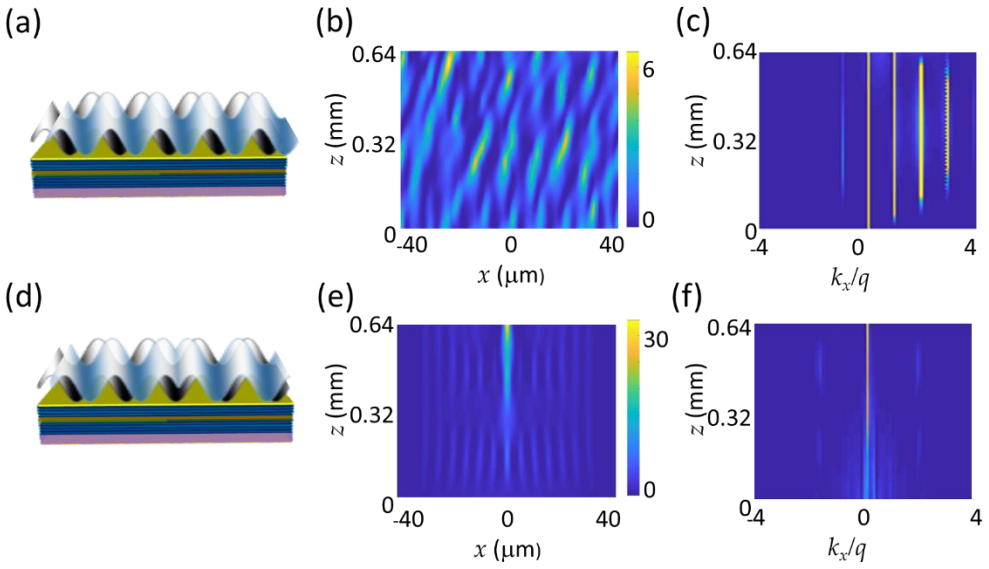

Figure 4.2. (a-c) Global PT-symmetric potential and (d-f) Local PT-symmetric (PT-axisymmetric) potential. (a)/(d) Scheme of the refractive index (blue) and pump (grey) effective modulation. (b)/(e) Intensity distribution within the amplifier for an incident plane wave propagated along z, for a sufficiently long integration time. (c)/(f) The corresponding transverse spectrum. The integration parameters are: $m_1 = 0.5$, $m_2 = 0.06$, $m_3 = -0.03$, $\Phi = 0$ and $p_0 = 1.23$.

We now consider a PT-axisymmetric potential with a central symmetry axis at $x = 0$, dividing the system into two half-spaces, both holding PT-symmetry but directed in opposite senses. We assume a symmetric harmonic transverse modulation of the pump and the refractive index, respectively, in the form:

$$\begin{aligned}\Delta p(x,z) &= m_1 \sin\left(q_x |x| + \Phi\right) \\ \Delta n(x,z) &= m_2 \cos\left(q_x |x| + \Phi\right) + m_3 \sin\left(q_x |x| + \Phi\right)\end{aligned} \tag{4.4}$$

The general phase Φ, appearing in all modulations, controls the character of the central axis. The resulting potential is schematically presented in Fig. 4.2 (d). Such potential is expected to couple light asymmetrically in the transverse direction, promoting the inward coupling, enhancing and localizing light at the symmetry axis. Figure 4.2 (e) shows the resulting field distribution along the propagated direction for a large enough integration time and using an hypergaussian pump profile as boundary conditions in the transverse direction. We observe that the corresponding spectrum does not broaden as in the previous case but remains almost constant, see Fig. 4.2 (f).

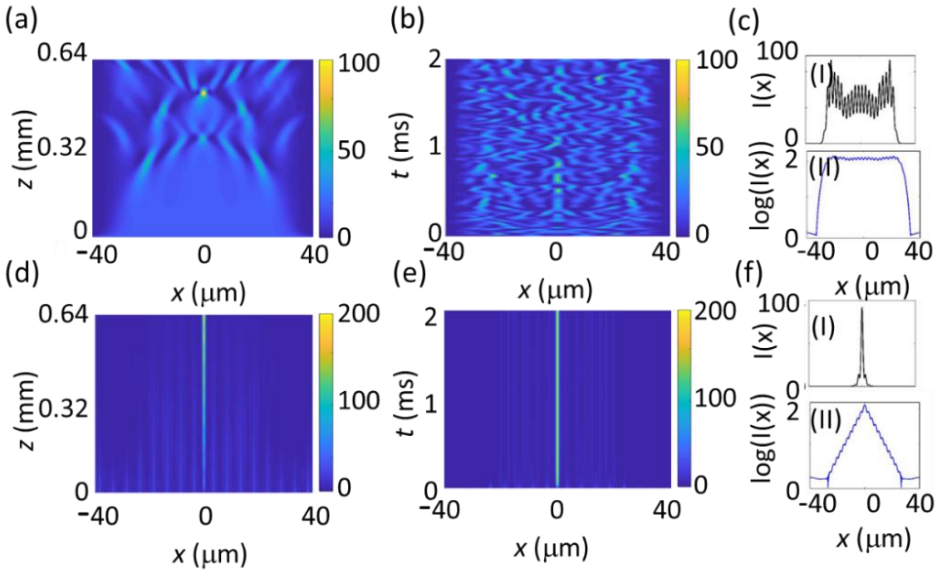

Figure 4.3. Unmodulated EE amplifier: (a) spatial intensity distribution and (b) temporal evolution of the output intensity for $p_0 = 1.23$ (arbitrary units). (c) (I) Output intensity profile and (II) its logarithm for a sufficient integration time. Modulated EE amplifier: (d) spatial intensity distribution, and (e) temporal evolution of the output intensity for $p_0 = 1.23$ (arbitrary units). (f) (I) Output intensity profile and (II) its logarithm for long enough temporal integration. Integration parameters: $m_1 = 0.5$, $m_2 = 0.021$ and $m_3 = -0.029$, $\Phi = 0$ and $p_0 = 1.23$.

The benefits of the proposed PT-axisymmetric scheme are evident when comparing the emitted beam with and without modulation. The spatio-temporal integration of the unmodulated EE amplifier shows both inhomogeneous spatial field distributions and unstable temporal behaviors, see Figs. 4.3 (a) and (b). The radiated emission may be regularized by introducing the mentioned pump and

refractive index periodic modulations inducing the local PT-symmetric profile. The light intensity is spatially localized and enhanced at the symmetry center, resulting into a bright and narrow emission, Fig. 4.3 (d). In addition to spatial regularization, the field becomes temporally stable, Fig. 4.3 (e). Consequently, the PT-axisymmetric potential directly impacts both spatial and temporal stability while improving the beam quality. In Fig. 4.3 (c), we can observe a transverse cut of the intensity profile, clearly inhomogeneous. In addition, the logarithm of the field intensity is almost constant along the transverse spatial coordinate

On the other hand, when an inward PT-axisymmetric potential is applied, the light is localized into a narrow beam, as energy increases exponentially in the central region, the logarithm of the field intensity shows a constant slope, see Fig. 4.3 (f).

The aforementioned effect caused by the local PT-symmetry directly impacts the performance of the proposed EE amplifier. The field becomes temporally stable and is spatially regularized. We explore the parameter space of the amplitudes of the modulations of the index m_2 and m_3, for a fixed value of the pump modulation amplitude, m_1, and a fixed phase, $\Phi = 0$.

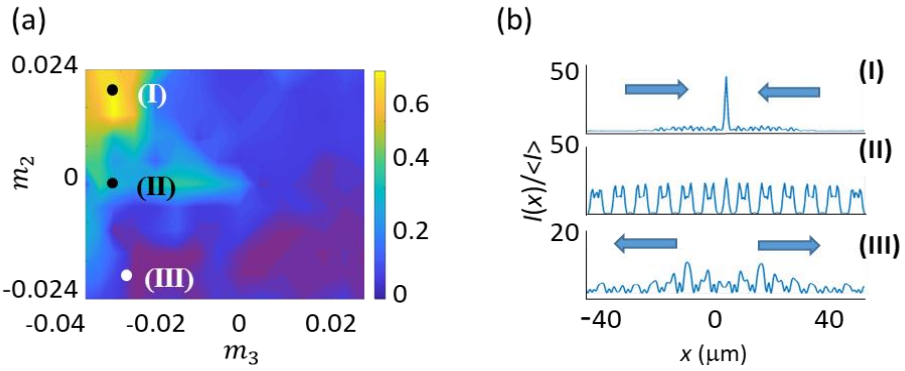

Figure. 4.4. (a) Axial concentration factor map in (m_2, m_3) parameter space for $m_1 = 0.5$ and $\Phi = 0$. (b) Transverse cuts of the intensity distributions, at $z = L$, normalized to the mean intensity, for three representative points of the map, corresponding to: (I) PT-axisymmetric distribution leading to inward mode coupling, $m_2 = 0.021$ and $m_3 = -0.033$; (II), symmetric mode coupling, in phase gain and index modulation $m_2 = 0$ and $m_3 = -0.033$; (III) local PT-symmetric distribution leading to outwards mode coupling $m_2 = -0.021$ and $m_3 = -0.029$.

Depending on the sign of the product $m_1 \cdot m_2$, we may expect regions of inward or outward mode coupling. The inward coupling (found for $m_1 \cdot m_2 > 0$) leads to an accumulation of the field around the center. For $m_2 = 0$, index and gain modulations are in phase, inducing a symmetric coupling and the observed field is homogeneously distributed. The outward coupling ($m_1 \cdot m_2 < 0$) leads to a

reduction of concentration in the center. Such light localization may be evaluated by a figure of merit, or field concentration factor, defined as the intensity at the center divided by the averaged intensity: $c = I(x=0)/\langle I \rangle$. Indeed, for $m_1 > 0$, we observe the maximum confinement for positive values of m_2 and negative values of m_3, while the concentration factor for $m_2 < 0$ is very small, consistent with the outward coupling. We assume a fixed value for the pump modulation amplitude, a fixed phase and explore the parameter space of the index modulations amplitudes m_2 and m_3, see Fig. 4.4 (a). The three above described possible situations regarding the transverse light localization are presented in Fig. 4.4 (b). For a positive value of m_3, positive, zero and negative values of m_2 and are respectively associated with inward, neutral and outward enhancement of the coupling.

For the case of the amplifier, we do not study the effect of the phase, Φ, that defines the character of the central axis, which may however play a more important role in EELs.

4.3 Edge-emitting lasers with local PT-symmetry

After validating the proposal in an EE amplifier, the next step is to introduce the PT-axisymmetric potential into an EEL. To model the laser, we may use the same rate equations, however accounting for both the forward and the backward fields and the corresponding longitudinal boundary conditions. The model used is the one presented in Eq. (2.7), in Chapter 2 section 2.1.2:

$$\begin{aligned} \pm\frac{\partial A^{\pm}}{\partial z} &= \frac{i}{2k_0 n}\frac{\partial^2 A^{\pm}}{\partial x^2} + \sigma[(1-ih)N-(1+\alpha)]A^{\pm} + i\Delta n(x)k_0 A^{\pm} \\ \frac{\partial N}{\partial t} &= \gamma(-N-(N-1)\left(\left|A^{+}\right|^2+\left|A^{-}\right|^2\right)^2 + p_0 + \Delta p(x) + D\nabla^2 N) \end{aligned} \tag{4.5}$$

where k_0 is the wave vector, n the refractive index, s is a parameter inversely proportional to the light-matter interaction length, h the Henry factor (linewidth enhancement factor of the semiconductor), α corresponds to losses, γ is the carrier's relaxation rate, p_0 the pump, and D is the carrier diffusion. The boundary conditions are straightforwardly determined by the Fabry-Perot cavity mirrors located at $z = 0$ and $z = L$ and are $A^{+}(z=0) = r_0 A^{-}(z=0)$ and $A^{-}(z=L) = r_L A^{+}(z=L)$ where L is the length of the laser and $r_{0/L}$ are the corresponding reflection of the

edge mirrors at $z = 0/L$, respectively. As in the previous section, we include the periodic modulations in the index and pump profiles aiming at generating spatially shifted effective pump and index profiles with either PT-symmetry with a global or a local character. To generate a global PT-symmetry, we consider the simplest sinusoidal modulation for the pump and refractive index, as described in Eq (4.4). However, for the desired local PT-symmetric potential, we consider instead:

$$\begin{aligned} \Delta p(x,z) &= m_1 sin\left(q_x |x| + \Phi\right) \\ \Delta n(x,z) &= m_2 \cos\left(q_x |x| + \Phi\right) + m_3 \sin\left(q_x |x| + \Phi\right) \end{aligned} \tag{4.6}$$

which depending on the three modulation amplitudes, namely (m_1, m_2, m_3), may create a PT-axisymmetric potential. In this case, the potential parameters under study are four, the three modulations amplitudes (m_1, m_2, m_3) and the phase, Φ, controlling the character of the center.

4.3.1 Study of the field localization

The emitted power in EELs is proportional to the pump (current density) and width of the laser. The spatio-temporal dynamics of the laser depend on these two main parameters. For either large pump values or broad widths, the output power of the laser increases while higher transverse modes appear in the field distribution inside the laser, and the laser emission becomes inhomogeneous and turbulent.

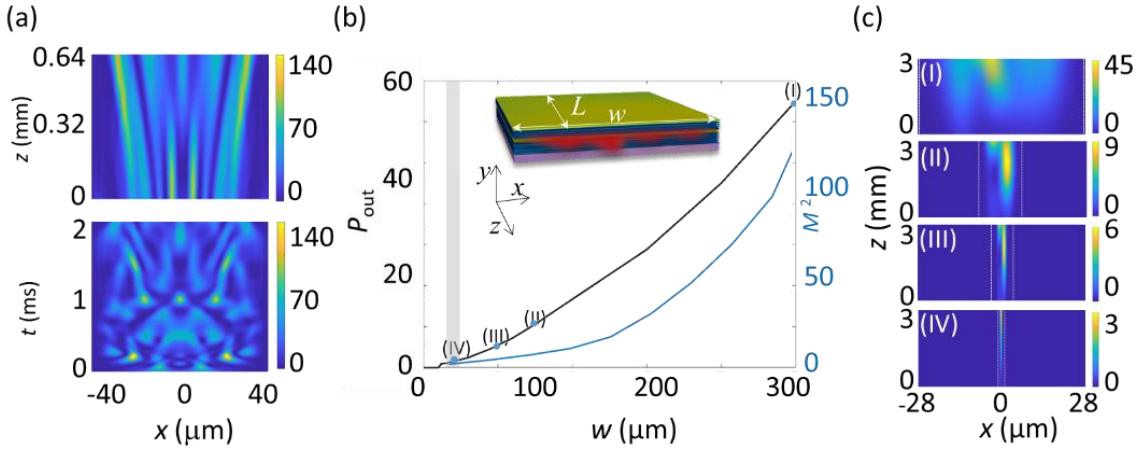

Figure. 4.5 (a) Inhomogeneous spatial intensity distribution inside the laser cavity and unstable laser emission for the unmodulated case. (b) Calculated output power (in black) of the unmodulated EEL as a function of the laser width (in arb. units) and corresponding quality factor

M^2 (in blue). (c) Spatial intensity distributions for the widths: (I) 15 μm; (II) 45 μm, (III) 75 μm, (IV) 300 μm.

We now apply the modulations described by Eq. (4.6). The idea is to reduce this inhomogeneity created by the apparition of new modes, filamentation and modulation instabilities (MI) by applying an axisymmetric PT-symmetry potential into lasers. A two-fold benefit is expected when axial PT-symmetric potentials are introduced, a bright emission in a narrow and intense output beam of high beam quality and the achievement of temporal stability. Both are consequences of the field localization at axis, i.e. the light generated in the whole laser width is directed to axis by the asymmetric coupling. The axial localization restricts transverse spatial modulations and associated spatio-temporal instabilities, see Fig. 4.6 (a). The narrow axial beam has a Gaussian-like shape with high beam quality (small M^2 values) and brightness, see the inset in Fig. 4.6 (b).

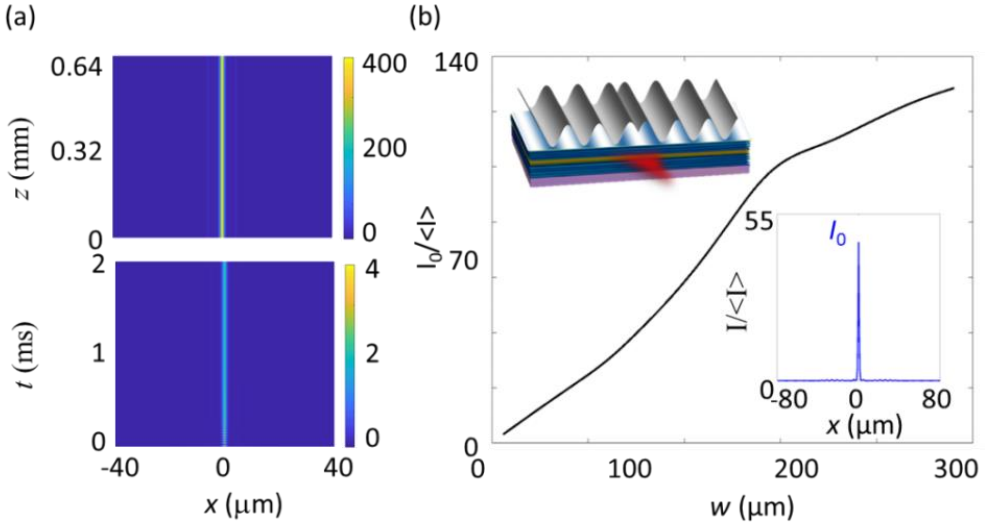

Figure 4.6. (a) Localized intensity inside the laser cavity and stable laser emission showing the central narrow and bright emitted beam for the EEL with axial PT-symmetric index and pump modulations with m_1 = 0.5, m_2 = 0.0048 and m_3 = -0.0143, p_0 = 1.23, Φ = π/4, r_0 = 0.99, r_L = 0.9 $and\ \gamma = 0.005$.(b) Concentration as a function of the laser width w and insets: scheme of a modulated EEL in index and pump and output beam profile.

We again evaluate the field concentration as the ratio between intensity at the axis and mean intensity, see Fig. 4.6 (b). This concentration increases linearly with the laser width following a constant and large slope. The intensity in the axis increases while the average intensity remains small up to the width value corresponding to the threshold. The slope is reduced for width values above threshold because the laser is lasing in the whole width and the average intensity

increases. As an interesting application, this light concentration may enable a direct coupling to an attached optical fiber without focusing lenses and associated energy losses.

4.3.2 Optimization of the modulation parameters

Finally, we study the performance of the EEL by scanning the parameter space as we did for the previously studied EE amplifier holding the same local PT-symmetry.

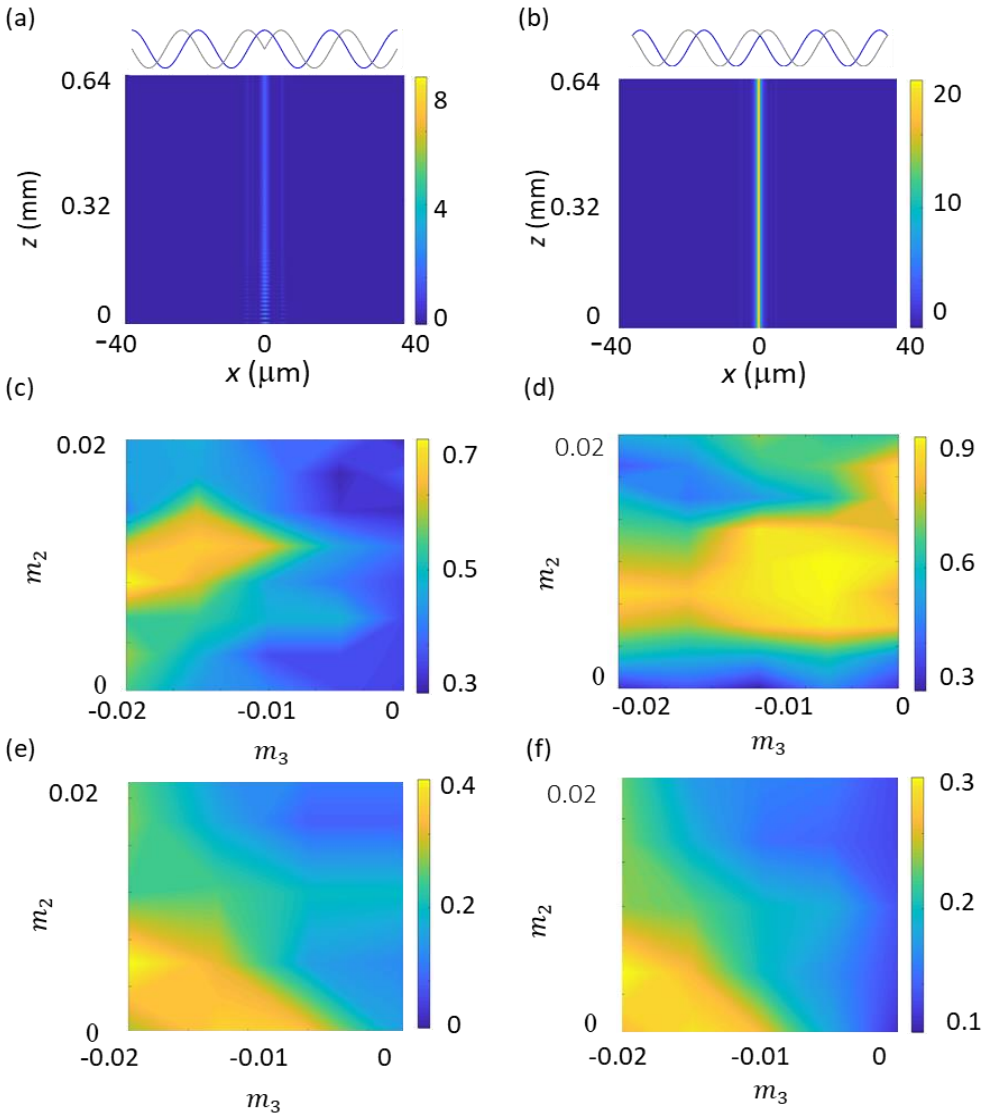

Figure. 4.7. (a) Index (blue) and gain (gray) PT modulation and typical localized spatial intensity distribution for the modulated EEL laser with axial PT-symmetry, (c) axial concentration factor

and (e) temporal stability map: amplitude of the temporal intensity oscillations mapped for $m_1 = 0.5$ in the (m_2, m_3) parameter space for and global dephase $\Phi = 0$. The same for a global dephase $\Phi = \pi/4$ plotted in (b), (d) and (f), respectively.

As expected, for an EEL, the character of the central defect controlled by the phase Φ, becomes more critical. It may be attributed to the system feedback imposed by the cavity. The optimum situation for field concentration is $\Phi = \pi/4$, since gain-maxima are located closer to the center, while an index relative maximum is still present at $x = 0$, preserving the index guiding effect. Thus, the field concentration reaches maximum values, and the stable regions become larger for $\Phi = \pi/4$, compare Figs. 4.7 (c) and (d). This optimal value for the global phase can be attributed to the positive values of both gain and refractive index at axis while index or gain becomes zero for $\Phi = 0$ or $\Phi = \pi/2$, see profiles in Figs. 4.7 (a) and (b).

In turn, the required amplitudes of both m_2 and m_3 are smaller than the required for spatio-temporal stabilization of a standard EE amplifier. The reduction in these values is attributed to the long effective cavity length, on the order of $10^2 \cdot L$ for the considered reflectivities. We also obtain a minimum of the required modulation amplitudes and a maximum enhancement and concentration for the optimal phase value $\Phi = \pi/4$, see Fig. 4.7 (b). Larger modulations of the complex refractive index (larger values of m_2 and m_3) are needed for $\Phi = 0$ and $\Phi = \pi/2$, presented in Fig. 4.7 (a), to obtain a similar effective inward coupling, note that for $\Phi = \pi/4$ the area of maximal axial concentration, mapped on Fig. 4.7 (d), is slightly shifted to smaller amplitude values as compared to Fig. 4.7 (c).

4.3.3 General laser performance

The general performance of the EEL can be analyzed in different working conditions by considering the homogeneous input pump, p_0, and the pump's modulation amplitude, m_1, keeping the index modulation amplitudes, m_2 and m_3 optimized and proportional to m_1. As might be expected, increasing m_1, the lasing threshold of the central area decreases, see Fig. 4.8 (a).

For small pump powers, lasing is mainly restricted to the central area with a high-intensity concentration factor, see Fig. 4.8 (b). A bright and narrow beam is generated below the homogeneous laser threshold ($p_0 = 1.2$) for sufficiently high modulation amplitudes. For $p_0 > 1.2$, amplification occurs in all the active material while localization persists, see the slope change of dotted lines in Fig. 4.8 (c). The average generated intensity increases with the pump, almost independent of the

potential amplitude, either for the unmodulated or modulated EEL, see the solid curves in Fig. 4.8 (c).

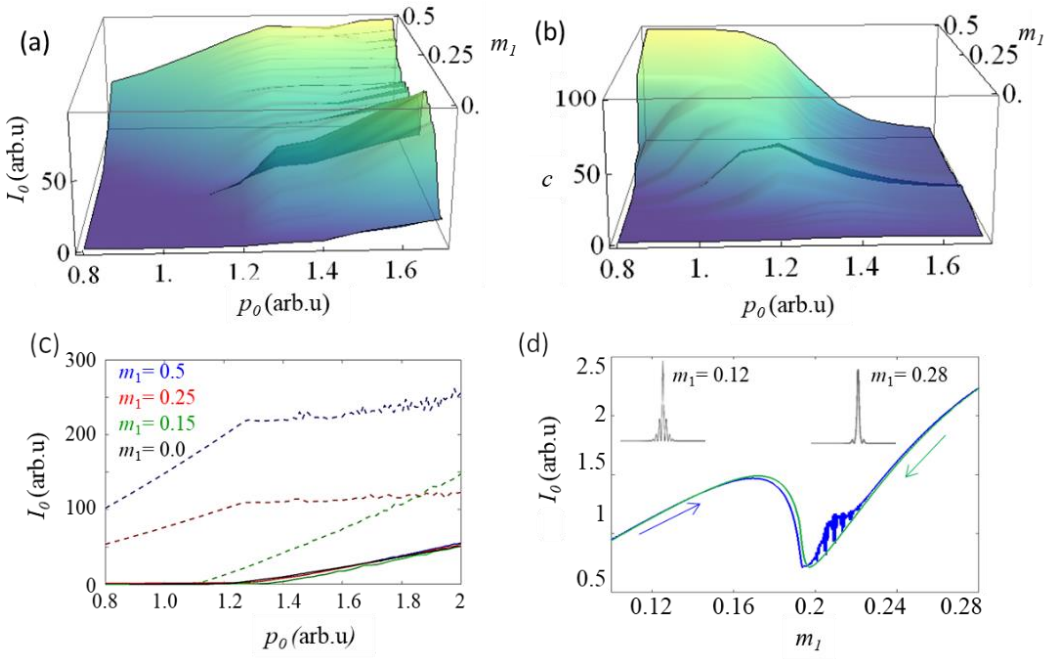

Figure 4.8. (a) Intensity at x = 0, I_0, as a function of the pump, p_0, and the pump modulation amplitude m_1, assuming the optimized corresponding values for the index modulations amplitudes m_2 and m_3. (b) Intensity concentration, $c = I_0/\langle I(x)\rangle$. (c) Central intensity I_0 (dashed curves) and mean intensity $\langle I(x)\rangle$ (solid curves) for different values of the pump p_0, as a function of m_1. The unmodulated case (black curve) is depicted for comparison. (d) Central intensity for p_0 = 1.23 showing a transition around m_1 = 0.2 with different transverse mode localization profiles, when integration is performed increasing/decreasing the m_1 value. All other parameters are the same as in Fig. 4.4, except $r_L = 0.04$.

We note that for small modulation amplitudes of the local PT-symmetric potentials, the peak intensity I_0 grows faster, increasing the pump while having less concentration. This is attributed to the existence of different transverse profiles, we observe wide/narrow peaks for small/large values of m_1, see Fig. 4.8 (d).

Moreover, the lasing threshold curve in Fig. 4.8 (a) shows different clear slopes in the p_0-m_1 plane for both peak transverse profiles. The transition between these profiles does neither show hysteresis nor bistability, see Fig. 4.8 (d). We note that these calculations are performed for a set of parameters restricted to realistic values.

A final interesting idea to further improve the laser emission is to replace the conventional multilayer mirror with constant reflectivity with a Gaussian mirror. Gaussian mirrors, also known as VRM (variable reflecting mirrors), are characterized by a reflection function that slopes from the center of the optic in a Gaussian distribution, see Fig 4.9 (b) for the designed wavelength instead of a constant reflection, as in Fig. 4.9 (a).

In this way, the mirror contributes to enhancing the localization of light. Moreover, inspecting the stabilization effects, we observe that introducing the GM the emitted beam presents smaller modulation amplitudes m_2 and m_3, note that the scales in Figs. 4.9 (a) and (b) are different.

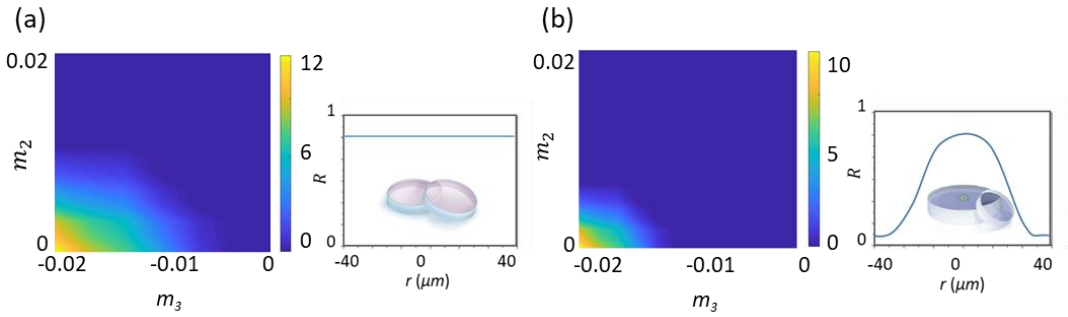

Figure 4.9. Temporal stability maps of the EEL: amplitude of the temporal intensity oscillations as a function of the amplitudes of the PT-axisymmetric potential, namely m_2 and m_3, for two different situations: (a) constant-reflectivity conventional multilayer mirror (b) Gaussian mirror. The insets show the reflectance curves as a function of the radial position.

4.4 Conclusions

To conclude, we show a feasible and compact scheme to control and stabilize the spatio-temporal dynamics of EELs. The proposal is based on the ability of non-Hermitian potentials with given local symmetries to manage the flow of light based on asymmetric mode coupling. We impose a pump modulation with a central symmetry axis which induces in-phase gain and refractive index modulations due to the Henry factor. Both modulations are, in turn, spatially shifted by an appropriate index profile that divides the modified EEL into two mirror-symmetric half-spaces holding PT-symmetry with opposite mode coupling. Such local non-Hermitian potential induces an inward mode coupling, accumulating the light generated from the entire active layer at the central symmetry axis, ensuring spatial regularization and temporal stability. By an

exhaustive exploration of the modulation parameters, we significantly improve the intensity concentration, stability, and brightness of the emitted beam. This approach produces a twofold benefit: light localization into a narrow-beam emission and the control over the spatio-temporal dynamics, improving the laser performance.

Publication V

J. Medina, M. Botey, R. Herrero, and K. Staliunas, *"Stabilized narrow-beam emission from broad-area semiconductor lasers,"* Physical Review A **101**(3), 033833 (2020).

ATTENTION¡¡
Pages 112 to 116 of the thesis, containing the article mentioned above are available at the editor's web

Publication VI

[Med20-2] J. Medina, M. Botey, R. Herrero, and K. Staliunas, *"Spatiotemporal stabilization of PT-symmetric BAS lasers,"* Society of Photo-Optical Instrumentation Engineers (SPIE) Conference Series. Vol. 11356. 2020.

ATTENTION¡¡
Pages 118 to 124 of the thesis, containing the article mentioned above are available at the editor's web
https://opg.optica.org/ol/abstract.cfm?uri=ol-43-11-2511

Publication VII

[Med19] J. Medina, M. Botey, R. Herrero, and K. Staliunas, *"Spatiotemporal stabilization of PT-symmetric BAS lasers,"* The European Conference on Lasers and Electro-Optics. Optical Society of America, 2019.

ATTENTION¡¡
Page 126 of the thesis, containing the article mentioned above is available at the editor's web
https://ieeexplore.ieee.org/document/8871755

Publication VIII

[Bot19] M. Botey, W. W. Ahmed, J. Medina, R. Herrero, and K. Staliunas, *"Non-Hermitian Broad Aperture Semiconductor Lasers Based on PT-Symmetry,"* 2019 21st International Conference on Transparent Optical Networks (ICTON). IEEE, 2019.

Publication IX

[Bot19-2] M. Botey, W. W. Ahmed, J. Medina, R. Herrero, Y. Wu, Y., and K. Staliunas, *"Regularization of broad-area lasers by non-Hermitian potentials,"* Proceedings of META 2019, The 10th International Conference on Metamaterials, Photonic Crystals and Plasmonic: Lisbon, Portugal, 23-26 July *2019*.

M ETA 2019, LISBON - PORTUGAL, JULY 23 – 26, 2019

Regularization of broad-area lasers by non-Hermitian potentials

M. Botey[1], W. W. Ahmed[2], Judith Medina[1], R. Herrero[1], Ying Wu[2], and K. Staliunas[1,3]

[1]Departament de Física, Universitat Politècnica de Catalunya (UPC), Barcelona, Catalonia
[2]Division of Computer, King Abdullah University of Science and Technology (KAUST), Saudi Arabia
[3]Institució Catalana de Recerca i Estudis Avançats (ICREA), Barcelona, Catalonia
[*]corresponding author: muriel.botey@upc.edu

Abstract- It was recently shown that arbitrary non-Hermitian optical potentials based on local Parity-Time (PT-) symmetry may control the flow of light, due to the asymmetric mode coupling. We propose periodic non-Hermitian potentials to efficiently regularize the complex spatial dynamics of broad-area semiconductor (BAS) lasers and Vertical-Cavity Surface-Emitting Lasers (VCSELs). Light generated from the entire active layer is concentrated on the structure axis, confined in an intense central narrow beam opening the path to design compact, bright broad-area lasers.

Semiconductor lasers are compact and efficient coherent light sources yet being generally unstable due to the due their large aspect ratio and to the lack of a transverse mode control mechanism. Spatial random fluctuations and spatiotemporal instabilities degrade the spatial beam quality and laser coherence [1]. This intrinsic instability gives rise to different nonlinear modal interactions such as filamentation, and hole burning limiting possible applications. Common techniques to control the complex dynamics of BAS and VCSELs semiconductor lasers generally compromise their compactness while reducing the power conversion efficiency,

The present paper proposes a novel solution to the need for a more general physical mechanism to stabilize the complex spatial dynamics in semiconductor lasers while improving the beam quality emission. In recent years, non-Hermitian spatially modulated materials have provided a flexible platform to manipulate the light wave dynamics. Simultaneous refractive index and pump modulations have already shown the capability to suppress spatial instabilities in nonlinear optical systems, particularly in BAS and VECSEL devices [2]. A particularly remarkable class of such materials is the one globally holding Parity-Time (PT-) symmetry [3], which may be regarded as particular class of non-Hermitian systems fulfilling spatial Kramers-Kronig relation [4]. One of the most interesting features of such materials is the unidirectional light transport arising from the unidirectional mode coupling. In turn, it was shown that local PT-symmetry may lead to light localization and enhancement at a selected point or complex potential may be specially designed using a local Hilbert transform, to control flow of light favoring arbitrary vector fields directionality using periodic, quasiperiodic or random background potentials [5].

We show how axisymmetric non-Hermitian potentials efficiently regularize VCSELs radiation achieving a stable bright emission, see Figs 1.a-e. Dephased periodic (radial) refractive index and gain-loss modulations accumulate the generated light from the entire active layer and concentrate it around the structure axis to emit narrow beams. We perform a comprehensive analysis to explore the maximum central intensity enhancement and concentration regimes. We observe such lasers can be operated in stationary or pulsating oscillatory regime depending on the relative amplitude and phase of the index and gain-loss modulations. The results indicate the

effect occurs coinciding when the coupling between transverse modes is inwards yet not fulfilling perfect PT-symmetry. We also apply an analogous scheme to control and improve the spatiotemporal dynamics in BAS lasers, see Figs.1f-i. The BAS proposed modulation devides the structure in two half-spaces with two symmetric PT-symmetric potentials, by introducing a modulation both in the pump and refractive index. The generated light is directed towards the symmetry axis when to form a narrow and bright emitted beam.

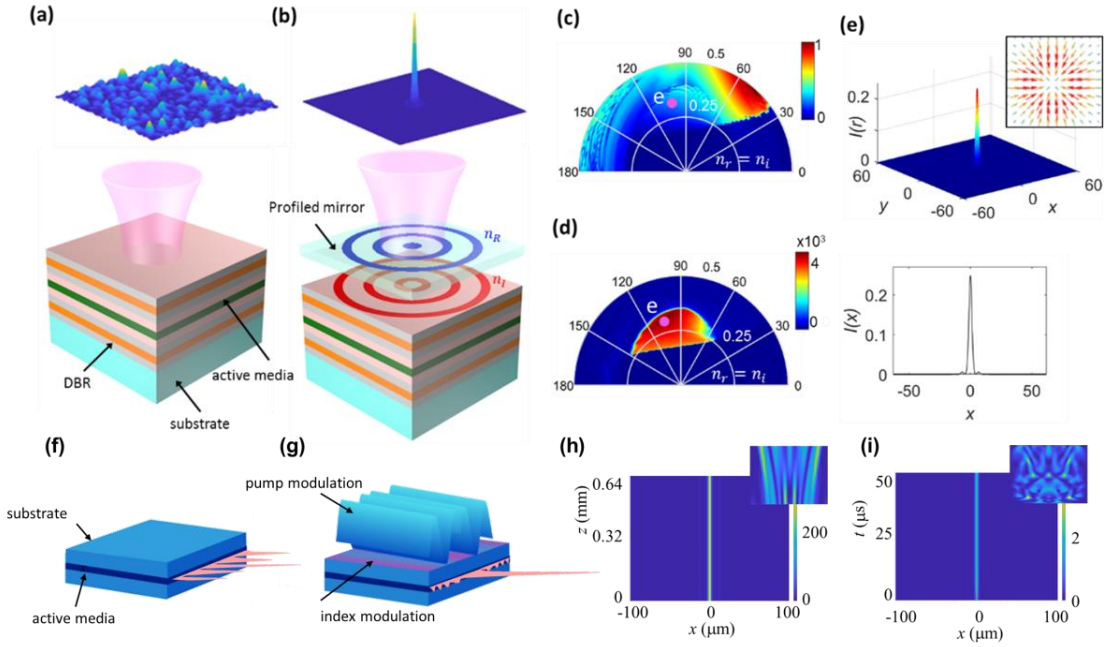

Fig. 1 (a)/b) Complex irregular/bight and narrow beam emission form conventional/structured broad-area VCSELs; (blue, n_R: index, red, n_I: gain-loss); (c) central intensity enhancement C=[$I(r=0)$.Area]/ $\int I(r)dr$; (d) axial concentration factor in parameter space (n_I, ϕ); (e) intensity profile and corresponding axial cross-section in stationary state. The inset illustrates the transverse field flow around the center, showing the unidirectional inward radial coupling. (f)/(g) Complex irregular/bright and narrow emission from conventional/structured BAS lasers; (h) intensity distribution within the BAS laser; (i) temporal evolution of the output intensity profile of the modulated BAS laser. The insets show the same intensity profiles for an unmodulated BAS laser.

The reported field regularization effect is universal and analogous field concentration, the study uncovers rich possibilities for various configurations which could be extended beyond periodic non-Hermitian potentials assuming different random, quasiperiodic complex profiles of the background potential. We expect the proposed mechanism to be applicable to regularize the radiation from actual broad aperture lasers and microlasers.

REFERENCES

1. J. Othsubo, Semiconductor Lasers: Stability, Instability and Chaos (Springer, Heidelberg, 2013).
2. R. Herrero, M. Botey, M. Radziunas, and K. Staliunas, Opt. Lett. 37, 5253 (2012), S. Kumar, R. Herrero, M. Botey, and K. Staliunas, Opt. Lett. 39, 5598 (2014)
3. C. M. Bender and S. Boettcher, Phys. Rev. Lett. 80, 5243 (1998),
4. W. W. Ahmed, R. Herrero, M. Botey, and K. Staliunas, Phys. Rev. A 94, 053819 (2016).
5. S. A. R Horsley, M. Artoni, and G. C. La Rocca. Nat. Phot. 9.7, 436 (2015)
6. W. W. Ahmed, R. Herrero, M. Botey, Z. Hayran, H. Kurt, and K. Staliunas, Phys. Rev. A 97, 033824 (2018).

Publication X

[Med20-3] J. Medina, R. Herrero, M. Botey, and K. Staliunas, *"Stabilized Bright Narrow Beams from Edge-Emitting Lasers,"*2020 22nd International Conference on Transparent Optical Networks (ICTON). IEEE, 2020

Chapter 5

Spatio-temporal stabilization of an array of edge-emitting lasers

5.1 Symmetric and asymmetric coupling between lasers

As presented in Chapter 1 section 1.1.1, the low beam quality is an essential drawback for the applications of Edge-Emitting Lasers (EELs) and EEL bars, mainly due to the high M^2 values that difficult the coupling to optical fibers. Indeed, this is of even higher importance for bar modules pumping a fiber laser. In this case, the pumping beam quality determines the number of modes coupled inside the active fiber of a given size and numerical aperture. The proposal presented in this chapter allows to obtain stable emission from EEL sources and the direct coupling to an optical fiber without any additional optical component, which should enormously enhance the coupling efficiency.

To attain this goal, the broad EEL is split in an array of thinner lasers with a non-Hermitian coupling to obtain stable emission from the EEL array and improve its beam quality and energy distribution within the laser array. The light generated in every single semiconductor laser is expected to be spatially redistributed and temporally stabilized via the non-Hermitian coupling between neighboring lasers. The non-Hermitian coupling is induced by a particular transverse shift, s, between the gain profile (pump) and index profile (stripes). All the results presented in this Chapter are published in Ref. [Med21].

However, splitting a broad EEL source in an array of thinner lasers, each one operating with a monomode stable emission when isolated, is not a solution since new temporal and synchronization instabilities arise from the coupling between neighboring lasers, leading again to irregular spatio-temporal behaviors. Thus, we propose a non-Hermitian asymmetric coupling between EELs composing the array to stabilize and redistribute the light emission increasing the quality of the emitted beam.

For this purpose, we should first identify the onset of spatio-temporal instabilities for a single laser source, in other words, for which parameters the emission is monomode and temporally stable. Secondly, we should characterize the non-Hermitian coupling between two neighboring lasers and the different dynamical phenomena arising from the coupling of an increasing number of neighboring lasers. Finally, we apply a mirror-symmetric non-Hermitian configuration to generate a central localization of the field generated in the whole array.

5.1.1 Model for semiconductor laser arrays

To model the spatial redistribution and temporal stabilization of the field in coupled EELs, we use the model previously presented in Chapter 2, section 2.1:

$$\begin{aligned} \pm\frac{\partial A^{\pm}}{\partial z} &= \frac{i}{2k_0 n}\frac{\partial^2 A^{\pm}}{\partial x^2} + \sigma[(1-ih)N-(1+\alpha)]A^{\pm} + i\Delta n(x)k_0 A^{\pm} \\ \frac{\partial N}{\partial t} &= \gamma(-N-(N-1)\left(\left|A^{+}\right|^2+\left|A^{-}\right|^2\right)^2 + p_0 + \Delta p(x) + D\nabla^2 N) \end{aligned} \tag{5.1}$$

The considered parameters are the same presented in Chapter 2 Eq. (2.7) and in the following calculations, the transverse and longitudinal spatial coordinates are in units of the wavelength.

Finally, the transverse profiles of the refractive index $\Delta n(x)$ account for the individual laser stripes and the pump, $\Delta p(x)$, for the spatial profile of the electrodes. Both profiles have the same shape, satisfying $\Delta n(x)/\Delta n = \Delta p(x-s)/p$ where s is the shift between them and induce the real and imaginary parts of the non-Hermitian potential, which, properly designed, may lead to an asymmetric field coupling, see Fig. 5.1 (a) for a schematic representation of the presented laser architecture. To avoid discontinuities in the derivatives of these modulations, the two spatial transverse profiles are mathematically described as consecutive sharp sigmoids.

5.1.2 Characterization of a single EEL

First, we numerically study a single EEL through the model described in Eq. (5.1), to determine its dynamics for different working conditions. As it is well known, a laser width reduction acts as a mode selection mechanism and as a result, the broad and strongly multimode semiconductor emission turns into a monomode emission regime.

The width of a single EEL is scanned to analyze the emitted field profile seeking for the onset of the laser monomode emission. Figure 5.1 (b) shows the total emitted output power from a single EEL for widths ranging from 2.5 μm to 50 μm. It can be compared with the analytical maximum width for a monomode emission, determined by $w_{\max} = \lambda/\sqrt{2n\Delta n}$ .The general operating parameters chosen in Fig. 5.1 correspond to 4 μm, in good agreement with the integrated beam profiles. In turn, we calculate the beam quality factor, M^2, as the ratio

between the Beam Parameter Product (BPP) of a real beam and a Gaussian beam, which can be numerically evaluated as: $M^2 = \frac{BPP_{actual\ beam}}{BPP_{Gaussian\ beam}} = \frac{\pi w \theta}{\lambda}$, where w and θ are the beam width in near-field and far-field, see Chapter 1 section 1.2.1 for more details.

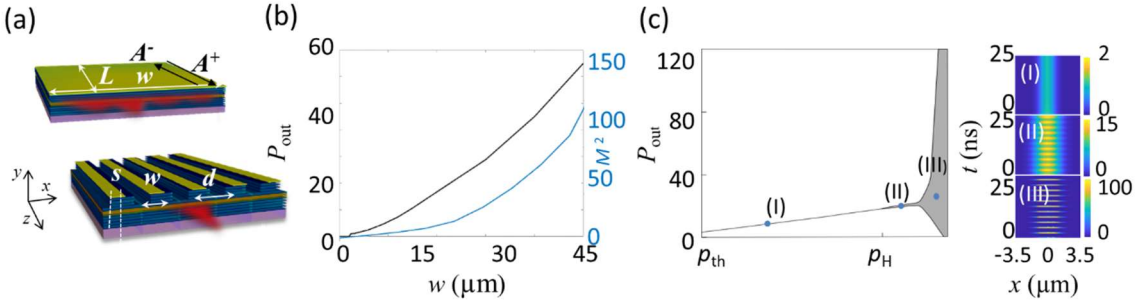

Figure 5.1. (a) Scheme of a broad single EEL where the index and pump profiles coincide, w is the width and L the length of the laser, and scheme of a laser array of thinner EELs separated a distance d with non-Hermitian coupling. (b) The output power of the EEL as a function of the laser width (in black) and M^2 (in blue) numerically obtained from Eq. (5.1); (c) Temporal evolution of the transverse intensity profile within the laser for w = 2.5 μm and different pumps, normalized to the emission threshold p_{th}: I p = 1.1 p_{th}, II p = 1.8 p_{th}, III p = 1.9 p_{th}, and bifurcation diagram showing the maximum and minimum values of the oscillating output power as a function of the pump; p_H indicates the onset of the instability.

The M^2 strongly increases with the laser's width as the laser becomes more multimode and inhomogeneous as has been already discussed in Chapter 4, see Fig. 5.1 (b).

However, while a narrow width in a semiconductor laser indeed acts as a transverse mode selection mechanism, it does not warrant its temporal stability. The temporal behavior is observed in Fig. 5.1 (c), where the temporal stability of a monomode laser of w = 2.5 μm is scanned as the pump function. The results show a Hopf bifurcation arising at a particular pump, referred to as the Hopf pump, p_H. For pump values above this threshold, the laser, remaining monomode becomes temporally unstable, see the insets of Fig. 5.1 (c). The smooth oscillations observed just after the Hopf bifurcation present periods of about 20 roundtrips and are only visible in the small pump interval shown in the figure, while for larger pump values, sharp peaks with an almost zero background appear. When scanning the pump upwards, pulses rapidly increase in amplitude.

We further analyze the effect of adding a displacement between the pump and the refractive index profiles. We observe that around $s = 0.35$ μm all the energy created in the laser is lost, see Fig. 5.2 (a). A physical insight to this effect is found calculating the transverse spatial tilt of the electric field phase within the laser. It indicates a transverse shift of light propagating along the laser and coming out from the laser stripe, Fig. 5.2 (b). As expected, such phase is symmetric and flat in the laser center for a symmetric coupling. The phase slope increases with the asymmetry parameter s, indicating more tilt in the field propagation and more energy transfer to the neighboring laser, as seen in Fig. 5.2 (c). Thus, an s shift between profiles will clearly induce a directionality in the coupling between lasers.

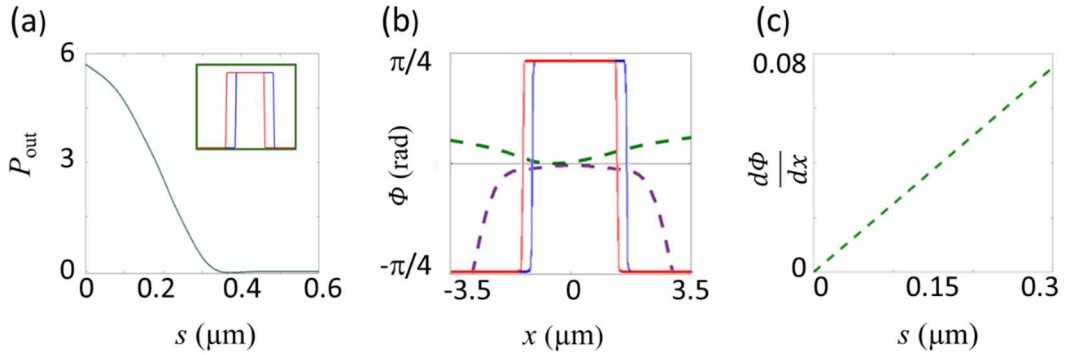

Figure 5.2. (a) Loss of output power for a single laser when the transverse shift s between pump and index profiles increases. Pump and index profiles in red and blue, respectively. (b) Field phase for $s = 0$ μm (dashed purple curve) and for s = 0.15 μm (dashed green curve), and (c) field phase slope $d\Phi/dx$ at the central point of the laser as a function of s. The integration parameters are: L= 500, α = 0.1, h = 2.0, σ = 0.06, D = 0.03 and γ = 0.005, and the units in the graphs correspond to $\lambda = 1$μm, $n_0 = 3.5$ and $\Delta n = 0.06$.

5.1.3 Symmetric and asymmetric coupling for two EELs

Once the main dynamics and parameters of a single laser are determined, we analyze the effect of the coupling between lasers on the spatiotemporal dynamics. Such coupling depends on the distance between neighboring lasers and the displacement between the laser profile and the pump, as schematically shown in Fig. 5.2 (b). We first analyze the coupling between two identical lasers with the same intrinsic parameters and where the index and the pump profiles perfectly coincide (s = 0 μm) and are, therefore, symmetrically coupled. While the standing-alone laser has a spatially and temporally stable emission for a given set of parameters, as the distance between coupled lasers decreases —the

coupling strength increases— both lasers become temporally unstable, Fig. 5.3 (b).

Spatial asymmetries are evident in every snapshot of the numerically calculated intensity distribution of two close EEL sources, see Fig. 5.3 (a) and (b). This effect is due to the symmetric interchange of energy between both lasers. Next, we slightly shift the index profile of both lasers with respect to the gain profiles to induce a mirror-symmetric coupling. As expected, the light generated in one laser is partially transferred to the other one, see Fig. 5.3 (c). The energy is directed due to the asymmetric coupling and both lasers become temporally stable, as shown in the temporal evolution of the intensity transverse profile in Fig. 5.3 (d). This temporal stabilization tendency increasing the coupling asymmetry agrees with the general behavior of coupled non-linear oscillators, generally showing less complex dynamics for unidirectional than for bidirectional couplings.

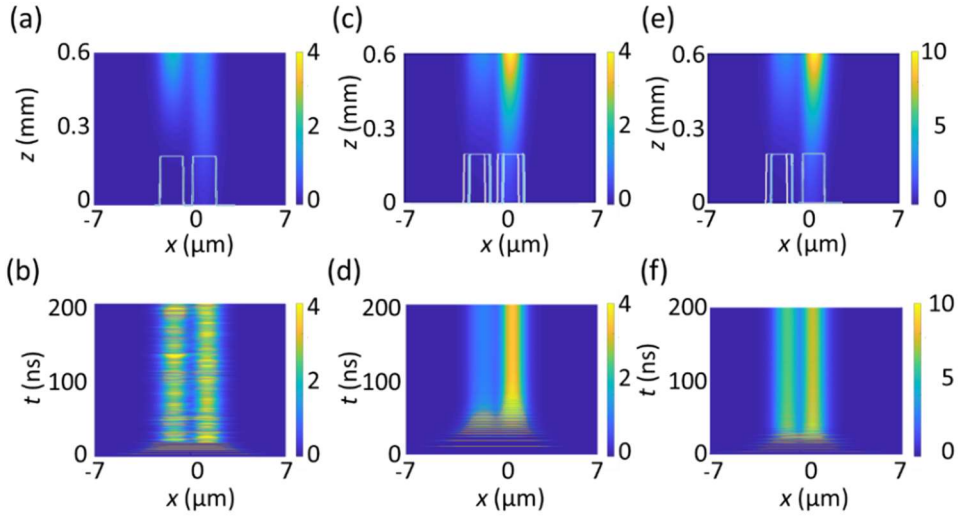

Figure 5.3. (a)/(c)/(e) Snapshots of the spatial intensity distribution after sufficient integration time for two symmetrically/asymmetrically/single transverse shift coupled lasers, and (b)/(d)/(f) temporal evolution of the intensity at z = L for two symmetrically/asymmetrically/single transverse shift coupled lasers with w = 2.5 μm, separated a center-to-center distance d = 3 μm and for s = 0.25 μm. Insets show the transverse pump profile Δp (white profile) and the index profile Δn (blue curve), and they coincide in (a).

We can observe that while the energy is enhanced in one laser, some energy is leaked in the other laser due to the asymmetric configuration, asymmetrically coupled out from the laser. We previously analyzed this effect considering a single laser, as observed in Fig. 5.1 (a). Therefore, the energy transfer can be optimized by considering a single transverse shift, i.e., no shift for the laser to

which the energy is transferred, Fig. 5.3 (e) and (f). We can compare this last configuration with the double transverse shift configuration inspected in Fig. 5.3 (c).

The performance of the proposed asymmetric coupling is assessed by the asymmetric energy enhancement and temporal stability of the attained regimes. We calculate the enhancement as the relative intensity of the laser to which the energy is accumulated, i.e., the ratio of the temporally averaged intensity of the enhanced laser, for $s \neq 0$ μm, versus the unshifted case, $s = 0$ μm. We explore the parameter space of the distance between lasers, d, and asymmetry shift parameter, s (spatial shift between the pump and the refractive index profiles) for a fixed pump value. The results are summarized in Figs. 5.4 (a).

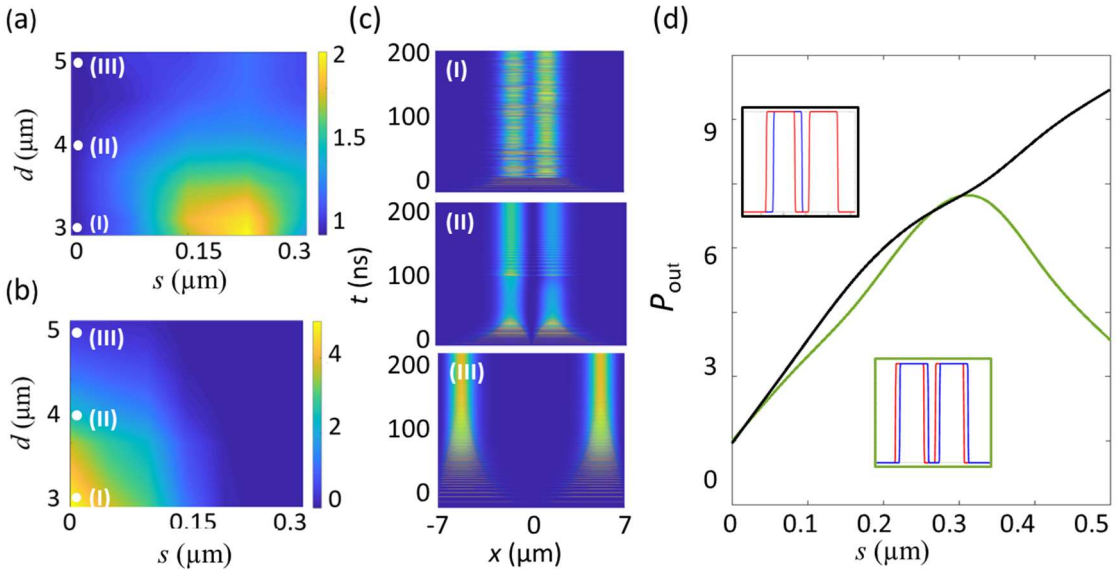

Figure 5.4. (a) Intensity enhancement factor of the amplified laser depending on the distance between lasers, d, and spatial shift, s. (b) Temporal instability map. The relative amplitude of the temporal oscillations (normalized to the average amplitude). (c) Temporal evolution of the intensity at z = L for three different distances d. (d) Comparison of the output power for two coupled lasers with asymmetric lateral coupling with single (black) and double transverse shift (green) as a function of s. All the integration parameters are the same as in Fig. 5.1, except p_0 = 2.5.

A monotonous field enhancement is expected by increasing the shift parameter s. However, we observe that the effect reaches a maximum around a given shift value, namely $s \approx 0.25$ μm. This behavior for high values of s may be attributed to the asymmetric configuration of both lasers, which also induces an asymmetric leaking of energy opposite the other laser's direction. Therefore,

such leaked energy is lost, and the net gain for the whole system is reduced, being the largest relative intensity of the enhanced factor around 2. Moreover, such enhancement increases for a smaller distance, d.

In addition, the temporal stability of the emission may be evaluated by mapping the amplitude of the temporal oscillations of the enhanced laser also in the distance-shift, (d,s), parameter space, see Fig. 5.4 (b). Temporal instabilities arise for small d and s values, i.e., when the distance between lasers or coupling asymmetry decrease. For center-to-center distances close to the laser width, the emission is unstable for all values of s. On the contrary, stability is found either increasing the coupling asymmetry for a given laser distance or, trivially, at more considerable distances between lasers, Fig. 5.4 (c). Interestingly, inspecting Fig. 5.4 (a) and (b), we observe a range of parameters around the maximum relative intensity region that coincides with a temporally stable behavior.

The double-shifted configuration achieves a maximum output power for an s value of about 0.25 μm and decreases due to the energy leakage. In contrast, the single-shifted case keeps increasing with s, observed in Fig. 5.4 (d). Temporal instabilities also disappear for the single shift case increasing s parameter, and the amplitude of the temporal oscillations shows a similar (d,s) dependence. The spatial intensity distribution and the temporal evolution for the single shift configuration are provided in Figs. 5.3 (e) and (f) showing more than twice the emission of the double shifted scheme of Fig. 5.3 (c) and (d).

5.2 Axisymmetric inward coupling between EELs

The next step is to consider a simple array architecture formed by three coupled lasers with a mirror-symmetric coupling with a central symmetry axis. That is to say, two symmetric lasers holding asymmetric shifts between gain and index profiles and a central one with no shift. The coupling is expected to increase for such a configuration as the distance decreases, eventually reaching a temporally stable regime as light is localized inwards, i.e. to the axis.

The numerical results for the three coupled lasers are summarized in Fig. 5.5. It can be observed that when symmetrically coupled, all three lasers are temporally unstable as intensity maxima switches from one laser to another see Figs. 5.5 (c) and (d). On the contrary, as the non-Hermitian potential is

introduced through an inward symmetric shift to the axis of the index profile, the generated light tends towards the central laser, and all lasers become stable, see Fig. 5.5 (e) and (f). We note that the fulfilled redistribution and spatial stabilization lead to enhanced intensities compared with the two-laser case in this scenario.

The performance of the proposed mirror-symmetric lasers triad is evaluated by the relative intensity of the central laser, i.e., the intensity of the enhanced laser, for $s \neq 0$, versus the unshifted case, $s = 0$. Comparing Fig. 5.5 (a) and Fig. 5.4 (a), we observe the maximum intensity for a somewhat larger value of d. Besides, a larger enhancement ratio is reached as energy is coupled from the two neighboring lasers.

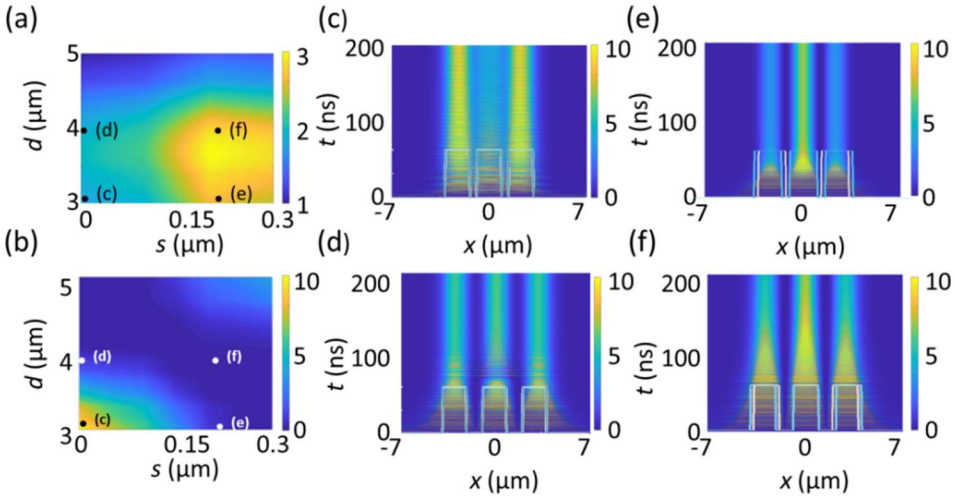

Figure 5.5. (a) The relative intensity and (b) amplitude of the temporal oscillations depending on the distance between lasers, d, and spatial shift, s. (c)/(e) Snapshots of the spatial intensity distribution of the intensity for a triad of lasers with symmetric/inward-axisymmetric coupling after sufficient integration time and (d)/(f) temporal evolution of the intensity at z = L for three lasers with symmetric/inward-axisymmetric coupling with w = 2.5 μm, separated a center-to-center distance d = 3.0 μm and for s = 0.25 μm. Insets show the transverse pump profile Δp (red curve) and the index profile Δn (blue curve). All the integration parameters are the same as in Fig. 5.2.

The emission's temporal stability is evaluated by mapping the temporal oscillations of the central laser in the distance-shift parameter space (d, s) for a fixed pump value. The results show a maximum energy localization range for small distances around 3.5 μm, and shift parameter $0.15 \leq s \leq 0.25$. Precisely this set of parameters coincides with temporal stability, assessed by mapping the temporal oscillations of the central laser. If we inspect Figs. 5.5 (a) and (b), we assert that temporal stability is achieved for a simultaneous light localization. In

this case, temporal stability reappears at larger distances for significant values of the shift parameter.

5.3 Axisymmetric array of EELs with inward coupling

An EEL array composed of many lasers with an axisymmetric inward coupling can be created by combining the asymmetric lateral coupling studied for two lasers and the axisymmetric inward coupling presented for three lasers. The proposed scheme is a laser without any shift between index and pump profiles located on a central axis and the rest of lasers presenting index profiles shifted to the axis with respect to pump profiles. The proposed scheme is depicted in Fig. 5.1 (a). The array is divided into two half-spaces with a symmetric spatial shift between gain and transverse index profiles, arranged such that the index lays closer to the symmetry axis and the central laser holding no displacement. Thus, we expect light generated within the array to be directed to the axis due to the asymmetric coupling, localizing the energy and improving the beam quality.

5.3.1 Axisymmetric multiple laser array

The emission of the laser array with and without non-Hermitian coupling is compared in Fig. 5.6, for 7 and 13 laser arrays.

Arrays with symmetric couplings, s = 0 μm, show inhomogeneous field distributions and complex temporal evolutions. The field distributions of the two configurations after long integration times can be observed in Figs. 5.6 (a) and (c). The same laser arrays with axial non-Hermitian modulations show regular emissions. The light is directed towards the central laser, reaching a Gaussian-like envelope in the transverse profile and increasing the array's beam quality. Figures 5.6 (b) and (d) show such stable distributions for a displacement of s = 0.25 μm.

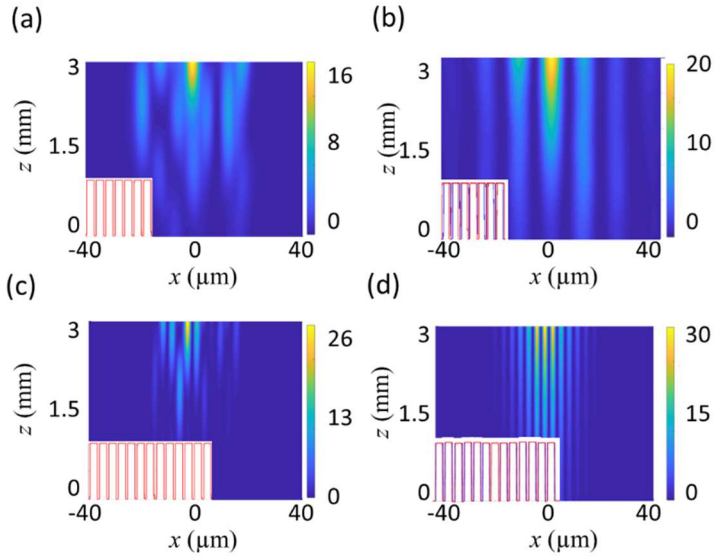

Figure 5.6. Spatial distribution of the intensity for 7/13 laser arrays after sufficient integration time for (a)/(c) a symmetric coupling and (b)/(d) an axial non-Hermitian coupling with s = 0.25 μm. All lasers have a w = 2.5 μm, separated with a center-to-center distance d = 3.0 μm. Insets show the transverse pump profile Δp (red curve) and the index profile Δn (blue curve), they coincide in (a).

This transverse non-Hermitian coupling presents a twofold benefit: the stabilization of the emission of the laser array, and an increase of the output intensity of the central laser along with an increase of the beam quality. The output intensity of the central laser depends linearly on the number of lasers due to the accumulation of the energy generated by all lasers in the central part of the array, see Fig. 5.7 (b). The beam quality, displayed by the M^2 parameter defined in Chapter 1, is used to compare three cases, see Fig. 5.7 (c). The array with symmetric coupling between lasers (black line), the same array with an axisymmetric inward coupling (blue line), and a single broad laser with a width equivalent to the active width of the array (red line). In the broad laser case, M^2 increases exponentially with the laser width as new modes appear, and the laser becomes highly inhomogeneous.

The beam quality is clearly improved by splitting the active area in many lasers with symmetric coupling, the values of M^2 increase linearly with the number of lasers. More interesting is the case of inward asymmetric coupling, which highly increases the beam quality and strongly smooths its dependence on the number of lasers. Both improvements together demonstrate the proposal's viability and allow a direct coupling into the fiber by just using the light emitted by the central laser.

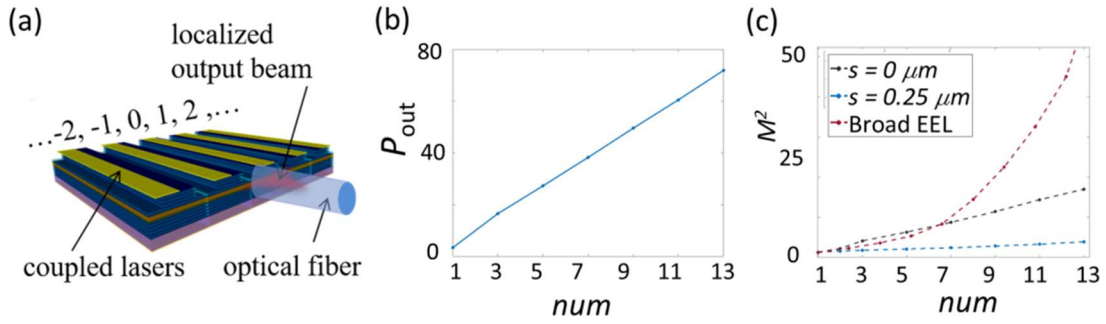

Figure 5.7. (a) Scheme of the array of coupled lasers directly coupled to an optical fiber. (b) Output power dependence on the number of laser lasers (*num*) for the axisymmetric inward coupling scheme. (c) Dependence of M^2 with the number of lasers (*num*), for three different cases, in red a broad EEL of equivalent width, in black the array of lasers with symmetric coupling, and in blue the array of lasers with axisymmetric inward coupling.

5.3.1 Asymmetric multiple laser array with punctual and non-diffractive model

The presented results provide proof of the working principle and a comprehensive understanding of the asymmetric coupling of the proposed scheme. Next, the same concept is extended to EEL bars composed of many lasers. For this purpose, we develop a simplified model, accounting for the longitudinal propagation, temporal evolution, and coupling between lasers but disregarding diffraction, $\frac{\partial^2 A}{\partial x^2}=0$, and carrier diffusion, $\nabla^2 N=0$, so considering a transverse mean field for each laser (no transversal modes). The simplified model aims to show the concept of EEL bars and to characterize the asymmetric coupling with a large number of lasers. The model describes the forward and backward field of every single laser of the array, namely $A_j^{\pm}$, as monomode lasers in the transverse direction, only coupled to the two neighboring lasers, as:

$$\begin{aligned}
&\frac{\partial A_j^{\pm}}{\partial z}=\left[\left(1-ih\right)N-\left(1+\alpha\right)\right]A_j^{\pm}+m^{-}A_{j-1}^{\pm}+m^{+}A_{j+1}^{\pm}\\
&\frac{\partial N_j}{\partial t}=\gamma\left(-N-\left(N-1\right)\left(\left|A^{+}\right|^2+\left|A^{-}\right|^2\right)+p_0\right),\\
&for\ \ j=-\frac{num-1}{2},\ldots,\frac{num-1}{2}
\end{aligned}\tag{5.2}$$

where, $m^{\pm}$ are complex numbers standing for the coupling parameter from the lasers at positions *j*+1 and *j*-1, respectively, and the spatial and temporal coordinates and all parameters are normalized as in Eq. (5.1). In the simplest case, the system with a non-Hermitian modulation in one dimension may be described by a complex harmonic potential in the form:

$$V(x) = m_m\left[m_r\cos\left(\frac{2\pi}{d}x\right) + im_i\sin\left(\frac{2\pi}{d}x + \Phi\right)\right] = m_m\left[m^+e^{+i\frac{2\pi}{d}x} + m^-e^{-i\frac{2\pi}{d}x}\right] \quad (5.3)$$

where *d* is the distance between lasers and m_r and m_i are the amplitudes of the real and imaginary part of the non-Hermitian potential. Therefore, from Eq. (5.2), we may express the coupling between neighboring lasers as deriving from this simple harmonic complex potential as $m^{\pm} = m_m\left[\left(\frac{m_r \pm m_i}{2}\right)\cos\Phi + im_i\sin\Phi\right]$ being m_m the coupling strength. In this model, we can define different types of coupling between two lasers depending on m_r, m_i, and the phase, Φ. For $\Phi = \pm\,\pi/2$, the coupling is perfectly symmetric, while for $\Phi = 0$, the coupling becomes PT-symmetric. We assume $m_r = m_i = 1$, the PT-symmetry breaking point for simplicity, which entails no restriction but assuming the maximally asymmetric situation.

The system described by Eq. (5.2) is integrated with boundary conditions given by the two mirrors of the Fabry-Perot cavity as for the complete model described by Eq. (5.1). To compare the results of this simplified model to the full model, we find equivalences between parameters comparing behaviors. We first determine the pump threshold p_{th} and the onset of temporal stability, Hopf bifurcation p_H, for a single laser to locate equivalent pump values, see Fig. 5.8 (a). The temporal instability onset corresponds to smooth oscillations of small amplitude, just for a pump interval above the bifurcation, abruptly changing to a pulsed regime with short and bright pulses, starting from almost zero constant output power, as observed with the complete model in Fig. 5.1 (c).

To provide a comparison between the coupling parameters of the simplified model, namely just m_m and Φ, coupling strength and phase shift, with the parameters of the full model, *d* and *s*, distance between lasers and shift between the gain and index profiles, we consider two coupled lasers and map the amplitude of the temporal oscillations of the field amplitude of the laser to which the energy is transferred. Despite the relationship between parameters of

spatial modulation in both models is nontrivial, we can infer a logarithmic relationship between m_m and the laser distance d as far as the coupling strength should decrease exponentially with the laser separation given by (d-w). This relationship is verified by directly comparing the temporal instability in both models shown in Fig. 5.8 (b). The phase shift between the real and imaginary components of the coupling, $\pi/2 - \Phi$ is proportional to the spatial shift s. The other parameters: σ, h, α, γ and p_0 are the same as in Eq. (5.1).

Inspecting the comparison in Fig. 5.8 (b), we conclude that for a symmetric coupling, hence $\Phi = \pi/2$, instabilities arise for values of the coupling strength between lasers, m_m, above 10^{-6} equivalent to no asymmetric shift, $s = 0$ μm and distances d larger than 5.0 μm in the full model. Moreover, for coupling strengths of 10^{-4} and a symmetric coupling, the simplified model shows behaviors analogous to the ones found with the complete model for distances between lasers d = 3.0-3.5 μm, and no asymmetric shift. As expected, the laser is temporally stable at the symmetry breaking point, hence for $\Phi = 0$. However, the transition to stabilization is reached for much larger values of Φ, about $\Phi \approx \pi/3$, which compares the two models, turns out to be analogous to an asymmetric shift about $s \approx 0.3$ μm. Thus, both models agree that it is unnecessary to reach the PT-symmetry breaking point, and just a small shift, s, or, equivalently, a small phase shift ($\pi/2 - \Phi$) is enough to attain stabilization.

Apart from achieving temporal stabilization, the proposed scheme is intended to localize the output beam profile to enable the direct coupling of the light generated from the entire bar directly into an optical fiber. This can eventually avoid any optical elements and minimize losses, as depicted in Fig. 5.7 (a).

To confirm the effect in a laser array, we use both the complete and the simplified model to numerically calculate the spatial redistribution of the generated light, the localization, and the light enhancement at the central laser, for arrays of many lasers, schematically shown in the inset of Fig. 5.8 (c). We consider an array formed by *num* lasers and increase *num* up to 21 in the simplified model —for being a typical number of lasers for an actual laser bar. Using Eq. (5.2), we assume $\Phi = 0$, and consider two different coupling factors corresponding to a strong ($m_m = 10^{-3}$) and weak ($m_m = 10^{-5}$) coupling. For strong coupling, due to the field localization induced by the asymmetric inward coupling, the output power of the central laser increases with the number of lasers, see Fig. 5.8 (c). However, for a small coupling, the output intensity of the center remains almost constant.

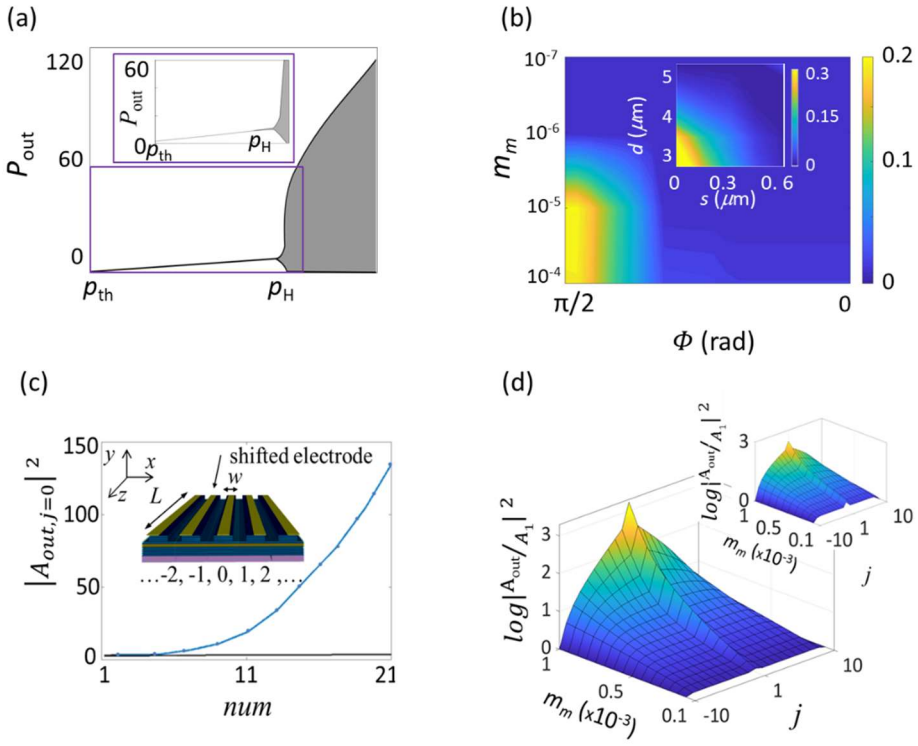

Figure 5.8. (a) LI-curve for a single laser numerically obtained integrating the simplified model, described by Eq. (5.2). The inset shows the LI-curve obtained by the complete model, Eq. (5.1), for comparison. (b) Temporal instability map. The relative amplitude of the temporal oscillations (normalized to the average amplitude) for two coupled lasers obtained with the simplified model, depending on coupling magnitude, m_m, and phase, Φ, between coupling coefficients. The inset compares to the complete model, amplitude of the temporal instability depending on the distance between lasers, d, and the transverse shift coefficient, s. The integration parameters for the simplified model are the same as in Fig. 5.2 and $m_m = 5{\cdot}10^{-3}$, $\Phi = 0$. (c) Intensity of the central laser ($j = 0$) of an array made up of an increasing number of lasers (num), calculated using the simplified model, Eq. (5.2), with inward axisymmetric coupling, for two different coupling strengths: $m_m = 10^{-3}$ (in blue) and $m_m = 10^{-5}$ (in black). The inset displays the proposed scheme for the j = -(num-1)/2…0…(num-1)/2 lasers with shifted electrodes. (d) Emitted intensity distribution in logarithmic scale as a function of the coupling strength, m_m, and the laser position j, for an array made of num = 21 lasers. In the inset: the emitted intensity distribution in log scale of the 21 coupled lasers for $m_m = 2{\cdot}10^{-3}$., equivalent to (d), highlights the laser emission distribution within the array for three particular analog coupling strengths.

Using Eq. (5.2), we assume $\Phi = 0$, and consider two different coupling factors corresponding to a strong ($m_m = 10^{-3}$) and weak ($m_m = 10^{-5}$) coupling. For strong coupling, due to the field localization induced by the asymmetric inward coupling, the output power of the central laser increases with the number of

lasers, see Fig. 5.8 (c). However, for a small coupling, the output intensity of the center remains almost constant.

For a given laser array, the intensity distribution can be evaluated as a function of the coupling parameter, see Fig. 5.8 (d). This figure shows the increase in energy concentration towards the central laser rapidly increasing with the coupling parameter m_m above a given threshold ($m_m = 10^{-3}$). The peak at the central laser is due to the addition of fields coming from both sides. While these results prove the working principle of the proposal, we note that a more realistic approach intended to design an experiment should certainly include diffraction and inhomogeneous losses due to the fiber coupling, reducing the field localization.

Finally, to provide a deeper analytic insight, we consider a stationary and punctual model, i.e. assuming null spatial and temporal derivatives in Eq. (5.2) and just with inward axisymmetric coupling. The amplitude solution for the uncoupled lasers at each edge coincides with the standing alone laser: $|A|^2 = \dfrac{p_0 - (1+\alpha)}{\alpha}$, from which, we induce the amplitudes of all lasers of the array, from the edges to the central laser, resulting in:

$$\begin{aligned} &\left[(1-ih)\frac{p_0 + A_j^2}{1+A_j^2} - (1+\alpha) \right] A_j + m_j^- A_{j+1} + m_j^+ A_{j-1} = 0 \,, \\ &for \;\; j = -\frac{num-1}{2}, \ldots, \frac{num-1}{2} \\ &m_{-j}^- = m_j^+ = 0, \; m_j^- = m_{-j}^+ = m_m \text{ for } j \geq 0. \end{aligned} \tag{5.4}$$

This simple analytic estimation of the central laser intensity and energy distribution on the array shows a good agreement with the numerical integration of the forward and backward fields in Eq. (5.2) for the *num* asymmetrically coupled cavities. Despite the simplicity of the punctual model, comparing Fig. 5.8 (d) with the inset, we observe an analogous trend, yet in the punctual model, the pump is assumed to be just above the lasing threshold. Both results show a similar dependence on the number of lasers and coupling strength, and for the particular case of *num* = 21, both energy distribution patterns strongly change their profiles for the same critical value of m_m, about $m_m = 10^{-3}$.

From Eq. (5.4), we can induce that for a weak coupling strength m_m, the gain enhancement in laser j given by the asymmetric coupling from the neighboring laser j+1 (or j-1) is small, and the laser losses α limits the field amplitude A_j remaining constant along the array, from the edge lasers to the central laser, with an intensity value about the standing alone laser $A_j^2 \approx \frac{p_0 - (1+\alpha)}{\alpha}$. In contrast, for large m_m values, the asymmetric coupling strongly enhances gain, and the cascade effect from edges to the central laser is the cause of the energy localization with a sharp profile. Thus, considering amplitude values much larger than the pump value, the multiplying factor becomes $\frac{A_{\pm|j|}}{A_{\pm|j+1|}} = \frac{m_m}{\sigma\alpha}$ from which we can infer the threshold coupling strength for a sharp profile in the energy distribution, $m_{mth} = \sigma\alpha = 10^{-3}$ for the considered parameters, in good agreement with numeric simulations.

5.4 Conclusions

In summary, we present a physical mechanism for the temporal stabilization and localization of the emission of a coupled array of EELs or an EEL bar. The scheme is based on a non-Hermitian coupling between neighboring lasers with a global mirror-symmetric geometry. While the monomode emission of a single laser is assured by reducing its width, spatio-temporal instabilities may still arise from the coupling between lasers in an array. Such temporal instabilities are molded by a non-Hermitian coupling that may be simply introduced by a lateral shift between the pump and index profile, technically by a spatial shift between the individual laser stripe and corresponding electrode. While temporally stabilizing the emission, such asymmetric coupling also redistributes and localizes energy close to the central symmetry axis.

The proposed stabilization scheme is analyzed by a complete spatio-temporal model, including transverse and longitudinal spatial degrees of freedom and the temporal evolution of the electric fields and carriers. Furthermore, we perform a comprehensive numerical analysis in terms of the design parameters, namely the distance between lasers and non-Hermitian shift observing regimes of simultaneous temporal stabilizations and light localization. In turn, the proposal's validity is also demonstrated for an array with a large number of

lasers using a simplified model where the coupling between neighboring laser cavities accounts for the transverse space.

A non-Hermitian architecture for stable EEL bars is demonstrated, leading to a brighter output beam, yet the field concentration is expected to facilitate a direct coupling of these semiconductor laser arrays to an optical fiber.

Publication XI

J. M. Pardell, R.Herrero, M. Botey, and K. Staliunas, *"Non-Hermitian arrangement for stable semiconductor laser,"* Optics Express **29**(15), 23997-24009 (2021).

Research Article | Vol. 29, No. 15 / 19 July 2021 / Optics Express 23997

Optics EXPRESS

Non-Hermitian arrangement for stable semiconductor laser arrays

J. MEDINA PARDELL,[1,*] R. HERRERO,[1] M. BOTEY,[1] AND K. STALIUNAS[1,2]

[1] *Departament de Física, Universitat Politècnica de Catalunya (UPC), Colom 11, E-08222 Terrassa, Barcelona, Catalonia, Spain*
[2] *Institució Catalana de Recerca i Estudis Avançats (ICREA), Passeig Lluís Companys 23, E-08010 Barcelona, Catalonia, Spain*
[*] *judith.medina@upc.edu*

Abstract: We propose and explore a physical mechanism for the stabilization of the complex spatiotemporal dynamics in arrays (bars) of broad area laser diodes taking advantage of the symmetry breaking in non-Hermitian potentials. We show that such stabilization can be achieved by specific pump and index profiles leading to a PT-symmetric coupling between nearest neighboring lasers within the semiconductor bar. A numerical analysis is performed using a complete (2 + 1)-dimensional space-temporal model, including transverse and longitudinal spatial degrees of freedom and temporal evolution of the electric field and carriers. We show regimes of temporal stabilization and light emission spatial redistribution and enhancement. We also consider a simplified (1 + 1)-dimensional model for an array of lasers holding the proposed non-Hermitian coupling with a global axisymmetric geometry. We numerically demonstrate a two-fold benefit: the control over the temporal dynamics over the EELs bar and the field concentration on the central lasers leading to a brighter output beam, facilitating a direct coupling to an optical fiber.

1. Introduction

Diode lasers systems, either in the form of a single Edge-Emitting Laser (EEL), in the form of arrays of lasers (lasers bars), or as stacks of EEL bars, are replacing other lasers sources due to their compactness, affordable prices and high performance. However, they present a major drawback, the laser spatiotemporal instability and divergence which, particularly, prevents them to efficiently couple to optical fibers. Spatiotemporal complex dynamics is commonly observed in spatially extended, dissipative systems which are driven by an external pump. Board area diode lasers are no exception and are plagued by self-focusing filamentation instabilities and complex dynamical behaviors [1,2,3]. Moreover, in EELs bars, the coupling between neighboring EELs contributes to increase such spatiotemporal instabilities [4,5,6,7]. The consequence is the onset of chaotic and turbulent regimes produced by spatial and temporal instabilities such as the modulation instability and Hopf bifurcations. Yet, different proposals to reduce or to eliminate these instabilities for a single laser relay on external cavities or elements, therefore compromising the compactness of the laser [8,9,10]; this is also the case for bars of EEL lasers [11,12,13,14]. Besides, a complex optical setup made up of: a fast-axis collimator, a slow-axis collimator and a focusing lens, is commonly used to improve efficient coupling into multimode fibers. Usually, the intrinsic turbulent behavior enlarges the smallest possible focal point and limits the coupling to thin monomode fibers [15]. Possible approaches on the regularization of a single semiconductor laser are based on intracavity filtering [16,17] or on spatial gain profile to mitigate semiconductor lasers instabilities by the introduction of intrinsic complex modulations within the laser [18,19,20]. But obtaining a stable emission from EELs bars remains a longstanding open question, and there is a need for a compact stabilization scheme.

#425860 https://doi.org/10.1364/OE.425860
Journal © 2021 Received 14 Apr 2021; revised 9 Jun 2021; accepted 28 Jun 2021; published 14 Jul 2021

Optics EXPRESS

Recently, the interplay between gain and index modulation has emerged as a fruitful new research area in photonics. Initially introduced as a curiosity in quantum mechanics [21], parity-time (PT-) symmetry, found experimental realizations in the field of photonics in artificial materials with spatial distributions of real and complex permittivities, showing the ability of molding the flow of light [22,23,24,25,26]. The attentions to those systems that while being non-conservative could still hold real energy eigenvalues, derives from the unusual, even counter intuitive properties they hold arising from an asymmetric coupling of modes. Beyond the particular class of open non-conservative systems holding PT-symmetry however, there is a larger class of non-conservative as non-Hermitian Hamiltonians [27]. Indeed complex Non-Hermitian photonics has led to technologically accessible novel effects, from transparency and invisibility [28,29] to light transport [30] including various applications in laser science [31,32]. In particular, the new concepts of non-Hermitian photonics have successfully been applied to the control of the dynamics of broad semiconductor lasers [33,34], and arrays of vertical emitting semiconductor lasers or a ring array of semiconductor lasers [35,36].

Our proposal is intended to obtain a stable emission from an array of EELs and the improvement of its beam quality and energy distribution within the laser array. Altogether allows the direct coupling to fiber or optical guide without any optical component that should strongly enhance the coupling efficiency. The light generated in every single semiconductor laser is expected to be spatially redistributed and temporally stabilized via non-Hermitian coupling between neighboring lasers induced by a particular gain (pump) and index modulation (stripes) of the structure. The system is described by a complete $(2+1)$-dimensional space-temporal model, including transverse and longitudinal spatial directions and temporal evolution of the electric field and carriers.

We first identify the onset of spatiotemporal instabilities for a single laser source, the regime of temporally stable and monomode emission severely restricts the power of the laser source. However, splitting a broad EEL source in an array of stable, thinner lasers with stable emission parameters, is not a solution, since new temporal and synchronization instabilities arise from the coupling between neighboring lasers leading again to irregular spatiotemporal behaviors. Thus, we propose a non-Hermitian asymmetric coupling between EELs within the array for stabilization and redistribution of the light emission. This emission improvement is first demonstrated for the simple two coupled laser system. We determine the stabilization performance as a function of the shift between the pumped region and laser stripes and the distance between the two lasers. Next, we analyze a system formed by three lasers holding a global mirror symmetry to induce an inward coupling in the laser array. In the following, a simplified $(1+1)$-dimensional model is used to extend the study to a full EEL bar formed by an array of many lasers. The simulations show both temporal stabilization and simultaneous spatial redistribution, i.e. localization, of the generated light.

2. Model for semiconductor laser arrays

In order to model the spatial redistribution and temporal stabilization of coupled EEL sources, we use a well-established model including the spatiotemporal evolution of the electromagnetic field and carrier density inside the cavity [20]. EELs are usually described either by stationary models [37] or dynamical models of the mean field [38]. Here, the complete dynamical model is used for the forward and backward fields propagating within the cavity and the carrier density. It was recently used to demonstrate spatial filtering of broad EEL sources [17]. Since the round-trip time of the cavity (on the order of ps) is small compared to the carrier's relaxation time (on the order of ns), the temporal evolution of the field in one roundtrip may be calculated by its propagation along the cavity assuming constant carriers. Applying the slowly varying envelope approximation, the forward and backward envelopes of the electric field, $A^{\pm}$ are integrated along the EEL followed by the second step, the temporal integration of carriers considering a constant

Optics EXPRESS

field. We neglect the frequency dependence of material gain, spatial hole burning of carriers, and heating-induced changes of model parameters since we assume we do not reach high powers [39,40]. Overall, this results in the following non-linear system of three coupled equations:

$$\begin{aligned} \pm \frac{\partial A^{\pm}}{\partial z} &= \frac{i}{2k_0 n}\frac{\partial^2 A^{\pm}}{\partial x^2} + \sigma[(1-ih)N - (1+\alpha)]A^{\pm} + i\Delta n(x)k_0 A^{\pm} \\ \frac{\partial N}{\partial t} &= \gamma(-N - (N-1)(|A^{+}|^2 + |A^{-}|^2)^2 + p_0 + \Delta p(x) + D\nabla^2 N) \end{aligned} \tag{1}$$

where k_0 is the wavevector, n is the effective refractive index, $\boldsymbol{\sigma}$ is a parameter inversely proportional to the light matter interaction length, h is the Henry factor or linewidth enhancement factor of the semiconductor, α corresponds to losses, p_0 is the pump, D is the carrier diffusion coefficient and γ is the inverse of carriers' relaxation time, τ_{nr}. In our calculations the transverse and longitudinal spatial coordinates are in units of the wavelength, time is normalized to the roundtrip time; N is normalized to N_0 (the carrier's density to achieve transparency) and the electric field envelope is normalized to $\frac{a\tau_{nr}}{\hbar\omega}$ being a the gain parameter, ω the angular frequency of light. Polarization of the material is eliminated in Eq. (1) as the semiconductor laser is considered a class B laser and the fine longitudinal interference between the forward and backward fields, considered to be blurred by the carrier diffusion, is disregarded. Finally, the transverse modulations of the refractive index $\Delta n(x)$ account for the individual laser stripes; and the pump, $\Delta p(x\text{-}s)$, where s is a spatial shift the spatial profile of the electrodes. Both modulations, $\Delta n(x)$ and $\Delta p(x\text{-}s)$, induce the real and imaginary parts of the non-Hermitian potential, which, properly designed, may lead to an asymmetric field coupling. See Fig. 1(a) for a schematic representation of the laser architecture. In order to avoid discontinuities in the derivatives of these modulations, the two spatial transverse profiles are mathematically described as consecutive sharp sigmoids.

In the proposed scheme, the two profiles, $\Delta n(x)$ and $\Delta p(x)$, can be slightly spatially shifted a distance s, one with respect to another, and it is precisely this interplay between index and gain profiles that is expected to induce a non-Hermitian potential and asymmetric coupling between neighboring lasers. The boundary conditions are straightforwardly determined by the Fabry-Perot cavity mirrors located at $z=0$ and $z=L$ are $A^{+}(z=0) = r_0 A^{-}(z=0)$ and $A^{-}(z=L) = r_L A^{+}(z=L)$, where L is the length of the laser and $r_{0/L}$ are the corresponding reflection of the edge mirrors at $z=0/L$, respectively.

First, we numerically study the spatiotemporal behavior of a single EEL source through the system model in Eq. (1) to determine its dynamics for different working conditions. As it is well known, decreasing the laser width acts as a mode selection mechanism when light is confined and a the broad and strongly multimode semiconductor emission turns into a monomode emission regime. However, to achieve a brighter source it is not enough to split a broad EEL source into an array of spatially stable thin EELs by patterning longitudinal separation slits between them. It is also necessary to engineer the coupling between lasers within the array to obtain stability and improve the quality of the emission, see Fig. 1(a). Numerical simulations supporting this idea are provided in Fig. 1(b), showing the total emitted output power of a single EEL for widths, w, ranging from 2.5 µm to 50 µm, and analyzing the field profile within the laser while decreasing width seeking for the onset of the monomode emission. The maximum width for a monomode emission determined by $w_{\max} = \lambda/\sqrt{2n\Delta n}$ (corresponding to 4 µm for the general operational parameters chosen in Fig. 1) is in good agreement with the integrated beam profiles. In turn, we calculate the beam quality factor, M^2 as the ratio between the Beam Parameter Product (BPP) of a real beam and a Gaussian beam, which can be numerically evaluated as: $M^2 = \frac{BPP_{actual\ beam}}{BPP_{Gaussian\ beam}} = \frac{\pi w\theta}{\lambda}$, where w is the near-field width, and where the divergence, θ, is obtained from the far field, provided in the inset of Fig. 1(b). Indeed, the transvers cuts for the laser profiles provided in Fig. 1(b), also evidence how M^2 strongly increases with the laser's width as the laser becomes more multimode and inhomogeneous, see However, while a short

Optics EXPRESS

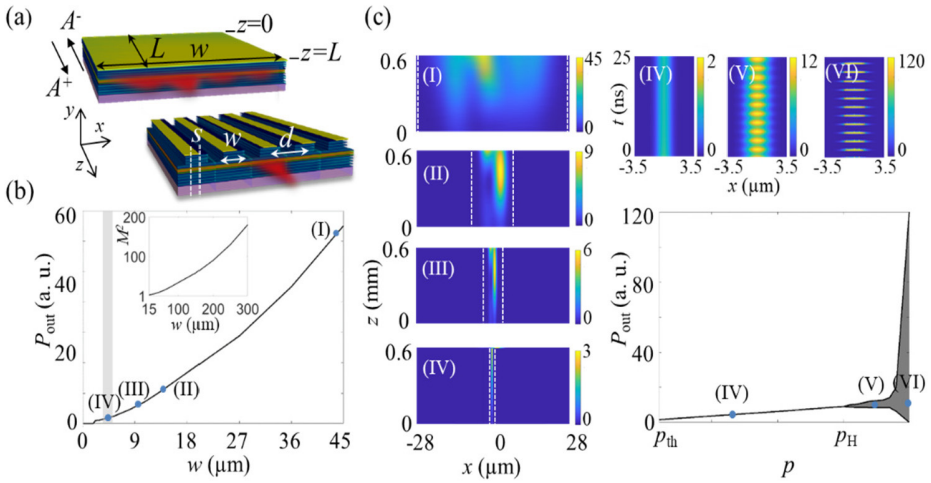

Fig. 1. (a) Scheme of a broad single EEL where the index and pump profiles coincide with no spatial shift ($s = 0\mu m$), where w is the laser width and L the length, and scheme of a laser array made of single lasers with $s \neq 0$, separated a distance d. (b) Calculated output of the EEL as a function of the laser width, as obtained from Eq. (1); inset: M^2 dependence on the laser width for a given pump $p_0 = 2.5$. The lateral subplots depict the spatial intensity distributions for different widths of the pump: I 50 μm, II 12.5μm, III 7.5μm, IV 2.5μm determined by dashed lines on each plot; grey area: analytical range of monomode emission. (c) Temporal evolution of the transverse intensity profile within the laser for $w = 2.5$ μm and different pumps, normalized to the emission threshold p_{th}: IV $p = 1.1\ p_{th}$, V $p = 1.8\ p_{th}$, VI $p = 1.9\ p_{th}$, and numerical Light-Intensity output power, LI-curve, as a function of the pump; p_H indicates the onset of the instability. The integration parameters are: $L = 500$, $\alpha = 0.1$, $h = 2.0$, $\sigma = 0.06$, $D = 0.03$ and $\gamma = 0.005$, and the units in the graphs correspond to $\lambda = 1\mu m$, with $n_0 = 3.5$ and $\Delta n = 0.06$.

width in a semiconductor laser indeed acts as a transverse mode selection mechanism it does not warrant its temporal stability. This can be observed in Fig. 1(c), where the temporal stability of a monomode laser —namely, $w = 2.5$ μm— is scanned as a function of the pump. The results show a Hopf bifurcation arising at a particular pump, referred as the Hopf pump, p_H, and for pump values above this threshold the laser becomes temporally unstable as it is evident comparing the temporal evolution of the spatial distribution transverse profile for two given pump values below and above p_H, sharing however monomode spatial distribution along the laser. The smooth oscillations observed just after the Hopf bifurcation present periods about 20 roundtrips and are only visible in the small pump interval shown in the figure, while for larger pump values sharp peaks with an almost zero background appear. Scanning the pump upwards, pulses rapidly increase in amplitude while becoming shorter, with a time duration of few roundtrips, and reducing their frequency.

3. Symmetric and asymmetric coupling

Once the main dynamics and parameters of a single laser are determined we proceed to analyze the effect of the coupling between lasers on the dynamics. Such coupling depends on the distance between neighboring lasers and can be further engineered by introducing a displacement between the laser profile and the pump, as schematically shown in Fig. 1(a). We first analyze the coupling between two identical lasers with the same intrinsic parameters and where the index and the pump profiles perfectly coincide, and are, therefore, symmetrically coupled. While the two standing alone lasers may have a spatially and temporally stable emission, as the distance between

Optics EXPRESS

them decreases —the coupling strength increases— and keeping the rest of parameters, both lasers become temporally unstable. Spatial asymmetries are evident in every snapshot of the numerically calculated intensity distribution of two close EEL sources, see Fig. 2(a). Besides, the temporal evolution of the transverse profile of the intensity at any position of the cavity length is aperiodic, see Fig. 2(b). Next, we slightly shift the index profile of both lasers with respect to the gain profiles to induce a mirror-symmetric coupling. As expected, the light generated in one laser is partially transferred to the other one, see Fig. 2(c). As an important consequence, when the energy is redistributed due to the asymmetric coupling, both lasers become temporally stable, as shown in the temporal evolution of the intensity transverse profile in Fig. 2(d). This temporal stabilization tendency is in agreement with the general behavior of coupled nonlinear oscillators generally showing less complex dynamics for unidirectional than for bidirectional couplings.

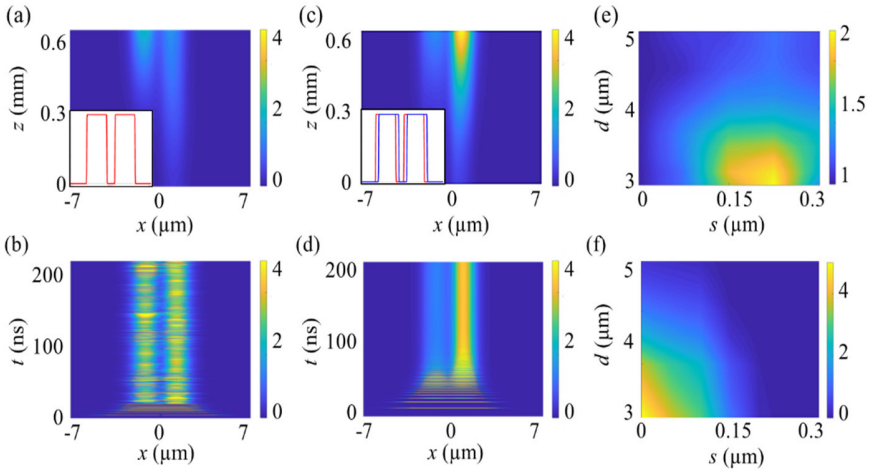

Fig. 2. (a)/(c) Snapshots of the spatial intensity distribution after sufficient integration time for two symmetrically/asymmetrically coupled lasers, and (b)/(d) temporal evolution of the intensity at $z = L$ for two symmetrically/asymmetrically coupled lasers with $w = 2.5\mu$m, separated a center-to-center distance $d = 3\,\mu$m and for $s = 0.25\,\mu$m. Insets show the transverse pump profile Δp (red curve) and the index profile Δn (blue curve), and they coincide in (a). (e) Intensity enhancement factor of the amplified laser depending on the distance between lasers, d, and spatial shift, s. (f) Temporal instability map. Relative amplitude of the temporal oscillations (normalized to the average amplitude) All the integration parameters are the same as in Fig. 1, and $p_0 = 2.5$.

The performance of the proposed asymmetric coupling is assessed by the asymmetric energy enhancement and temporal stability of the attained regimes. We calculate the enhancement as the relative intensity of the laser to which the energy is accumulated, i.e. as the ratio of the temporally averaged intensity of the enhanced laser, for $s \neq 0$, versus the unshifted case, $s = 0$. We explore the parameter space of the distance between lasers, d, and asymmetry shift parameter, s (spatial shift between the pump and the refractive index profiles) for a fixed value of the pump. The results are summarized in Fig. 2(e). While a larger enhancement could be expected by increasing the shift parameter s. However, we observe that the emission decreases for a maximum around a given shift value, namely $s \approx 0.25\,\mu$m. This decrease may be attributed to the asymmetric configuration of both lasers which also induces an asymmetric leaking of energy opposite to the direction of the other laser. Such leaked energy is therefore lost, and the net gain for the whole system is reduced; being the largest relative intensity of the enhanced factor around about 2. Moreover, such enhancement increases for a smaller distance, d. In addition, the temporal stability of the emission may be evaluated by mapping the amplitude of the temporal oscillations of the enhanced laser also in the distance-shift, (d,s), parameter space. Temporal instabilities arise

Optics EXPRESS

for small d and s values, i.e. when the distance between lasers or coupling asymmetry decrease. For center-to-center distances close to the laser width the emission is found to be unstable for all values of s. On the contrary, stability is found either increasing the coupling asymmetry for a given laser distance, as also, trivially, at larger distances between lasers. Interestingly, inspecting Figs. 2(e) and 2(f), we observe that there is a range of parameters around the maximum relative intensity region which coincides with a temporally stable behavior.

As above mentioned, while the energy is enhanced in one laser, some energy is in turn leaked due to the asymmetric configuration, asymmetrically coupled out from the laser. We further analyze this effect considering a single laser. We observe that around $s = 0.35$ µm all the energy created in the laser is lost, see Fig. 3(a). A physical insight to this effect is found calculating the transverse spatial tilt of the phase of the electric field within the laser that indicates a transverse shift of light propagating along the laser and out from the laser stripe, see Fig. 3(b). As it may be expected, such phase if completely symmetric for s=0, while the averaged phase slope inside the laser, directly increases with the asymmetry parameter s, see Fig. 3(c), indicating a linear increase of the transverse transfer of energy with s.

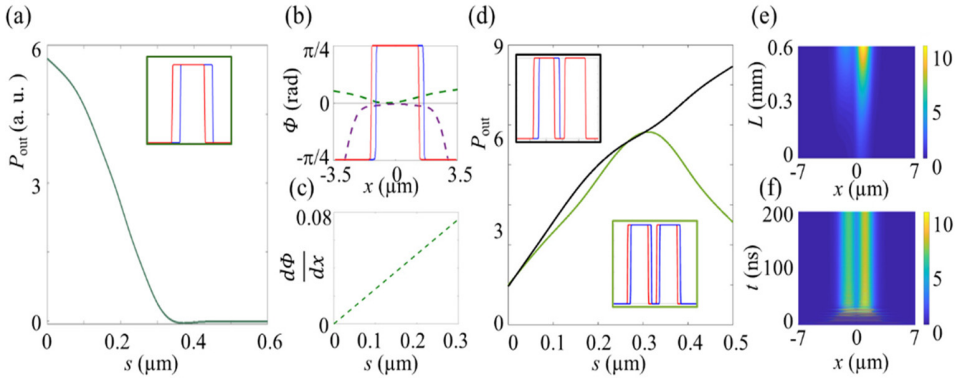

Fig. 3. (a) Loss of output power for one laser when s increases, being s the transverse shift between Δn and Δp, in blue and red in the inset. (b) Field phase for $s = 0$ µm (dashed purple curve) and for $s = 0.15$ µm (dashed green curve). The blue and red solid lines represent Δn and Δp for the second case. (c) Field phase slope at the central point of the laser as a function of s. (d) Comparison of the output power for two coupled lasers with asymmetric lateral coupling with single (black) and double transverse shift (green) as a function of s. (e) Snapshot of the spatial intensity distribution after sufficient integration time and (f) temporal evolution of the intensity for two coupled lasers with single transverse shift corresponding to the black curve for $s = 0.4$ µm. All the integration parameters are the same as in Fig. 2.

Therefore, the effect is optimized by considering a single transverse shift, i.e. no shift for the laser to which the energy is transferred. We compare this last configuration with the double transverse shift configuration inspected in Fig. 2 for a distance of 3 µm between the two lasers, see Fig. 3(d). The double shifted configuration achieves a maximum of output power for an s value about 0.25 µm and decrease due to the energy leakage while the single shifted case keeps increasing with s. Temporal instabilities also disappear for the single shift case increasing s parameter and the amplitude of the temporal oscillations shows a similar (d, s) dependence of Fig. 2(f). The spatial intensity distribution and the temporal evolution for the single shift configuration are provided in Figs. 3(e) and 3(f) showing more than twice the emission of the double shifted scheme of Fig. 2(c).

Optics EXPRESS

4. Axisymmetric inward coupling of EELs

As observed, the asymmetric coupling leads to simultaneous enhancement and temporal stabilization of the emitted field and the effect is optimized when the enhanced laser has no asymmetric shift. Therefore, the next step is considering a simple array architecture formed by three coupled lasers with asymmetric coupling but with a central symmetry axis [33]. That is to say, two symmetric lasers holding asymmetric shift between gain and index profiles and a central one with no shift. For such configuration, the coupling is expected to increase as the distance decreases eventually also reaching a temporally stable regime as light is localized inwards.

The numerical results for the three coupled lasers are summarized on Fig. 4. It can be observed that when symmetrically coupled, all three lasers are temporally unstable as intensity switches from one laser to another see Figs. 4(a) and 4(b). On the contrary, as the non-Hermitian inward potential is introduced, by means of the inward asymmetric shift of the index profile versus the gain profile, the generated light tends towards the central laser and all lasers become stable, see Figs. 4(c) and 4(d). We note that in this scenario, the fulfilled redistribution and spatial stabilization leads to enhanced intensities as compared with the two-laser case.

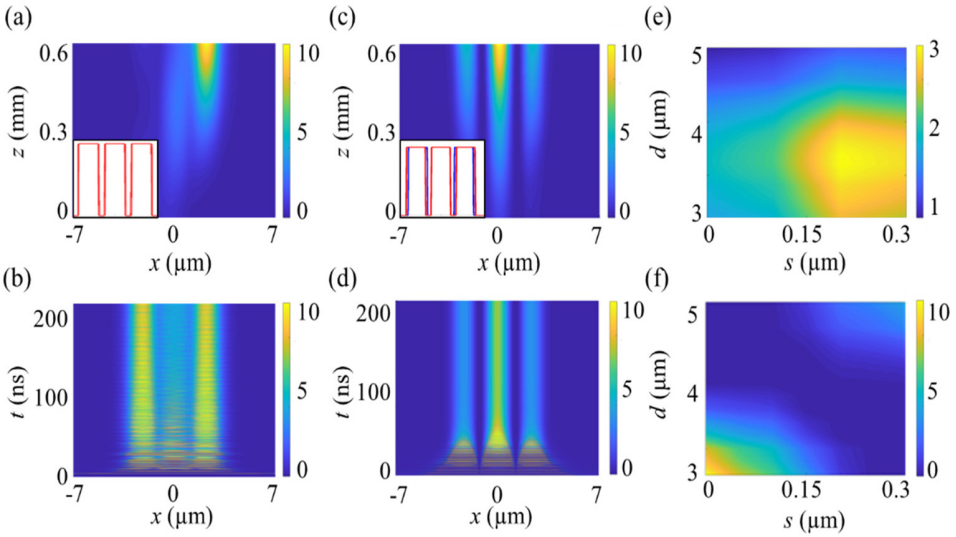

Fig. 4. (a)/(c) Snapshots of the spatial intensity distribution of the intensity for a triad of lasers with symmetric/inward-axisymmetric coupling after sufficient integration time and (b)/(d) temporal evolution of the intensity at $z = L$ for three lasers with symmetric/inward-axisymmetric coupling with $w = 2.5\,\mu m$, separated a center-to-center distance $d = 3.0\,\mu m$ and for $s = 0.25\,\mu m$. Insets show the transverse pump profile Δp (red curve) and the index profile Δn (blue curve), and they coincide in (a). (e) Relative intensity and (f) amplitude of the temporal oscillations depending on the distance between lasers, d, and spatial shift, s. All the integration parameters are the same as in Fig. 2.

The performance of the proposed mirror symmetric lasers triad is evaluated by the relative intensity of the central laser, i.e. intensity of the enhanced laser, for $s \neq 0$, versus the unshifted case, $s = 0$. Comparing Fig. 4(e) and Fig. 3(e), we observe the maximum intensity for a somewhat larger value of d. Besides, a larger enhancement ratio is reached, as energy is coupled from the two neighboring lasers. The temporal stability of the emission is here evaluated by mapping the temporal oscillations of the central laser also in the distance-shift parameter space, (d, s), for a fixed pump value. The results, summarized in Fig. 4(f), show a range of maximum energy localization, for small distances around 3.5 μm, and shift parameter $0.15 \leq s \leq 0.25$. Precisely these set of parameters coincides with temporal stability, assessed by mapping the temporal

Optics EXPRESS

oscillations of the central laser. Inspecting Figs. 4(e) and 4(f), we assert that temporal stability is achieved for a simultaneous light localization. In this case, temporal stability reappears at larger distances for significant values of the shift parameter.

5. EEL array with axisymmetric inward coupling

The results presented in the previous section provide a proof of principle along with a comprehensive understanding of the asymmetric coupling of the proposed scheme. Next such results are extended to an EEL array or an EEL bar composed of many lasers.

The proposed scheme is depicted in Fig. 5(c), the array is divided into two half-spaces with symmetric spatial shift between gain and index transverse profiles, arranged such that the index lays closer to the symmetry axis and the central laser holding no displacement. Thus, we expect light generated within the array to be directed inwards due to the asymmetric coupling.

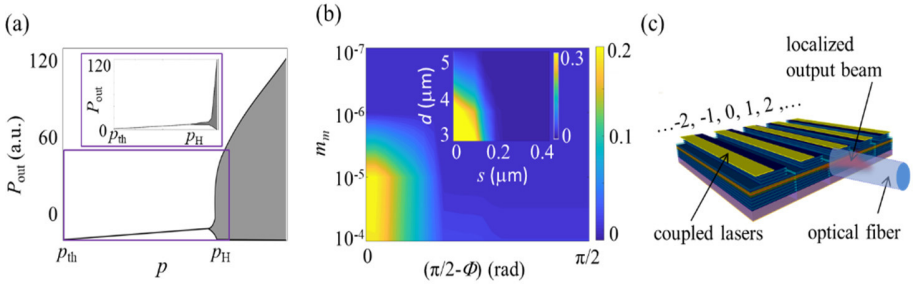

Fig. 5. (a) LI-curve for a single laser numerically obtained integrating the simplified model, described by Eq. (2). The inset shows the LI-curve obtained by the complete model, Eq. (1), for comparison. (b) Temporal instability map. Relative amplitude of the temporal oscillations (normalized to the average amplitude) for two coupled lasers obtained with the simplified model, depending on coupling magnitude, m_m, and phase shift, $\pi/2$-Φ, between coupling coefficients. The inset provides a comparison to the complete model, amplitude of the temporal instability depending on the transverse shift coefficient, s. All the integration parameters are the same as in Fig. 2. (c) Scheme of the array of coupled lasers directly coupled to an optical fiber. The integration parameters for the simplified model are the same as in Fig. 2. with $m_m = 5{\cdot}10^{-3}$ and $\Phi = 0$.

We develop a simplified model, accounting for the longitudinal propagation, temporal evolution and coupling between lasers but disregarding diffraction, $\frac{\partial^2 A}{\partial x^2}$, and carriers diffusion, $\nabla^2 N = 0$, so considering a transverse mean field for each laser (no transversal modes). The simplified model is aimed at showing the concept on EEL bars, and to characterize the asymmetric coupling with a large number of lasers. The model describes the forward and backward field of every single laser of the array, namely $A_j^{\pm}$, as monomode lasers in the transverse direction, only coupled to the two neighboring lasers, as:

$$\begin{aligned} \frac{\partial A_j^{\pm}}{\partial z} &= \sigma[(1-ih)N-(1+\alpha)]A_j^{\pm}+m^{-}A_{j-1}^{\pm}+m^{+}A_{j+1}^{\pm} \\ \frac{\partial N_j}{\partial t} &= \gamma(-N-(N-1)(|A^{+}|^2+|A^{-}|^2)+p_0)\ ,\ for\ \ j=-\frac{num-1}{2}\ ,\ \ldots,\ \frac{num-1}{2} \end{aligned} \tag{2}$$

where, $m^{+/-}$ are complex numbers standing for the coupling parameter from the lasers at positions j+1 and j-1, respectively, and the spatial and temporal coordinates and all parameters are normalized as in Eq. (1). In the simplest case, a periodic non-Hermitic potential in one-dimension may be approximated by a complex harmonic form: $V(x) = m_m\left[m_r\cos\left(\frac{2\pi}{d}x\right)+im_i\sin\left(\frac{2\pi}{d}x+\Phi\right)\right] =$

Optics EXPRESS

$m_m \left[m^+ e^{+i\frac{2\pi}{d}x} + m^- e^{-i\frac{2\pi}{d}x} \right]$, where d is the distance between lasers and m_r and m_i the amplitudes of the real and imaginary part of the non-Hermitian potential. Therefore, from Eq. (2) we may express the coupling between neighboring laser as deriving from this simple harmonic complex potential as $m^{\pm} = m_m \left[\left(\frac{m_r \pm m_i}{2} \right) \cos\Phi + i m_i \sin\Phi \right]$ being m_m the coupling strength. In this model we can define different types of coupling between two lasers depending on the values of m_r, m_i and the phase, Φ. For $\Phi = \pm \pi/2$, the coupling is perfectly symmetric while for $\Phi = 0$, the coupling becomes PT-symmetric. In turn, and for simplicity we assume $m_r = m_i = 1$, the PT-symmetry breaking point, which entails no restriction but assuming the maximally asymmetric situation. Despite the relationship between parameters of spatial modulation in both models is nontrivial, we can infer a logarithmic relationship between m_m and the laser distance d as far as the coupling strength should decrease exponentially with the laser separation given by (d-w). This relationship is verified by direct comparison of the temporal instability in both models shown in Fig. 5(b). The phase shift between the real and imaginary components of the coupling, $\pi/2$-Φ is proportional to the spatial shift s. The other parameters:σ, h, α, γ and p_0 are the same as in Eq. (1).

The system of Eq. (2) is integrated with boundary conditions given by the two mirrors of the Fabry-Perot cavity as for the complete model described by Eq. (1). In order to compare the results of this simplified model to the complete model, we find equivalences between parameters comparing behaviors. We first determine the pump threshold p_{th} and the onset of temporal instability, Hopf bifurcation p_H, for a single laser to locate equivalent pump values, see Fig. 5(a). The temporal instability onset corresponds to smooth oscillations of small amplitude, just for a pump interval above the bifurcation, abruptly changing to a pulsed regime with short and bright pulses, starting from almost zero constant output power, as observed with the complete model in Fig. 1(c). In order to provide a comparison between the coupling parameters of the simplified model, namely just m_m and Φ, coupling strength and phase shift, with the parameters of the full model, d and s, distance between lasers and shift between the gain and index profiles, we consider two coupled lasers and map the amplitude of the temporal oscillations of the field amplitude of the laser to which the energy is transferred. Inspecting the comparison in Fig. 5(b) we conclude that for a symmetric coupling, hence $\Phi = \pi/2$, instabilities arise for values of the coupling strength between lasers, m_m, above 10^{-6} equivalent to no asymmetric shift, $s = 0$ and distances d larger than 5.0 µm in the full model. Moreover, for coupling strengths of 10^{-4} and a symmetric coupling the simplified model shows behaviors analogous to a distance between lasers $d = 3.0$-3.5 µm, and no asymmetric shift. As expected, the laser is temporally stable at the symmetry breaking point, hence for $\Phi = 0$, although the transition to stabilization is reached for much larger values of Φ, about $\Phi \approx \pi/3$, which comparing the two models, turns out to be analogous to an asymmetric shift about $s \approx 0.3$ µm. Thus, both models agree that it is not necessary to reach totally asymmetric unidirectional couplings, but just a small shift, s, or, equivalently, a small phase shift ($\pi/2$ - Φ) to attain stabilization. Apart from achieving temporal stabilization the proposed scheme is intended to localize the output beam profile to enable the direct coupling of the light generated from the entire bar directly into an optical fiber, eventually avoiding any optical elements and minimizing losses as depicted in Fig. 5(c).

To confirm the effect in a laser array we use both, the complete and the simplified model to numerically calculate the spatial redistribution of the generated light, the localization and the light enhancement at the central laser, for arrays of many lasers, schematically shown in the inset of Fig. 6(b). We use Eq. (1) to evaluate the decrease of the beam quality factor M^2, for arrays up to 13 lasers, see Fig. 6(a), due to the stripping (black line) and the non-Hermitian potential effect (blue line) with respect a single broad laser with the same pumped area (orange line). We consider an array formed by *num* lasers and increase *num* up to 21 in the simplified model, for being a sensible number of lasers for an actual laser bar. Using Eq. (2), we assume $\Phi = 0$, and consider two different coupling factors corresponding to a strong ($m_m = 10^{-3}$) and weak ($m_m = 10^{-5}$) coupling. For a strong coupling, as a consequence of the field localization

Optics EXPRESS

induced by the asymmetric inward coupling, the output power of the central laser increases with the number of lasers, see Fig. 6(a). Yet, for a small coupling the output intensity of the central remains almost constant. For a given laser array the intensity distribution, at each laser position, can be evaluated as a function of the coupling parameter, see Fig. 6(b) showing the increase of the energy concentration towards the central laser rapidly increasing with the coupling parameter m_m above a given threshold ($m_m = 10^{-3}$). The peak at the central laser is due to the addition of fields coming from both sides. While these results proof the working principle of the proposal we note that a more realistic approach indented to design an experiment should certainly include diffraction and inhomogeneous losses reducing the field localization.

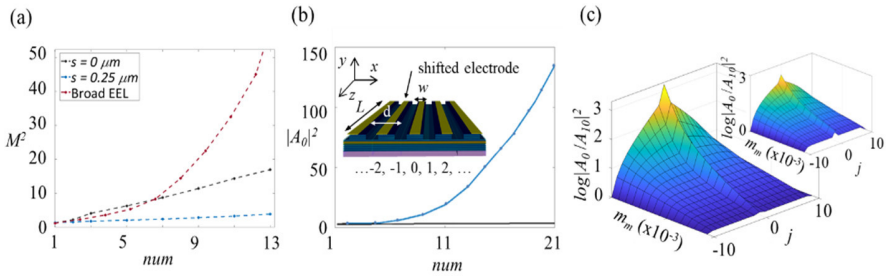

Fig. 6. (a) M^2 value dependence on the number of lasers for a symmetric array of lasers ($s = 0$ μm, black), a non-Hermitian array of lasers ($s = 0.25$ μm, blue) and a single broad EEL with equivalent pumped area (red). (b) Intensity of the central laser, $|A_0|^2$, for arrays of *num* lasers with inward axisymmetric coupling, for the simplified model, Eq. (2), and for two different coupling strengths: $m_m = 10^{-3}$ (blue) and for $m_m = 10^{-5}$ (black). The inset displays the proposed scheme for *num* lasers, j = -(*num*-1)/2. . . 0. . . (*num*-1)/2, with shifted gain and index profiles. (c) Emitted intensity distribution for an array made of *num* = 21 lasers as a function of the coupling strength, m_m,. Intensity of laser j relative to the laser at edge (j=10) in logarithmic scale. In the inset the equivalent emitted intensity distribution for the punctual laser model of Eq. (3).

Finally, in order to provide a deeper analytic insight, we consider a stationary and punctual model, i.e. assuming null spatial and temporal derivatives in Eq. (2) and just with inward axisymmetric coupling. The amplitude solution for the uncoupled lasers at each edge coincides with the standing alone laser: $|A|^2 = \frac{p_0-(1+\alpha)}{\alpha}$, from which, we induce the amplitudes of all lasers of the array, from the edges to the central laser, resulting in:

$$\sigma\left[(1-ih)\frac{p_0+|A_j|^2}{1+|A_j|^2}-(1+\alpha)\right]A_j + m_j^- A_{j+1} + m_j^+ A_{j-1} = 0\ ,\ for\ j = -\frac{num-1}{2}\ ,\ \ldots\ ,\ \frac{num-1}{2}$$

$$m_{-j}^-=m_j^+=0,\ \ m_j^-=m_{-j}^+=m_m \text{ for } j \geq 0. \tag{3}$$

This simple estimation of the central laser intensity and energy distribution on the array really shows a good agreement with the numerical integration of the forward and backward fields in Eq. (2) for the *num* asymmetrically coupled cavities. In spite of the simplicity of the punctual model, comparing Figs. 6(a) and 6(b) with 6(c), we observe an analogous trend, yet in Fig. 6(c) the pump is assumed to be just above the lasing threshold. Both results show a similar dependence on the number of lasers and coupling strength, and for the particular case of *num* = 21, both energy distribution patterns strongly change their profiles for the same critical value of m_m, about $m_m = 10^{-3}$.

We can simply deduce from Eq. (3) that for a weak coupling strength m_m, the gain enhancement in laser j given by the asymmetric coupling from the neighboring laser j+1 (or j-1) is small and the laser losses α limits the field amplitude A_j remaining constant along the array, from the edge

Optics EXPRESS

lasers to the central laser, with an intensity value about the standing alone laser $|A_j|^2 \approx \frac{p_0-(1+\alpha)}{\alpha}$. In contrast, for large m_m values, the asymmetric coupling strongly enhances gain, and the cascade effect from edges to the central laser is the cause of the energy localization with a sharp profile. Considering amplitude values much larger than the pump value, the multiplying factor becomes $\frac{A_{\pm|j|}}{A_{\pm|j+1|}} = \frac{m_m}{\sigma\alpha}$ from which we can infer the threshold coupling strength for a sharp profile in the energy distribution, $m_{mth} = \sigma\alpha = 10^{-3}$ for the considered parameters, in good agreement with numeric simulations.

6. Conclusions

In summary, we propose a physical mechanism for the temporal stabilization and localization of the emission of a coupled array of EELs or an EEL bar. The scheme is based on a non-Hermitian coupling between neighboring lasers with a global mirror-symmetric geometry. While the monomode emission of a single laser is assured by reducing its width, spatiotemporal instabilities may still arise from the coupling between lasers in an array. Such temporal instabilities are molded by a non-Hermitian coupling that may be simply introduced by a lateral shift between the pump and index profile, technically by a spatial shift between the individual laser stripe and corresponding electrode. Such asymmetric coupling, while temporally stabilizing the emission also redistributes and localizes energy close to the central symmetry axis.

The proposed stabilization scheme is analyzed by a complete spatiotemporal model, including transverse and longitudinal spatial degrees of freedom and the temporal evolution of the electric fields and carriers. We perform a comprehensive numerical analysis in terms of the design parameters, namely the distance between lasers and non-Hermitian shift observing regimes of simultaneous temporal stabilizations and light localization. In turn, the validity of the proposal is also demonstrated for an array with a large number of lasers using a simplified model where the transverse space is accounted by the coupling between neighboring laser cavities.

The proposed non-Hermitian architecture for stable EEL bars is demonstrated leading to a brighter output beam, yet the field concentration is expected to facilitate a direct coupling of these semiconductor lasers arrays to an optical fiber.

Funding. Ministerio de Economía y Competitividad (BES-2016-076422, FIS2015-65998-C2-1-P).

Disclosures. The authors declare that there are no conflicts of interest related to this article.

Data availability. Data underlying the results presented in this paper are not publicly available at this time but may be obtained from the authors upon reasonable request.

References

1. O. Hess, S. W. Koch, and J. V. Moloney, "Filamentation and beam propagation in broad-area semiconductor lasers," IEEE J. Quantum Electron. **31**(1), 35–43 (1995).
2. V. I. Bespalov and V. I. Talanov, "Filamentary structure of light beams in Nonlinear liquids," J. Exp. Theor. Phys. Lett. **3**, 307 (1966).
3. H. Adachihara, O. Hess, E. Abraham, and J. V. Moloney, "Spatiotemporal chaos in broad-area semiconductor lasers," J. Opt. Soc. Am. B **10**(3), 496 (1993).
4. H. G. Winful, "Instability threshold for an array of coupled semiconductor lasers," Phys. Rev. A **46**(9), 6093–6094 (1992).
5. T. Y. Fan, "Laser beam combining for high-power, high-radiance sources," IEEE J. Sel. Top. Quantum Electron. **11**(3), 567–577 (2005).
6. S. Yanchuk, A. Stefanski, T. Kapitaniak, and J. Wojewoda, "Dynamics of an array of mutually coupled semiconductor lasers," Phys. Rev. E **73**(1), 016209 (2006).
7. H. G. Winful and L. Rahman, "Synchronized chaos and spatiotemporal chaos in arrays of coupled lasers," Phys. Rev. Lett. **65**(13), 1575–1578 (1990).
8. S. Wolff and H. Fouckhardt, "Intracavity stabilization of broad area lasers by structured delayed optical feedback," Opt. Express **7**(6), 222–227 (2000).
9. D. H. DeTienne, G. R. Gray, G. P. Agrawal, and D. Lenstra, "Semiconductor laser dynamics for feedback from a finite-penetration-depth phase-conjugate mirror," IEEE J. Quantum Electron. **33**(5), 838–844 (1997).
10. A. V. Pakhomov, R. M. Arkhipov, and N. E. Molevich, "Stabilization of class-B broad-area laser emission by external optical injection," J. Opt. Soc. Am. B **34**(4), 756–763 (2017).

Optics EXPRESS

11. H. G. Winful and S. S. Wang, "Stability of phase locking in coupled semiconductor laser arrays," Appl. Phys. Lett. **53**(20), 1894–1896 (1988).
12. I. V. Koryukin and P. Mandel, "Two regimes of synchronization in unidirectionally coupled semiconductor lasers," Phys. Rev. E **65**(2), 026201 (2002).
13. L. Wang, J. Zhang, Z. Jia, Y. Zhao, C. Liu, Y. Liu, S. Zhai, Z. Ning, X. Xu, and F. Liu, "Phase-locked array of quantum cascade lasers with an integrated Talbot cavity," Opt. Express **24**(26), 30275 (2016).
14. A. Jechow, M. Lichtner, R. Menzel, M. Radziunas, D. Skoczowsky, and A. G. Vladimirov, "Stripe-array diode-laser in an off-axis external cavity: Theory and experiment," Opt. Express **17**(22), 19599–19604 (2009).
15. J. Yu, L. Guo, L. H. Wu, Z. Wang, S. Gao, and D. Wu, "Optimization of beam transformation system for laser-diode bars," Opt. Express **24**(17), 19728–19735 (2016).
16. D. Gailevicius, V. Koliadenko, V. Purlys, M. Peckus, V. Taranenko, and K. Staliunas, "Photonic crystal microchip laser," Sci. Rep. **6**(1), 34173 (2016).
17. S. Gawali, J. Medina, D. Gailevičius, V. Purlys, G. Garre-Werner, C. Cojocaru, J. Trull, M. Botey, R. Herrero, J. Montiel-Ponsoda, and K. Staliunas, "Spatial filtering in edge-emitting lasers by intracavity chirped photonic crystals," J. Opt. Soc. Am. B **37**(10), 2856–2864 (2020).
18. R. Herrero, M. Botey, M. Radziunas, and K. Staliunas, "Beam shaping in spatially modulated broad-area semiconductor amplifiers," Opt. Lett. **37**(24), 5253–5255 (2012).
19. S. Kumar, R. Herrero, M. Botey, and K. Staliunas, "Suppression of modulation instability in broad area semiconductor amplifiers," Opt. Lett. **39**(19), 5598–5601 (2014).
20. W. W. Ahmed, J. Medina, R. Herrero, M. Botey, and K. Staliunas, "Stabilization of Broad-area semiconductor laser sources by simultaneous index and pump modulations," Opt. Lett. **43**(11), 2511–2514 (2018).
21. C. M. Bender and S. Böttcher, "Real Spectra in Non-Hermitian Hamiltonians Having PT-Symmetry," Phys. Rev. Lett. **80**(24), 5243–5246 (1998).
22. R. El-Ganainy, K. G. Makris, D. N. Christodoulides, and Z. H. Musslimani, "Theory of coupled optical PT-symmetric structures," Opt. Lett. **32**(17), 2632–2634 (2007).
23. C. E. Rüter, K. G. Makris, R. El-Ganainy, D. N. Christodoulides, M. Segev, and D. Kip, "Observation of parity–time symmetry in optics," Nat. Phys. **6**(3), 192–195 (2010).
24. A. Guo, G. J. Salamo, D. Duchesne, R. Morandotti, M. Volatier-Ravat, V. Aimez, G. A. Siviloglou, and D. N. Christodoulides, "Observation of PT-symmetry breaking in complex optical potentials," Phys. Rev. Lett. **103**(9), 093902 (2009).
25. A. A. Zyablovsky, A. P. Vinogradov, A. A. Pukhov, A. V. Dorofeenko, and A. A. Lisyansky, "PT-symmetry in optics," Phys.-Usp. **57**(11), 1063–1082 (2014).
26. K. G. Makris, R. El-Ganainy, D. N. Christodoulides, and Z. H. Musslimani, "Beam dynamics in PT symmetric optical lattices," Phys. Rev. Lett. **100**(10), 103904 (2008).
27. R. El-Ganainy, K. G. Makris, M. Khajavikhan, Z. H. Musslimani, S. Rotter, and D. N. Christodoulides, "Non-Hermitian physics and PT-symmetry," Nat. Phys. **14**(1), 11–19 (2018).
28. Z. Lin, H. Ramezani, T. Eichelkraut, T. Kottos, H. Cao, and D. N. Christodoulides, "Unidirectional invisibility induced by PT-symmetric periodic structures," Phys. Rev. Lett. **106**(21), 213901 (2011).
29. Z. Hayran, H. Kurt, R. Herrero, M. Botey, and K. Staliunas, "All-dielectric self-cloaked structures," ACS Photonics **5**(5), 2068–2073 (2018).
30. W. W. Ahmed, R. Herrero, M. Botey, Y. Wu, and K. Staliunas, "Restricted Hilbert transform for non-Hermitian management of fields," Phys. Rev. Appl. **14**(4), 044010 (2020).
31. Z. J. Wong, Y. L. Xu, J. Kim, K. O'Brien, Y. Wang, L. Feng, and X. Zhang, "Lasing and anti-lasing in a single cavity," Nat. Photonics **10**(12), 796–801 (2016).
32. H. Hodaei, M. A. Miri, A. U. Hassan, W. Hayenga, M. Heinrich, D. N. Christodoulides, and M. Khajavikhan, "Parity-time-symmetric coupled microring lasers operating around an exceptional point," Opt. Lett. **40**(21), 4955 (2015).
33. W. W. Ahmed, R. Herrero, M. Botey, and K. Staliunas, "Locally parity-time-symmetric and globally parity-symmetric systems," Phys. Rev. A **94**(5), 053819 (2016).
34. J. Medina, R. Herrero, M. Botey, and K. Staliunas, "Stabilized narrow-beam emission from broad-area semiconductor lasers," Phys. Rev. A **101**(3), 033833 (2020).
35. S. Longhi and L. Feng, "Mitigation of dynamical instabilities in laser arrays via non-Hermitian coupling," APL Photonics **3**(6), 060802 (2018).
36. Z. Gao, S. T. M. Fryslie, B. J. Thompson, P. S. Carney, and K. D. Choquette, "Parity-time symmetry in coherently coupled vertical cavity laser arrays," Optica **4**(3), 323 (2017).
37. G. P. Agrawal, "Fast-Fourier-transform based beam-propagation model for stripe-geometry semiconductor lasers: Inclusion of axial effects," J. Appl. Phys. **56**(11), 3100–3109 (1984).
38. E. A. Ultanir, D. Michaelis, F. Lederer, and G. I. Stegeman, "Stable spatial solitons in semiconductor optical amplifiers," Opt. Lett. **28**(4), 251–253 (2003).
39. J. J. Lim, S. Sujecki, L. Lang, Z. Zhang, D. Paboeuf, G. Pauliat, G. Lucas-Leclin, K.-H. Hasler, B. Sumpf, H. Wenzel, G. Erbert, B. Thestrup, P. M. Petersen, N. Michel, M. Krakowski, and E. C. Larkins, "Design and Simulation of Next-Generation High-Power, High-Brightness Laser Diodes," IEEE J. Sel. Top. Quantum Electron. **15**(3), 993–1008 (2009).

Optics EXPRESS

40. A. Zeghuzi, H. Wünsche, H. Wenzel, M. Radziunas, J. Fuhrmann, A. Klehr, U. Bandelow, and A. Knigge, "Time-dependent simulation of thermal lensing in high-power broad-area semiconductor lasers," IEEE J. Select. Topics Quantum Electron. **25**(6), 1–10 (2019).

Chapter 6
Conclusions and future perspectives

6.1 Conclusions

In this thesis, we present four different approaches for a smart control of light in semiconductor laser sources, aiming to improve their fundamental characteristics, particularly the spatio-temporal stability and beam quality of the emitted beam, without compromising their compact design.

In Chapter 2, we demonstrate spatial filtering in edge-emitting lasers (EELs) both theoretically and experimentally, using an intracavity chirped PhC. Predictions are based on a complete (2+1)-dimensional space-temporal model, including transverse and longitudinal spatial degrees of freedom and temporal evolution of the electric field and carriers. We predict a brightness enhancement by a factor of 2.5, using an optimized chirped PhC placed on both the front and rear facets of the laser. The effect may be even higher than the filtering performance of a slit. Experiments were performed in an extended cavity configuration using an intracavity 2D chirped PhC at the near-field plane and comparing it to a variable width slit in the far-field plane, determining a reduction of the beam quality parameter M^2 by a factor of 1.8, bringing along a brightness increase by a factor of 1.3. The experimental results are in good agreement with the numerical simulations which predict a brightness increase of 1.7, considering the transmission of the actual PhC used in experiments.

Further improvement may be achieved by exploring different spatial-filtering schemes. In particular, we predict a significant brightness enhancement, using an optimized chirped PhC placed at both the front and rear facets of the laser. These findings demonstrate that intracavity PhC filtering may render edge-emitting lasers bright light sources while keeping their compactness. Worth noting that the good agreement between numerical predictions and experiments provides confirmation of the validity of the model.

In Chapter 3, we propose using a non-Hermitian potential, with simultaneous 2D modulations of the pump and the refractive index as an effective scheme to stabilize edge-emitting laser sources, lasers and amplifiers, both in space and time. The proposed configuration can eliminate the modulation instability (MI) in highly non-linear regimes with appropriate parameters. We perform numerical simulations on the full model considering field and carriers with realistic parameters. The results predict that the doubly-modulated configuration can completely suppress modulation instability in non-linear regimes and offer a flexible control on spatio-temporal dynamics of EELs. The parameter space is

explored to determine the MI-free regions, showing that the best stabilization occurs around the resonance of both modulations. Moreover, we perform an analysis of the stabilization performance of the device in terms of the linewidth enhancement factor and the pump parameter for the doubly modulated EEL with a simplified paraxial model. The proposal could be implemented with existing nanofabrication techniques, being moreover compact, contrary to other approaches to improve the emission from edge-emitting laser sources.

Chapter 4 provides a feasible and compact scheme to control and stabilize the spatio-temporal dynamics of EELs. The proposal is based on the ability of non-Hermitian potentials with given local symmetries to manage the flow of light, based on asymmetric mode coupling. We impose a pump modulation, with a central symmetry axis which induces in-phase gain and refractive index modulations due to the Henry factor. Both modulations are, in turn, spatially shifted by an appropriate index profile that divides the modified EEL into two mirror-symmetric half-spaces holding PT-symmetry with opposite mode coupling. Such local non-Hermitian potential induces an inward mode coupling, accumulating the light generated from the entire active layer at the central symmetry axis, ensuring spatial regularization and temporal stability. By an exhaustive exploration of the modulation parameters, we show a significant improvement of the intensity concentration, stability, and brightness of the emitted beam. This approach produces a twofold benefit: light localization into a narrow-beam emission and the control over the spatio-temporal dynamics, improving the laser performance.

Finally, in Chapter 5, we present a physical mechanism for the temporal stabilization and localization of the emission of a coupled array of EELs (EEL bars). The scheme is based on a non-Hermitian coupling between neighboring lasers with a global axisymmetric geometry. While the monomode emission of a single laser is assured by reducing its width, spatio-temporal instabilities may still arise from the coupling between lasers in an array. Such temporal instabilities are molded by a non-Hermitian coupling that may be simply introduced by a lateral shift between the pump and index profile, namely a spatial shift between the individual laser stripe and the corresponding electrode. Such asymmetric coupling, while temporally stabilizing the emission, also redistributes and localizes energy close to the central symmetry axis.

The proposed stabilization scheme is first analyzed by the complete spatio-temporal model presented in Chapter 2. We perform a comprehensive numerical

analysis in terms of the design parameters, namely the distance between lasers and non-Hermitian shift observing regimes of simultaneous temporal stabilizations and light localization. In turn, the validity of the proposal is also demonstrated for an array with a large number of lasers using a simplified model where the transverse space is accounted by the coupling between neighboring laser cavities.

The proposed non-Hermitian architecture for stable EEL bars is demonstrated, leading to a brighter output beam, yet the field concentration is expected to facilitate a direct coupling of semiconductor laser sources to an optical fiber.

Therefore, the main results of this thesis show that: (I) intracavity filtering by an optimized chirped PhC may increase the brightness of an EEL over a factor of 2, when the PhC is placed on both the front and rear facets of the laser; (II) non-Hermitian intrinsic periodic potentials, with in-phase index and gain/loss modulations, may suppress modulation instability in EELs and semiconductor amplifiers; (III) a mirror-symmetric non-Hermitian potential applied within an EEL can lead to a simultaneous spatio-temporal stabilization while the field is enhanced and concentrated; and (IV) an analogous geometric scheme may be applied to an EEL bar, by spatially shifting the gain profile to induce asymmetric coupling between neighboring lasers, leading to stabilization and spatial redistribution of the emitted light, favoring direct coupling to optical fibers.

6.2 Future Perspectives

The first scheme presented in this thesis demonstrates intracavity filtering in a single EEL using a Photonic Crystal. After the theoretical and experimental demonstration of the proof of principle of the proposal and the brightness enhancement in a single EEL, the DONLL group started collaborating with Monocrom Company, aiming to implement intracavity PhC filtering into EEL bars. Therefore, the implementation of the proposal is actually a real ongoing project.

The other three proposals of the thesis are devoted to the theoretical and numerical study of the ability of non-Hermitian potentials to tailor the spatio-temporal dynamics of EELs, both to stabilize and improve the beam quality by controlling the light flow. These schemes aim to provide a basis for developing new techniques and methods in the novel platform of non-Hermitian Photonics.

Indeed, this topic is demonstrated on real physical systems, specifically on edge-emitting amplifiers, lasers and lasers bars. Therefore, the next natural step is to experimentally apply the proposal in actual devices. Regarding the advances in nanotechnology fabrication techniques, we expect to soon see an experimental confirmation, in collaboration with experimental groups.

Besides, the demonstrated ability of non-Hermitian potentials to control the field flows is an exciting step forward that may be explored beyond the field of optics, i.e., in other physical systems that present energy dissipation. Thus, this may be explored in fields ranging from plasmonics, acoustics, or even the control of turbulence. In particular, the DONLL group is exploring the control of turbulent states in the general model of the Complex Ginzburg-Landau Equation (CGLE) framework.

In conclusion, we expect that the present thesis results may contribute or directly lead to future new prospects in controlling light flows by non-Hermitian systems, with different technological applications.

References

[Ada93] H. Adachihara, O. Hess, E. Abraham, P. Ru, and J. V. Moloney, *"Spatiotemporal chaos in broad-area semiconductor lasers,"* Journal of Optical Society of America B 10, 658-665 (1993).

[Ahm15] W. W. Ahmed, S. Kumar, R. Herrero, M. Botey, M. Radziunas, and K. Staliunas, *"Stabilization of flat-mirror vertical-external-cavity surface-emitting lasers by spatiotemporal modulation of the pump profile,"* Physical Review A 92(4), 043829 (2015).

[Ahm16] W. W. Ahmed, R. Herrero, M. Botey, and K. Staliunas, *"Locally parity-time-symmetric and globally parity-symmetrics systems,"* Physical Review A 94(5), 053819 (2016).

[Ahm18] W. W. Ahmed, S. Kumar, J. Medina, M. Botey, R. Herrero, and K. Staliunas, *"Stabilization of broad-area semiconductor laser sources by simultaneous index and pump modulations,"* Optics Letters 43(11), 2511-2514 (2018).

[Ahm18-2] W. W. Ahmed, S. Kumar, J. Medina, M. Botey, R. Herrero, and K. Staliunas, *"Stabilization of Broad Area Semiconductor Amplifiers and Lasers by Double Modulation of Pump and Refractive Index,"* 2018 20th International Conference on Transparent Optical Networks (ICTON), IEEE, 2018.

[Ahm18-3] W. W. Ahmed, R. Herrero, M. Botey, Z. Hayran, H. Kurt, K. Staliunas, K, *"Directionality fields generated by a local Hilbert transform,"* Physical Review A 97(3), 033824 (2018).

[Agr84] G. P. Agrawal, *"Fast Fourier transform based beam propagation model for stripe geometry semiconductor lasers: Inclusion of axial effects."* Journal of Applied Physics 56, 3100 (1984).

[Agr13] G. P. Agrawal, and N. K. Dutta, "Semiconductor lasers," Springer Science & Business Media (2013).

[Alf01] Z. I. Alferov, "*Nobel Lecture: The double heterostructure concept and its applications in physics, electronics, and technology*," Reviews of modern physics 73(3), 767 (2001).

[Bar13] A. Baranov, and E. Tournié, "Semiconductor lasers: Fundamentals and applications," Elsevier (2013).

[Ben67] T. B. Benjamin, and J. E. Feir, *"The disintegration of wave trains on deep water Part 1. Theory,"* Journal of Fluid Mechanics 27(3), 417-430 (1967).

[Ben98] C. M. Bender, and S. Boettcher, *"Real spectra in non-Hermitian Hamiltonians having P-T symmetry,"* Physical Review Letters 80(24), 5243 (1998).

[Bes66] V. I. Bespalov and V. I. Talanov, *"Filamentary Structure of Light Beams in Nonlinear Liquids,"* Journal of Experimental and Theoretical Physics Letters 3, 307-309 (1966).

[Böh08] K. Böhringer, and O. Hess, *"A full time-domain approach to spatio-temporal dynamics of semiconductor lasers. I. Theoretical formulation"*, Progress in Quantum Electronics 32(5-6), 159-246 (2008).

[Bot09] M. Botey "Ligh propagation and generation in photonic nanostructures," PhD Thesis. http://www.tdx.cat/TDX-0601110-141417 (2009).

[Bot10] M. Botey, R. Herrero, and K.Staliunas, *"Light in materials with periodic gain-loss modulation on a wavelength scale,"* Physical Review A 82(1) 013828 (2010).

[Bot19] M. Botey, W. W. Ahmed, J. Medina, R. Herrero, and K. Staliunas, *"Non-Hermitian Broad Aperture Semiconductor Lasers Based on PT-Symmetry,"* 21st International Conference on Transparent Optical Networks (ICTON 2019), IEEE.

[Bot19-2] M. Botey, W. W. Ahmed, J. Medina, R. Herrero, Y. Wu, Y., and K. Staliunas, *"Regularization of broad-area lasers by non-Hermitian potentials,"* Proceedings of the 10th International Conference on Metamaterials, Photonic Crystals and Plasmonics (META 2019).

[Bur99] T. Burkhard, M. O. Ziegler, I. Fischer, and W. Elsäßer, *"Spatio-temporal dynamics of broad-area semiconductor lasers and its characterization,"* Chaos Solitons & Fractals 10, 845–850 (1999).

[Bus98] K. Busch, and S. John, *"Photonic bandgap formation in certain self-organizing systems,"* Physical Review E 58(3), 3896 (1998).

[Cha14] L. Chang, X. Jiang, S. Hua, C. Yang, J. Wen, L. Jiang, G. Li, G. Wang, and M. Xiao, *"Parity time symmetry and variable optical isolation in active passive-coupled microresonators*," Nature Photonics 8, 524 (2014).

[Col10] E. Colak, A. O. Cakmak, A. E. Serebryannikov, and E. Ozbay. *"Spatial filtering using dielectric photonic crystals at beam-type excitation,"* Journal of Applied Physics 108, 113106 (2010).

[DeT97] D. H. DeTienne, G. R. Gray, G. P. Agrawal, and D. Lenstra, *"Semiconductor laser dynamics for feedback from a finite-penetration-depth phase-conjugated mirror,"* IEEE Journal of Quantum Electronics 33, 838 (1997).

[Die00] R. Diehl, "High-power diode laser, fundamentals, technology, applications," Springer-Verlag (2000).

[El-G18] R. El-Ganainy, K. G Makris, M. Khajavikhan, Z. H. Musslimani, S. Rotter, and D. N. Christodoulides, *"Non-Hermitian physics and PT-symmetry,"* Nature Physics 14(1), 11-19 (2018).

[Fen12] L. Feng, Y.-L. Xu, W. S. Fegadolli, M.-H. Lu, J. E. Oliveira, V. R. Almeida, Y.-F. Chen, and A. Scherer, "*Experimental demonstration of a unidirectional reflectionless parity-time metamaterial at optical frequencies*," Nature Materials 12, 108 (2012).

[Fen17] L. Feng, R. El-Ganainy, G. Li, "Non-Hermitian photonics based on parity–time symmetry." Nature Photonics 11.12 (2017): 752-762.

[Gai16] D. Gailevičius, V. Koliadenko, V. Purlys, M. Peckus, V. Taranenko, and K. Staliunas, *"Photonic crystal microchip laser,"* Scientific Reports 6(1), 1-5 (2016).

[Gai19] D. Gailevičius, V. Purlys, and K. Staliunas, *"Photonic crystal spatial filters fabricated by femtoseconds pulsed Bessel beam,"* Optics Letters 44, 20 (2019).

[Gaw19] S. Gawali, D. Gailevičius, G. Garre-Werner, V. Purlys, C. Cojocaru, J. Trull, J. Montiel-Ponsoda, and K. Staliunas, *"Photonic Crystal Spatial Filtering in Broad Aperture Diode laser,"* Applied Physics Letters 115, 141104 (2019).

[Gaw20] S. Gawali, J. Medina, D. Gailevičius, V. Purlys, G. Garre-Werner, C. Cojocaru, J. Trull, M. Botey, R. Herrero, J. Montiel-Ponsoda, and K. Staliunas, *"Spatial filtering in edge-emitting lasers by intracavity chirped photonic crystals,"* Journal of the Optical Society of America B 37(10), 2856-2864 (2020).

[Gol88] L. Goldberg and M.K. Chun, *"Injection locking characteristics of a 1 W broad stripe laser diode,"* Applied Physics Letters 53, 1900-1902 (1988).

[Guo09] A. Guo, G. J. Salamo, D. Duchesne, R. Morandotti, M. Volatier-Ravat, V. Aimez, and D. N. Christodoulides, *"Observation of PT-symmetry breaking in complex optical potentials,"* Physical Review Letters 103, 093902 (2009).

[Hay18] Z. Hayran, R. Herrero, M. Botey, H. Kurt, K. Staliunas, "Invisibility on demand based on a generalized Hilbert transform," Physical Review A, 98(1), 013822 (2018).

[Hay18-2] Z. Hayran, H. Kurt, R. Herrero, M. Botey, K. Staliunas, *"All-dielectric self-cloaked structures,"* ACS photonics, 5(5), 2068-2073, (2018).

[Hal62] R. N. Hall, G. E. Fenner, J. D. Kingsley, T. J. Soltys, and R. O. Carlson, *"Coherent light emission from GaAs junction,"* Physical Review Letters 9, 9 (1962).

[Hen82] C. Henry, *"Theory of the linewidth of semiconductor lasers,"* IEEE Journal of Quantum Electronics 18(2), 259-264 (1982).

[Her12] R. Herrero, M. Botey, M. Radziunas, and K. Staliunas, *"Beam shaping in spatially modulated broad area semiconductor amplifiers,"* Optics Letters 37, 5253-5255 (2012).

[Hes95] O. Hess, S. W. Koch, and J. V. Moloney, *"Filamentation and beam propagation in broad-area semiconductor lasers,"* IEEE Journal of Quantum Electronics 31, 35 (1995).

[Hod14] H. Hodaei, M. A. Miri, M. Heinrich, D. N. Christodoulides, D. and M. Khajavikhan, *"Parity-time-symmetric microring lasers,"* Science 346(6212), 975-978 (2014).

[Hod17] H. Hodaei, A. U. Hassan, S. Wittek, H. Garcia-Gracia, R. El-Ganainy, D. N. Christodoulides and M. Khajavikha*"Enhanced sensitivity at higher-order exceptional points,"* Nature 548, 187–191 (2017).

[Hok19] M. P. Hokmabadi, N. S. Nye, R. El-Ganainy, D. N. Christodoulides, and M. Khajavikhan, *"Supersymmetric laser arrays,"* Science 363(6427), 623-626 (2019).

[Iid98] K. Iida, H. Horiuchi, O. Matoba, T. Omatsu, T. Shimura, and K. Kuroda, *"Injection locking of a broad-area diode laser through a double phase-conjugate mirror,"* Optical Communications 146, 6–10 (1998).

[Jec06] A. Jechow, V. Raab, and R. Menzel, "*High CW power using an external cavity for spectral beam combining of diode laser-bar emission,"* Applied Optics, 45(15), 3545 -3547 (2006).

[Jia15] Y. Jia, Y. Yan, S. V. Kesava, E. D. Gomez. and N. C. Giebink, *"Passive parity-time symmetry in organic thin-film waveguides,"*

American Chemical Society Photonics 2(2), 319-325 (2015).

[Joa11] J. D. Joannopoulos et al. "Photonic crystals: molding the flow of light," Princeton university press (2011).

[Joh87] S. John, *"Strong localization of photons in certain disordered dielectric superlattices,"* Physical Review Letters 58(23), 2486 (1987).

[Kot10] T. Kottos, *"Optical physics: Broken symmetry makes light work,"* Nature Physics 6, 166 (2010).

[Kum12] N. Kumar, M. Botey, R. Herrero, and K. Staliunas *"High-directional wave propagation in periodic loss modulated materials,"* Photonics and Nanostructures-Fundamentals and Applications 10(4), 644-650 (2012).

[Kum13] N. Kumar, R. Herrero, M. Botey, and K. Staliunas, *"Flat lensing by periodic loss-modulated materials,"* Journal of the Optical Society of America B 30(10), 2684-2688 (2013).

[Kum14] S. Kumar, R. Herrero, M. Botey, and K. Staliunas, *"Suppression of modulation instability in broad area semiconductor amplifiers,"* Optics Letters 39(19), 5598-5601 (2014).

[Kum15] S. Kumar, R. Herrero, M. Botey, and K. Staliunas, *"Taming of modulation instability by spatio-temporal modulation of the potential,"* Scientific Reports 5(1), 1-7 (2015).

[Kum16] S. Kumar, W. W. Ahmed, R. Herrero, M. Botey, M. Radziunas, and K. Staliunas, "Stabilization of Broad Area Semiconductor Amplifiers by Spatially Modulated Potentials," Nonlinear Dynamics: Materials, Theory, and Experiments, Springer International Publishing (2016).

[Li00] L. Li, *"The advances and characteristics of high-power diode laser materials processing,"* Optics and Lasers in Engineering 34, 231-253 (2000).

[Li07] H. Li, I. Chyr, X. Jin, F. Reinhardt, T. Towe, D. Brown, T. Nguyen, M. Berube, T. Truchan, D. Hu, R. Miller, R. Srinivasan, T. Crum, E. Wolak, R. Bullock, J. Mott, and J. Harrison, *">700W continuous-wave output power from single laser diode bar,"* Electronical Letters 43(1), 27–28 (2007).

[Lin11] Z. Lin, H. Ramezani, T. Eichelkraut, T. Kottos, H. Cao, and D. N. Christodoulides, *"Unidirectional invisibility induced by PT-symmetric periodic structures*," Physical Review Letters 106(21), 213901 (2011).

[Liu14] H. Liu, X. Liu, L. Xiong, and W. Zhao, "Packaging of High Power Semiconductor Lasers," Springer (2014).

[Lon11] S. Longhi, *"Invisibility in-symmetric complex crystals,"* Journal of Physics A: Mathematical and Theoretical 44.48, 485302 (2011).

[Loc70] H. F. Lockwood, H. Kressel, H. S. Sommers Jr, and F. Z. Hawrylo, *"An efficient large optical cavity injection laser,"* Applied Physics Letters 17(11) 499-502 (1970).

[Lug99] L. A. Lugiato, L. Spinelli, G. Tissoni, and M. Brambilla, *"Modulational instabilities and cavity solitons in semiconductor microcavities,"* Journal of Optics B: Quantum and Semiclassical Optics 1(1), 43 (1999).

[Mai10] L. Maigyte, T. Gertus, M. Peckus, J. Trull, C. Cojocaru, V. Sirutkaitis, and K. Staliunas, *"Signatures of light-beam spatial filtering in a three-dimensional photonic crystal,"* Physical Review A 82(4), 043819 (2010).

[Mai15] L. Maigyte and K. Staliunas, *"Spatial filtering with photonic crystals,"* Applied Physics Reviews 2, 011102 (2015).

[Med18] J. Medina, W. W. Ahmed, S. Kumar, M. Botey, R. Herrero, and K. Staliunas, *"Stabilization of Broad Area Semiconductor Laser Sources,"* 20th International Conference on Transparent Optical Networks (ICTON 2018), IEEE.

[Med19] J. Medina, M. Botey, R. Herrero, and K. Staliunas, *"Spatiotemporal stabilization of PT-symmetric BAS lasers,"* The European Conference on Lasers and Electro-Optics. Optical Society of America (European CLEO 2019).

[Med20] J. Medina, M. Botey, R. Herrero, and K. Staliunas, *"Stabilized narrow-beam emission from broad-area semiconductor lasers,"* Physical Review A 101(3), 033833 (2020).

[Med20-2] J. Medina, M. Botey, R. Herrero, and K. Staliunas, *"Spatiotemporal stabilization of PT-symmetric BAS lasers,"* Proceedings of SPIE 11356 (2020).

[Med20-3] J. Medina, R. Herrero, M. Botey, and K. Staliunas, *"Stabilized Bright Narrow Beams from Edge-Emitting Lasers,"* 22nd International Conference on Transparent Optical Networks (ICTON 2020), IEEE.

[Med21] J. Medina, R.Herrero, M. Botey, and K. Staliunas, *"Non-Hermitian arrangement for a stable semiconductor laser,"* Optics Express 29(15), 23997-24009 (2021).

[Oht12] J. Ohtsubo, "Semiconductor lasers: stability, instability, and chaos" Springer (2012).

[Osi87] M. Osinski, and J. Buus, *"Linewidth broadening factor in semiconductor lasers--An overview,"* IEEE Journal of Quantum Electronics 23(1), 9-29 (1987).

[Oue87] F. Ouellette, "*Dispersion cancellation using linearly chirped bragg grating filters in optical waveguides,"* Optics Letters 12, 847 (1987).

[Pak17] A. V. Pakhomov, R. M. Arkhipov, N. E., and Molevich, "*Stabilization of class-B broad-area laser emission by external optical injection,"* Journal of the Optical Society of America B 34, 756 (2017).

[Raa02] V. Raab, and R. Menzel, *"External resonator design for high-power laser diodes that yields 400mW of TEM00 power*," Optics Letters 27, 167-169 (2002).

[Rad11] M. Radziunas, *"Numerical bifurcation analysis of the traveling wave model of multisection semiconductor lasers*," Physica D: Nonlinear Phenomena 213(1), 98-112 (2001).

[Rad11-2] M. Radziunas and K. Staliunas, *"Spatial "rocking" in broad-area semiconductor lasers,"* Europhysics Letters 95, 14002 (2011).

[Rad13] M. Radziunas, M. Botey, R. Herrero, and K. Staliunas, *"Intrinsic beam shaping mechanism in spatially modulated broad area semiconductor amplifiers,"* Applied Physics Letters 103, 132101-132104 (2013).

[Reg12] A. Regensburger, C. Bersch, M. A. Miri, G. Onishchukov, D. N. Christodoulides, and U. Peschel, *"Parity-time synthetic photonic lattices,"* Nature 488, 167 (2012).

[Rüt10] C. E. Rüter, K. G. Makris, K, R. El-Ganainy, D. N. Christodoulides, M. Segev, and D. Kip, *"Observation of parity-time symmetry in optics,"* Nature Physics 6, 192-195 (2010).

[Sal85] J. Salzman, T. Venkatesan, R. Lang, M. Mittelstein, and A.Yariv, *"Unstable resonator cavity semiconductor lasers,"* Applied Physics Letters 46, 218–220 (1985).

[Ser09] A. E. Serebryannikov, A. Y. Petrov, and Ekmel Ozbay, *" Toward photonic crystal based spatial filters with wide angle ranges of total transmission,"* Applied Physics Letters 94, 181101 (2009).

[Sie86] L. Siegman, "Lasers," University Science Books (1986).

[Sil96] W. T. Silfvast, "Laser Fundamentals" Cambridge University Press (1996).

[Sou12] C. M. Soukoulis, "Photonic crystals and light localization in the 21st century," Springer Science & Business Media (2012).

[Spi98] L. Spinelli, G. Tissoni, M. Brambilla, F. Prati, and L. A. Lugiato, *"Spatial solitons in semiconductor microcavities,"* Physical Review A 58, 2542, 1998.

[Sta06] K. Staliunas and R. Herrero, *"Nondiffractive propagation of light in photonic crystals,"* Physical Review E 73, 016601 (2006).

[Sta09] K. Staliunas, R. Herrero, and R. Vilaseca, *"Subdiffraction and spatial filtering due to periodic spatial modulation of the gain-loss profile,"* Physical Review A 80, 013821 (2009).

[Ste07] N. Stelmakh, *"Harnessing Multimode Broad-Area Laser-Diode Emission Into a Single-Lobe Diffraction-Limited Spot,"* IEEE Photonics Technology Letters 19, 1392-1394 (2007).

[Sum09] B. Sumpf, K.-H Hasler, P. Adamiec, F. Bugge, F. Dittmar, J. Fricke, H. Wenzel, M. Zorn, G. Erbert, and G. Tränkle, *"High-Brightness Quantum Well Tapered Lasers,"* IEEE Journal of selected topics in Quantum Electronics 15, 3 (2009).

[Tan06] Z. Tang, H. Zhang, Y. Ye, C. Zhao, S. Wen, and D. Fan, "*Low-pass spatial filtering using optically thinner left-handed photonic crystals,"* 2006 International Symposium on Biophotonics, Nanophotonics and Metamaterials, IEEE.

[Tan07] Z. Tang, D. Fan, S. Wen, Y. Ye, and C. Zhao, *"Low-pass spatial filtering using a two-dimensional self-collimating photonic Crystal,"* Chinese Optics Letters 5, S211 (2007).

[Tei91] M. C. Teich, B. E. A. Saleh, "Fundamentals of Photonics," Wiley (1991).

[Tur10] S. K. Turitsyn, S. A. Babin, A. E. El-Taher, P. Harper, D. V. Churkin, S. I. Kablukov, J. D. Ania-Castañón, V. Karalekas, and E. V. Podivilov, *"Random distributed feedback fiber laser,"* Nature Photonics 4(4), 231-235 (2010).

[Tur10] M. Turduev, M. Botey, I. Giden, R. Herrero, H. Kurt, E. Ozbay, and K. Staliunas, *"Two-dimensional complex parity-time-symmetric photonic structures,"* Physical Review A 91(2), 023825.

[Ult06] E. A. Ultanir, D. N. Christodoulides, and G. I. Stegeman, *"Spatial modulation instability in periodically patterned semiconductor optical amplifiers,"* Journal of the Optical Society of America B 23, 341-346 (2006).

[Yab87] E. Yablonovitch, *"Inhibited spontaneous emission in solid-state physics and electronics,"* Physical Review Letters 58(20), 2059 (1987).

[Yu96] P. Y. Yu and M. Cardona, "Fundamentals of Semiconductors,"

Springer-Verlag (1996).

[Yu16] J. Yu, L. Guo, H. Wu, Z. Wang, S. Gao, and D. Wu, *"Optimization of a beam transformation system for laser-diode bars,"* Optics Express 24(17), 19728-19735 (2016).

[Val06] G. J. D Valcárcel, E. Roldán, and F. Prati, "*Semiclassical theory of amplification and lasing,"* Revista mexicana de física E, *52*(2), 198-214 (2006).

[Vla06] A. G. Vladimirov, D. V. Skryabin, G. Kozyreff, P. Mandel, and M. Tlidi, *"Bragg localized structures in a passive cavity with transverse modulation of the refractive index and the pump,"* Optics Express 14(1), 1-6 (2006).

[Wol99] S. Wolff, D. Messerschmidt, and H. Fouckhardt, "*Fourier-optical selection of transverse modes in broad area lasers*," Optics Express 5(3), 32 (1999).

[Wol00] S. Wolff, and H. Fouckhardt, "*Intracavity stabilization of broad area lasers by structured delayed optical feedback,*" Optics Express 7(6), 222-227 (2000).

[Zia14] A. A. Zyablovsky, A. P. Vinogradov, A. A. Pukhov, A. V. Dorofeenko, and A. A. Lisyansk, "*PT-symmetry in optics,"* Physics-Uspekhi 57(11), 1063 (2014).